

The Effect of Coastal Environment on the Degradation of Reinforced Concrete Structures

Lead Guest Editor: Charis Apostolopoulos

Guest Editors: Stefania Imperatore, Zila Rinaldi, and Walter Salvatore





The Effect of Coastal Environment on the Degradation of Reinforced Concrete Structures

Advances in Civil Engineering

The Effect of Coastal Environment on the Degradation of Reinforced Concrete Structures

Lead Guest Editor: Charis Apostolopoulos

Guest Editors: Stefania Imperatore, Zila Rinaldi,
and Walter Salvatore



Copyright © 2020 Hindawi Limited. All rights reserved.

This is a special issue published in "Advances in Civil Engineering." All articles are open access articles distributed under the Creative Commons Attribution License, which permits unrestricted use, distribution, and reproduction in any medium, provided the original work is properly cited.






Chief Editor

Cumaraswamy Vipulanandan, USA










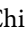



Associate Editors

Chiara Bedon , Italy
Constantin Chalioris , Greece
Ghassan Chehab , Lebanon
Ottavia Corbi, Italy
Mohamed ElGawady , USA
Husnain Haider , Saudi Arabia
Jian Ji , China
Jiang Jin , China
Shazim A. Memon , Kazakhstan
Hossein Moayedi , Vietnam
Sanjay Nimbalkar, Australia
Giuseppe Oliveto , Italy
Alessandro Palmeri , United Kingdom
Arnaud Perrot , France
Hugo Rodrigues , Portugal
Victor Yepes , Spain
Xianbo Zhao , Australia

Academic Editors

José A.F.O. Correia, Portugal
Glenda Abate, Italy
Khalid Abdel-Rahman , Germany
Ali Mardani Aghabaglou, Turkey
José Aguiar , Portugal
Afaq Ahmad , Pakistan
Muhammad Riaz Ahmad , Hong Kong
Hashim M.N. Al-Madani , Bahrain
Luigi Aldieri , Italy
Angelo Aloisio , Italy
Maria Cruz Alonso, Spain
Filipe Amarante dos Santos , Portugal
Serji N. Amirkhania, USA
Eleftherios K. Anastasiou , Greece
Panagiotis Ch. Anastasopoulos , USA
Mohamed Moafak Arbili , Iraq
Farhad Aslani , Australia
Siva Avudaiappan , Chile
Ozgur BASKAN , Turkey
Adewumi Babafemi, Nigeria
Morteza Bagherpour, Turkey
Qingsheng Bai , Germany
Nicola Baldo , Italy
Daniele Baraldi , Italy

Eva Barreira , Portugal
Emilio Bastidas-Arteaga , France
Rita Bento, Portugal
Rafael Bergillos , Spain
Han-bing Bian , China
Xia Bian , China
Huseyin Bilgin , Albania
Giovanni Biondi , Italy
Hugo C. Biscaia , Portugal
Rahul Biswas , India
Edén Bojórquez , Mexico
Giosuè Boscato , Italy
Melina Bosco , Italy
Jorge Branco , Portugal
Bruno Briseghella , China
Brian M. Broderick, Ireland
Emanuele Brunesi , Italy
Quoc-Bao Bui , Vietnam
Tan-Trung Bui , France
Nicola Buratti, Italy
Gaochuang Cai, France
Gladis Camarini , Brazil
Alberto Campisano , Italy
Qi Cao, China
Qixin Cao, China
Iacopo Carnacina , Italy
Alessio Cascardi, Italy
Paolo Castaldo , Italy
Nicola Cavalagli , Italy
Liborio Cavaleri , Italy
Anush Chandrappa , United Kingdom
Wen-Shao Chang , United Kingdom
Muhammad Tariq Amin Chaudhary, Kuwait
Po-Han Chen , Taiwan
Qian Chen , China
Wei Tong Chen , Taiwan
Qixiu Cheng, Hong Kong
Zhanbo Cheng, United Kingdom
Nicholas Chileshe, Australia
Prinya Chindaprasirt , Thailand
Corrado Chisari , United Kingdom
Se Jin Choi , Republic of Korea
Heap-Yih Chong , Australia
S.H. Chu , USA
Ting-Xiang Chu , China

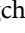
Zhaofei Chu , China
Wonseok Chung , Republic of Korea
Donato Ciampa , Italy
Gian Paolo Cimellaro, Italy
Francesco Colangelo, Italy
Romulus Costache , Romania
Liviu-Adrian Cotfas , Romania
Antonio Maria D'Altri, Italy
Bruno Dal Lago , Italy
Amos Darko , Hong Kong
Arka Jyoti Das , India
Dario De Domenico , Italy
Gianmarco De Felice , Italy
Stefano De Miranda , Italy
Maria T. De Risi , Italy
Tayfun Dede, Turkey
Sadik O. Degertekin , Turkey
Camelia Delcea , Romania
Cristoforo Demartino, China
Giuseppe Di Filippo , Italy
Luigi Di Sarno, Italy
Fabio Di Trapani , Italy
Aboelkasim Diab , Egypt
Thi My Dung Do, Vietnam
Giulio Dondi , Italy
Jiangfeng Dong , China
Chao Dou , China
Mario D'Aniello , Italy
Jingtao Du , China
Ahmed Elghazouli, United Kingdom
Francesco Fabbrocino , Italy
Flora Faleschini , Italy
Dingqiang Fan, Hong Kong
Xueping Fan, China
Qian Fang , China
Salar Farahmand-Tabar , Iran
Ilenia Farina, Italy
Roberto Fedele, Italy
Guang-Liang Feng , China
Luigi Fenu , Italy
Tiago Ferreira , Portugal
Marco Filippo Ferrotto, Italy
Antonio Formisano , Italy
Guoyang Fu, Australia
Stefano Galassi , Italy

Junfeng Gao , China
Meng Gao , China
Giovanni Garcea , Italy
Enrique García-Macías, Spain
Emilio García-Taengua , United Kingdom
DongDong Ge , USA
Khaled Ghaedi, Malaysia
Khaled Ghaedi , Malaysia
Gian Felice Giaccu, Italy
Agathoklis Giaralis , United Kingdom
Ravindran Gobinath, India
Rodrigo Gonçalves, Portugal
Peilin Gong , China
Belén González-Fonteboa , Spain
Salvatore Grasso , Italy
Fan Gu, USA
Erhan Güneyisi , Turkey
Esra Mete Güneyisi, Turkey
Pingye Guo , China
Ankit Gupta , India
Federico Gusella , Italy
Kemal Hacıfendioglu, Turkey
Jianyong Han , China
Song Han , China
Asad Hanif , Macau
Hadi Hasanzadehshooiili , Canada
Mostafa Fahmi Hassanein, Egypt
Amir Ahmad Hedayat , Iran
Khandaker Hossain , Canada
Zahid Hossain , USA
Chao Hou, China
Biao Hu, China
Jiang Hu , China
Xiaodong Hu, China
Lei Huang , China
Cun Hui , China
Bon-Gang Hwang, Singapore
Jijo James , India
Abbas Fadhil Jasim , Iraq
Ahad Javanmardi , China
Krishnan Prabhakan Jaya, India
Dong-Sheng Jeng , Australia
Han-Yong Jeon, Republic of Korea
Pengjiao Jia, China
Shaohua Jiang , China

MOUSTAFA KASSEM , Malaysia
Mosbeh Kaloop , Egypt
Shankar Karuppannan , Ethiopia
John Kechagias , Greece
Mohammad Khajehzadeh , Iran
Afzal Husain Khan , Saudi Arabia
Mehran Khan , Hong Kong
Manoj Khandelwal, Australia
Jin Kook Kim , Republic of Korea
Woosuk Kim , Republic of Korea
Vaclav Koci , Czech Republic
Loke Kok Foong, Vietnam
Hailing Kong , China
Leonidas Alexandros Kouris , Greece
Kyriakos Kourousis , Ireland
Moacir Kripka , Brazil
Anupam Kumar, The Netherlands
Emma La Malfa Ribolla, Czech Republic
Ali Lakirouhani , Iran
Angus C. C. Lam, China
Thanh Quang Khai Lam , Vietnam
Luciano Lamberti, Italy
Andreas Lampropoulos , United Kingdom
Raffaele Landolfo, Italy
Massimo Latour , Italy
Bang Yeon Lee , Republic of Korea
Eul-Bum Lee , Republic of Korea
Zhen Lei , Canada
Leonardo Leonetti , Italy
Chun-Qing Li , Australia
Dongsheng Li , China
Gen Li, China
Jiale Li , China
Minghui Li, China
Qingchao Li , China
Shuang Yang Li , China
Sunwei Li , Hong Kong
Yajun Li , China
Shun Liang , China
Francesco Liguori , Italy
Jae-Han Lim , Republic of Korea
Jia-Rui Lin , China
Kun Lin , China
Shibin Lin, China

Tzu-Kang Lin , Taiwan
Yu-Cheng Lin , Taiwan
Hexu Liu, USA
Jian Lin Liu , China
Xiaoli Liu , China
Xuemei Liu , Australia
Zaobao Liu , China
Zhuang-Zhuang Liu, China
Diego Lopez-Garcia , Chile
Cristiano Loss , Canada
Lyan-Ywan Lu , Taiwan
Jin Luo , USA
Yanbin Luo , China
Jianjun Ma , China
Junwei Ma , China
Tian-Shou Ma, China
Zhongguo John Ma , USA
Maria Macchiaroli, Italy
Domenico Magisano, Italy
Reza Mahinroosta, Australia
Yann Malecot , France
Prabhat Kumar Mandal , India
John Mander, USA
Iman Mansouri, Iran
André Dias Martins, Portugal
Domagoj Matesan , Croatia
Jose Matos, Portugal
Vasant Matsagar , India
Claudio Mazzotti , Italy
Ahmed Mebarki , France
Gang Mei , China
Kasim Mermerdas, Turkey
Giovanni Minafò , Italy
Masoomah Mirrashid , Iran
Abbas Mohajerani , Australia
Fadzli Mohamed Nazri , Malaysia
Fabrizio Mollaioli , Italy
Rosario Montuori , Italy
H. Naderpour , Iran
Hassan Nasir , Pakistan
Hossein Nassiraei , Iran
Satheeskumar Navaratnam , Australia
Ignacio J. Navarro , Spain
Ashish Kumar Nayak , India
Behzad Nematollahi , Australia

Chayut Ngamkhanong , Thailand
Trung Ngo, Australia
Tengfei Nian, China
Mehdi Nikoo , Canada
Youjun Ning , China
Olugbenga Timo Oladinrin , United Kingdom
Oladimeji Benedict Olalusi, South Africa
Timothy O. Olawumi , Hong Kong
Alejandro Orfila , Spain
Maurizio Orlando , Italy
Siti Aminah Osman, Malaysia
Walid Oueslati , Tunisia
SUVASH PAUL , Bangladesh
John-Paris Pantouvakis , Greece
Fabrizio Paolacci , Italy
Giuseppina Pappalardo , Italy
Fulvio Parisi , Italy
Dimitrios G. Pavlou , Norway
Daniele Pellegrini , Italy
Gatheeshgar Perampalam , United Kingdom
Daniele Perrone , Italy
Giuseppe Piccardo , Italy
Vagelis Plevris , Qatar
Andrea Pranno , Italy
Adolfo Preciado , Mexico
Chongchong Qi , China
Yu Qian, USA
Ying Qin , China
Giuseppe Quaranta , Italy
Krishanu ROY , New Zealand
Vlastimir Radonjanin, Serbia
Carlo Rainieri , Italy
Rahul V. Ralegaonkar, India
Raizal Saifulnaz Muhammad Rashid, Malaysia
Alessandro Rasulo , Italy
Chonghong Ren , China
Qing-Xin Ren, China
Dimitris Rizos , USA
Geoffrey W. Rodgers , New Zealand
Pier Paolo Rossi, Italy
Nicola Ruggieri , Italy
JUNLONG SHANG, Singapore

Nikhil Saboo, India
Anna Saetta, Italy
Juan Sagaseta , United Kingdom
Timo Saksala, Finland
Mostafa Salari, Canada
Ginevra Salerno , Italy
Evangelos J. Sapountzakis , Greece
Vassilis Sarhosis , United Kingdom
Navaratnarajah Sathiparan , Sri Lanka
Fabrizio Scozzese , Italy
Halil Sezen , USA
Payam Shafigh , Malaysia
M. Shahria Alam, Canada
Yi Shan, China
Hussein Sharaf, Iraq
Mostafa Sharifzadeh, Australia
Sanjay Kumar Shukla, Australia
Amir Si Larbi , France
Okan Sirin , Qatar
Piotr Smarzewski , Poland
Francesca Sollecito , Italy
Rui Song , China
Tian-Yi Song, Australia
Flavio Stochino , Italy
Mayank Sukhija , USA
Piti Sukontasukkul , Thailand
Jianping Sun, Singapore
Xiao Sun , China
T. Tafsirojjan , Australia
Fujiao Tang , China
Patrick W.C. Tang , Australia
Zhi Cheng Tang , China
Weerachart Tangchirapat , Thailand
Xiixin Tao, China
Piergiorgio Tataranni , Italy
Elisabete Teixeira , Portugal
Jorge Iván Tobón , Colombia
Jing-Zhong Tong, China
Francesco Trentadue , Italy
Antonello Troncone, Italy
Majbah Uddin , USA
Tariq Umar , United Kingdom
Muahmmad Usman, United Kingdom
Muhammad Usman , Pakistan
Mucteba Uysal , Turkey

Ilaria Venanzi , Italy
Castorina S. Vieira , Portugal
Valeria Vignali , Italy
Claudia Vitone , Italy
Liwei WEN , China
Chunfeng Wan , China
Hua-Ping Wan, China
Roman Wan-Wendner , Austria
Chaohui Wang , China
Hao Wang , USA
Shiming Wang , China
Wayne Yu Wang , United Kingdom
Wen-Da Wang, China
Xing Wang , China
Xiuling Wang , China
Zhenjun Wang , China
Xin-Jiang Wei , China
Tao Wen , China
Weiping Wen , China
Lei Weng , China
Chao Wu , United Kingdom
Jiangyu Wu, China
Wangjie Wu , China
Wenbing Wu , China
Zhixing Xiao, China
Gang Xu, China
Jian Xu , China
Panpan , China
Rongchao Xu , China
HE YONGLIANG, China
Michael Yam, Hong Kong
Hailu Yang , China
Xu-Xu Yang , China
Hui Yao , China
Xinyu Ye , China
Zhoujing Ye, China
Gürol Yildirim , Turkey
Dawei Yin , China
Doo-Yeol Yoo , Republic of Korea
Zhanping You , USA
Afshar A. Yousefi , Iran
Xinbao Yu , USA
Dongdong Yuan , China
Geun Y. Yun , Republic of Korea

Hyun-Do Yun , Republic of Korea
Cemal YİĞİT , Turkey
Paolo Zampieri, Italy
Giulio Zani , Italy
Mariano Angelo Zanini , Italy
Zhixiong Zeng , Hong Kong
Mustafa Zeybek, Turkey
Henglong Zhang , China
Jiupeng Zhang, China
Tingting Zhang , China
Zengping Zhang, China
Zetian Zhang , China
Zhigang Zhang , China
Zhipeng Zhao , Japan
Jun Zhao , China
Annan Zhou , Australia
Jia-wen Zhou , China
Hai-Tao Zhu , China
Peng Zhu , China
QuanJie Zhu , China
Wenjun Zhu , China
Marco Zucca, Italy
Haoran Zuo, Australia
Junqing Zuo , China
Robert Černý , Czech Republic
Süleyman İpek , Turkey



Contents

A Study on the Strengthening Performance of Concrete Beam by Fiber-Reinforced Polyurea (FRPU) Reinforcement

Jun-Hyuk Song, Eun-Taik Lee, and Hee-Chang Eun 



Research Article (9 pages), Article ID 6967845, Volume 2020 (2020)

Experimental Study on the Structural Performance Degradation of Corrosion-Damaged Reinforced Concrete Beams

Ju-Seong Jung, Bang Yeon Lee , and Kang-Seok Lee 

Research Article (14 pages), Article ID 9562574, Volume 2019 (2019)

Experimental Study on Flexural Behavior of Prestressed Concrete Beams Reinforced by CFRP under Chloride Environment

Yunyan Liu  and Yingfang Fan 

Research Article (14 pages), Article ID 2424518, Volume 2019 (2019)

Effect of Sulphate and Chloride Ingress on Selected Cements Mortar Prisms Immersed in Seawater and Leather Industry Effluent

Jackson Muthengia Wachira , Reginah Wangui Ngari, Joseph Karanja Thiong'o, and Joseph Mwiti Marangu 

Research Article (16 pages), Article ID 8191689, Volume 2019 (2019)

Research Article

A Study on the Strengthening Performance of Concrete Beam by Fiber-Reinforced Polyurea (FRPU) Reinforcement

Jun-Hyuk Song,¹ Eun-Taik Lee,² and Hee-Chang Eun ¹

¹Department of Architectural Engineering, Kangwon National University, Chuncheon, Republic of Korea

²Department of Architectural Engineering, Chung-Ang University, Seoul, Republic of Korea

Correspondence should be addressed to Hee-Chang Eun; heechang@kangwon.ac.kr

Received 14 May 2019; Accepted 29 July 2019; Published 11 March 2020

Guest Editor: Charis Apostolopoulos

Copyright © 2020 Jun-Hyuk Song et al. This is an open access article distributed under the Creative Commons Attribution License, which permits unrestricted use, distribution, and reproduction in any medium, provided the original work is properly cited.

Polyurea coating helps improve the ductility and toughness of structural members. A fiber-reinforced polyurea (FRPU) composite provides high load-carrying capacity and is applied by simply spraying it onto the member surface. Unlike existing reinforcement approaches, the FRPU coating method can prevent the ductility of concrete beams from deteriorating and the concrete surface from debonding. In this study, 20 concrete beams were tested with respect to their load-carrying capacity and flexural ductility using polyurea or FRPU reinforcement. The test variables included the type of reinforcing fibers, coating thickness, and weight-to-content ratio of the fibers in the FRPU. Moreover, the load-carrying capacity and mechanical behavior of all specimens were compared according to the content of the steel fibers, milled glass fibers, or carbon nanotubes (CNTs). Specimens reinforced using polyurea or FRPU were confirmed to retain the load-carrying capacity and flexural ductility to a certain degree after concrete failure at the tension face of the midspan section. The concrete beams ultimately failed through the fracture of polyurea or FRPU without debonding. Experiments were conducted to illustrate the strengthening effect by FRPU and determine its superiority.

1. Introduction

Elastomers are a class of polymetric materials. An elastomer has viscoelasticity, with a low elastic modulus and high yield strain. Polyurea is an elastomeric polymer derived from the rapid reaction of an isocyanate component and polyamine and is considered a versatile material. It has been utilized as a flooring and waterproofing material to prevent shrinkage when drying. It has a high tensile strength, elongation, and the capability to absorb the energy generated through dynamic and impulsive blast loading. In addition, it represents a good adhesion to concrete and can increase the toughness and flexural strength of the concrete, decreasing the stiffness. Polyurea coatings combine high flexibility with hardness and high elasticity with a high surface hardness.

Owing to the increased loading requirements, change in use, and structural deterioration, the structural performance can be recovered using retrofitting techniques. Building structures need to be evaluated and effectively implemented,

with economical repair and strengthening capabilities. Polyurea achieves flexural and shear reinforcement for structural members rather than blast or impact mitigation [1] and can improve the seismic performance of structures, controlling the plastic hinge occurrence, increasing the deformation capacity and dissipated energy, strengthening or changing the structural system, and enhancing the lateral stiffness. Marawan et al. [2] observed an increase in the flexural and shear capacity of small- and large-scale beams strengthened using a sprayed polyurea system depending on the thickness of the polyurea applied. Parniani and Toutanji [1] investigated the behavior of concrete beams strengthened using a polyurea coating system. They found that the polyurea coating system increases the flexural capacity and ductility of reinforced concrete beams. Kamonchaivanich et al. [3] compared the flexural strength of a back-coated ceramic with polyurea of a lower and higher modulus.

Structural-strengthening techniques include a section enlargement, a reinforced jacketing of externally bonded

steel elements, fiber reinforced polymer (FRP) composites, and other factors. There have been numerous studies related with an enhancement of the load-carrying capacity and ductility of a concrete member using FRP, which has been utilized in repairing and strengthening aged and performance-deteriorated structures, including their end of service life, steel corrosion, and concrete spalling. FRPs of a high tensile strength and low weight fail through concrete cover separation and interfacial debonding. Numerous analytical models have been developed to describe the mechanical characteristics of concrete externally confined with FRP composites [4–10].

The FRP composites are made up of fibers with a high tensile strength embedded in an epoxy matrix. An explicit bonding to achieve sufficient adhesiveness between the FRP composites and concrete structures is required for transferring the stress among them. Gideon and Alagusundaramoorthy [11] studied the flexural behavior and failure mode of concrete beam prototypes with a high shear span ratio externally bonded using carbon fiber-reinforced polymer (CFRP) laminates. Li et al. [12] determined that the variation in shear capacity of a strengthened beam depends strongly on the strengthened area. Alferjani et al. [13] observed that an epoxy resin is favorable in strengthening and an end anchorage is needed to eliminate debonding failures. FRP-strengthened beams exhibit debonding failure modes at the end of the beams without an end anchorage and a rupture of the FRP in beams with an end anchorage [14–21]. Uomoto et al. [22] introduced FRP composites to combine the structural and durability characteristics of FRPs as reinforcement in concrete constructions. Mahiyar and Soni [23] observed that the utilization of an FRP grid is extremely effective in enhancing the flexural strength of concrete.

FRPU is a composite used to mix elastic polyurea with fibers for a more enhanced load-carrying capacity and greater mechanical properties. FRPU coating systems can yield a multihazard retrofit material suitable for aging structures. Such systems must be useful in repair and retrofit applications for strengthening the structural capacity, improving the seismic performance, and mitigating blast and impact damage.

A polyurea or FRPU spraying method can prevent the debonding of FRP or steel plates from concrete surfaces and retain sufficient ductility. The fiber addition provides improved stiffness and strength to a composite system, whereas polyurea provides ductility. Greene and Myers [24] investigated the flexural and shear reinforcement capabilities of the systems provided by externally applied discrete fiber-reinforced polyurea (DFRP) coating systems. A DFRP system is a composite system used to simultaneously spray polyurea and chopped glass fibers into a spray pattern. A measurable strengthening in terms of both flexural and shear capacity, along with substantial gains in ductility, was found. In addition, they mentioned that an increased fiber length significantly reduces the ductility. Carey and Myers [25] also considered the addition of discrete chopped fibers to the polyurea for additional strength and a more developed fiber characterization of the polyurea system.

The present study investigates the applicability of FRPU when containing fiber reinforcements such as milled glass fibers, steel fibers, and carbon nanotubes (CNTs). This can be expected to enhance the load-carrying capacity and improve the ductility. Concrete beam tests were conducted to compare the load-carrying capacity and mechanical behavior depending on the reinforcing materials, spray thickness, and fiber weight-to-content ratio. It was observed that the specimens reinforced using polyurea or FRPU retain the additional load-carrying capacity and flexural ductility after a concrete failure at the tension face of the midspan section. The concrete beams ultimately failed through a fracture of polyurea or FRPU without debonding. The experiment results illustrate the reinforcement effect from the FRPU and the superiority of its application.

2. Experiment

2.1. Polyurea and FRPU. FRPU is manufactured by mixing the polyurea of a prepolymer and hardener with fibers. The FRPU moves through the hose after a premixing of the prepolymer and fiber and is simply sprayed onto the surface of the structural member using a high-pressure spray gun with a hardener. The constituents of the polyurea used in this experiment are shown in Table 1.

Three types of fibers, namely, steel fibers, CNTs, and milled glass fibers, were considered during this experiment. Steel fibers are filaments of wire, deformed and cut to various lengths, for the reinforcement of concrete, mortar, and other composite materials. CNTs are utilized as a powder requiring high strength, durability, and lightweight properties as compared to conventional materials. Milled glass fibers are made by cutting E-glass fibers into short pieces. E-glass fibers have an excellent electrical insulation property, can be processed into various shapes, and are mainly applied in the reinforcement of plastics. This is effective in improving not only the strength but also the surface conditions and dimensional stability. This experiment utilizes milled glass fibers of 300 μm in length.

As the first step of FRPU spraying, a primer is painted onto the surface of the concrete member, as shown in Figure 1(a), after the laitance, foreign substances, and pollutants are removed to improve the bond performance. After curing for 24 h, the prepolymer and fibers are mixed and stirred, as shown in Figure 1(b), and the premixed prepolymer and fibers are sprayed along with a hardener onto the member surface through the hose of a high-pressure spray gun, as shown in Figure 1(c). After the FRPU coating, the coating is finished with a primer painting, as shown in Figure 1(d). The FRPU coating technology is completed simply and strongly bonded to the member.

2.2. Specimens. Twenty concrete beams without reinforcing bars are prepared for testing. The specimens are designed using a polyurea-reinforced control beam and FRPU-reinforced beams. The parameters of the experiment include the type and weight-to-content ratio of the fiber and the spraying thickness. The thickness effect of single (3 mm) and

TABLE 1: Constituents of polyurea.

	Chemicals	Content (%)
Prepolymer	α -(2-Aminomethylethyl)- ω -(2-aminomethylethoxy)poly[oxy(methyl-1,2-ethanediy)]	60~70
	Ar,ar-diethyl-ar-methylbenzenediamine	20~30
	Poly[oxy(methyl-1,2-ethanediy)], α , α' , α'' -1,2,3-propanetriyltris[ω -(2-aminomethyl-ethoxy)-	1~10
	Titanium dioxide	1~2.7
	1,4-Benzenedicarboxylic acid, bis(2-ethylhexyl) ester	1~10
	etc.	1~10
Hardener	Polyurethane resin	90~100
	4-Methyl-1,3-dioxolan-2-one	1~10

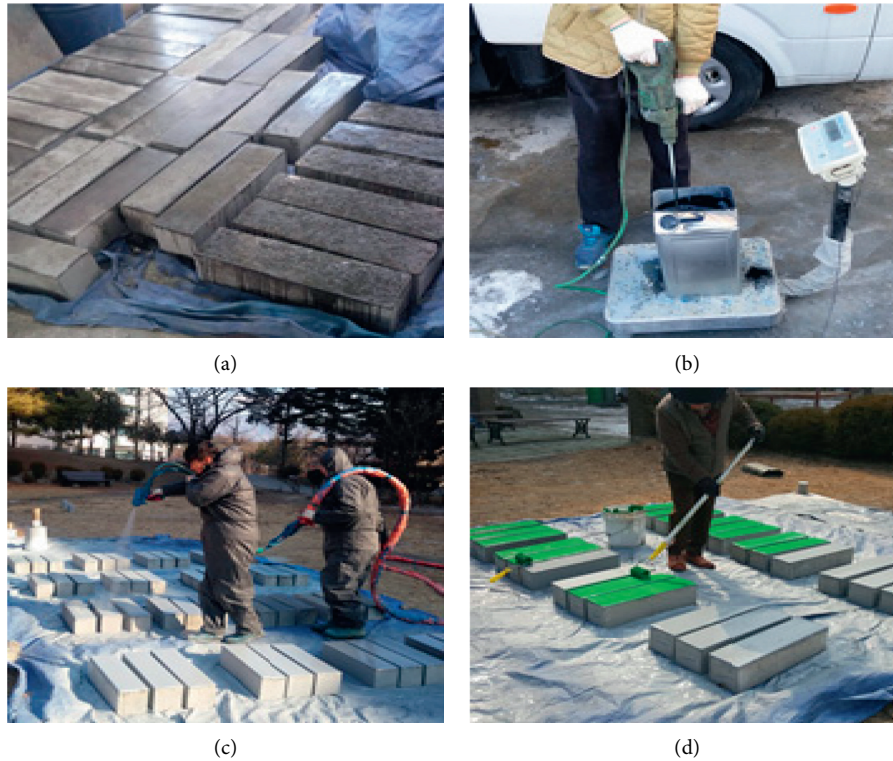


FIGURE 1: FRPU spraying operation: (a) primer painting; (b) mixing of prepolymer and fibers; (c) FRPU spraying; (d) primer painting.

double (5 mm) spraying is considered, and the weight-to-content ratio of the fiber is established as 5%, 7%, and 10% for steel and glass fibers, and 2%, 4%, and 6% for CNTs. The low ratio of the CNTs occurs because of the high cost and high volume from a due to low specific gravity. The steel fibers of 5 mm in length are scattered before the polyurea is sprayed owing to their difficulty in passing through the hose. The specimens are classified using the sign shown in Figure 2. In the figure, the characters S, F, and C denote the steel fibers, milled glass fibers, and CNTs, respectively. In addition, the next number is the weight-to-content ratio of the fibers, and the next numbers 1 and 2 denote the spraying thicknesses of 3 and 5 mm, respectively. The physical properties of FRPU reinforced using 2% CNTs are shown in Table 2. As the table indicates, the FRPU has a tensile strength of 12 N/mm² and an extension rate upon rupture of 240%. In addition, an improved flexural strength and ductility are expected.

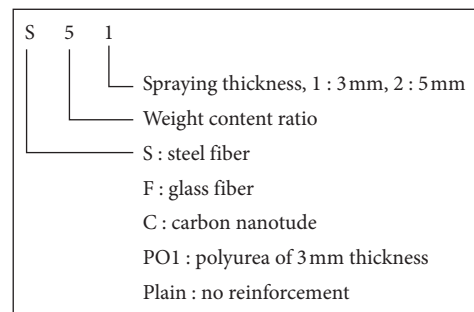


FIGURE 2: Specimen sign.

The five-week compressive strength of concrete after concrete casting is 28 MPa. The test beams are strengthened using polyurea or FRPU spraying three days in advance. The polyurea and FRPU act as a lateral reinforcement, leading to an enhanced strength and ductility. However, a polyurea-

TABLE 2: Physical properties of FRPU containing 2% CNT.

Item	Specification	Result
Amount of water absorption (g)		0.4
Water permeability resistance	KS F 4919	No penetration at 0.3 N/mm ² water pressure
Moisture permeability (m)		3.0
Permeation resistance of chloride ion (Coulombs)	KS F 4936	28
Tensile strength (N/mm ²)		12
Extension percentage at rupture (%)	KS F 4922	240
Bond strength (N/mm ²)		2.3

KS: Korean Standards.

reinforced concrete cylinder may be subjected to an eccentric load, and its accurate compressive strength can rarely be measured because the polyurea cannot be sprayed with a constant thickness along the circumferential surface. Figure 3 shows the failure mode of a polyurea-reinforced concrete cylinder through eccentric loading with an irregular expansion of the concrete cylinder. In addition, it is shown that the polyurea constrains the inner core concrete and fails by a loosening of the polyurea used to enclose the concrete pieces. This indicates that polyurea is effective in enhancing the ductility without a debonding.

Concrete beams of size 150 mm × 150 mm × 150 mm for testing the flexural strength are manufactured without reinforcing bars, and the load is applied at two points on the beam, as shown in Figure 4. The experiment results indicate the flexural performance including the load-carrying capacity and flexural ductility. The initial crack begins at the bottom face of the midspan section. The unreinforced concrete beam simultaneously fails with the advent of the initial cracking because of the low tensile strength of the concrete. The polyurea- and FRPU-reinforced concrete beams exhibit an abrupt reduction in the flexural strength the moment the initial cracking occurs. However, the load after the initial cracking gradually increases and is carried by the polyurea or FRPU on the tension side. The specimens reach the second peak load. The additional cracks are gradually propagated and widen around the midspan with an increase in the load. The polyurea or FRPU controls the development of cracks without peeling from the concrete surface.

Table 3 shows the peak load-carrying capacity, the second peak load, and the flexural ductility. The flexural ductility of the test beams is estimated based on the area under the load-deflection curve prior to failure. In addition, its ratio is calculated by dividing the ductility of FRPU-coated beams through the ductility of the polyurea-coated control beam. The peak load-carrying capacity ratio is determined as the peak load-carrying capacity of the polyurea- and FRPU-reinforced concrete beams with respect to that of the control beam. The peak load-carrying capacity of the FRPU-reinforced specimens was shown to be 1.0–1.53, which is as high as that of the polyurea-reinforced specimens, except for C62. The low-density CNTs have a high volume in FRPU. This can therefore lead to a discontinuous load-transferring path owing to the unevenness of the CNTs and the deteriorated flexural strength. In addition, all specimens except S51 represent a more improved flexural



FIGURE 3: Failure mode of polyurea-reinforced concrete cylinder.

ductility. The cause of the insufficient ductility of the S51 specimen is due to the uneven distribution of steel fibers owing to their nonuniform scattering prior to the spraying. After the occurrence of a concrete crack, the beam carries the additional load and reaches the second peak load. As indicated in Table 3, the second peak loads of the FRPU-reinforced specimens are higher than those of the polyurea-reinforced specimen, which is the reinforcement effect from the fibers.

Figure 5 shows the failure modes of the specimens. Upon initial loading, the flexure-resisting capacity is retained by the concrete, as well as the polyurea or FRPU. Upon the occurrence of the concrete cracks, the load abruptly deteriorates. Without a polyurea or FRPU reinforcement, the concrete beams abruptly fail under a load. The flexural capacity after the concrete cracks occurs is retained to a certain degree or even increased owing to the tensile strength of the polyurea or FRPU. The polyurea- or FRPU-reinforced concrete beams display a gradual increase in flexural ductility and deflection prior to ultimate failure. It was shown that the strengthened concrete beams ultimately fail through a fracture of the polyurea or FRPU.

Figure 6 shows the load-deflection curves of the specimens depending on the fiber types for a spray thickness of 3 mm. The plots are divided into three groups: (a) group 1 is CNTs strengthened by 2%, or milled glass or steel fibers strengthened by 5%, (b) group 2 is CNTs strengthened by 4%, or milled glass or steel fibers strengthened by 7%, and (c) group 3 is CNTs strengthened by 6%, or milled glass or

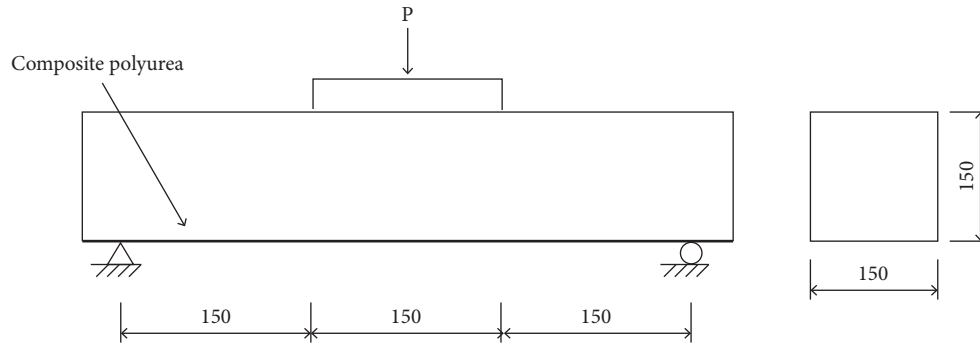


FIGURE 4: Loading system of concrete beam (unit: mm).

TABLE 3: Summary of experimental results.

Specimen	Load-carrying capacity		Second peak load (kN)	Flexural ductility	
	Peak (kN)	Ratio		Ductility (kN·mm)	Ratio
C21	24.41	1.20	10.35	138.36	1.98
C22	20.34	1.0	8.78	69.7	1.0
C41	21.49	1.06	13.43	135.6	1.95
C42	23.96	1.18	23.72	227.45	3.26
C61	23.1	1.14	15.85	160.1	2.30
C62	18.98	0.93	12.97	102.09	1.46
F51	22.25	1.09	11.61	97.74	1.40
F52	22.79	1.12	17.3	190.85	2.74
F71	23.99	1.18	22.6	231.77	3.32
F72	31.19	1.53	31.2	355.9	5.10
F101	23.2	1.14	20.38	188.33	2.70
F102	22.55	1.11	18.65	147.17	2.11
S51	21.45	1.05	13.6	58.56	0.84
S52	24.63	1.21	20.8	120.1	1.72
S71	22.12	1.09	17.38	116.57	1.67
S72	27.01	1.33	27.02	254.5	3.65
S101	21.43	1.05	15	85.4	1.22
S102	30.5	1.50	30.5	228.53	3.28
PO1	20.34	1.0	8.75	69.7	1.0
Plain	20.86			2.27	

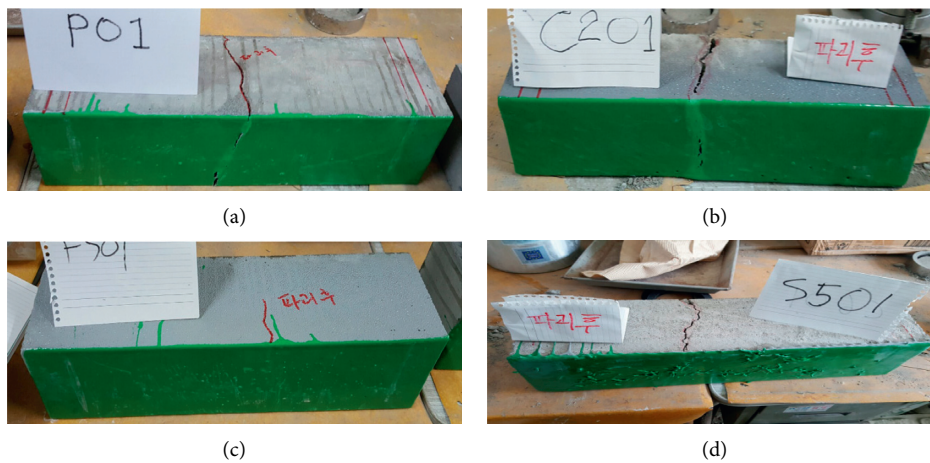


FIGURE 5: Failure mode of specimens: (a) PO1; (b) C21; (c) F51; (d) S51.

steel fibers strengthened by 10%. We assume that the beams ultimately fail when the load abruptly decreases after retaining sufficient ductility since the crack occurrence. It

was found that the polyurea- or FRPU-reinforced specimens retain sufficient flexural ductility owing to their expansibility. The specimens of group 1 in Figure 6(a) exhibit a

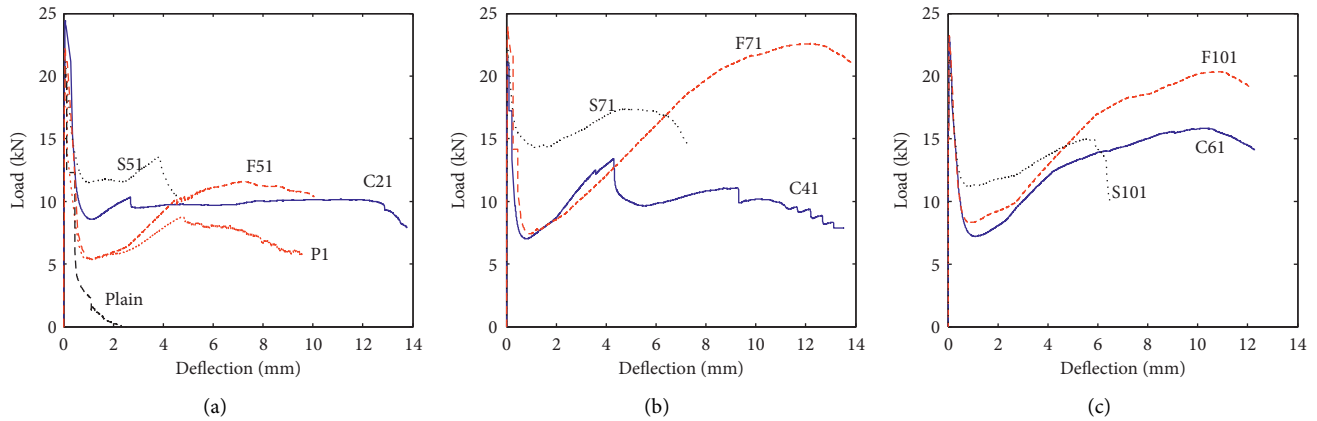


FIGURE 6: Load-deflection curves (spraying thickness of 3 mm): (a) group one; (b) group two; (c) group three.

similar load-deflection relationship prior to a concrete crack. Specimen C21 reinforced by CNTs also exhibits sufficient ductility. The specimens P1, F51, and S51 resist a load with a constant magnitude after a crack occurrence. The steel fibers of 5 mm in length are manually scattered on the beam surface prior to the polyurea spraying, and their even distribution cannot be expected. Thus, specimen S51 abruptly fails and exhibits little ductile behavior. It was found that the specimens reinforced by milled glass fibers or CNTs retain more load-carrying capacity and flexural ductility than those using polyurea only. The specimens of group 2 in Figure 6(b), which contain more fibers than those in group 1 in Figure 6(a), show a higher second peak load and more flexural ductility. Specimen C41 exhibits an abrupt load deterioration after the second peak load although the ductility is retained to a certain degree. The load deterioration in specimen C41 is caused by the uneven thickness of the FRPU and the uneven distribution of the CNT. It is difficult to obtain a precise and constant thickness because the spraying operation is manually conducted by experts. In addition, it is not easy to evenly disperse the fibers on the concrete surface. It has been shown that specimen F71 retains a high strength after concrete cracks occur, and thus the second peak load nearly reaches the peak load with an increase in the deflection. In group 3 in Figure 6(c), the specimen reinforced by steel fibers abruptly fails at a lower load than that in group 2. It has been estimated that an abrupt failure and low ductility are due to more irregular scattering with an increase in the weight-to-content ratio. It has been observed that the reinforcement by steel fibers has a limitation in the spraying operation regardless of the weight-to-content ratio. The specimen reinforced by CNTs in group 3, shown in Figure 6(c), exhibits a higher load-carrying capacity and more ductility after the cracking than that in group 2. The CNTs have a higher cost than the other fibers. In addition, the F101 specimen strengthened by milled glass fibers retains more load-carrying capacity and flexural ductility with an increase in the weight-to-content ratio.

Figure 7 shows the load-deflection curves of the specimens reinforced by FRPU of 5 mm in thickness. The load abruptly reduces upon the occurrence of the first flexural

concrete cracking. After this stage, the load is resisted by the FRPU at the flexural tension face and gradually increases with the deflection. Compared with specimens of 3 mm in thickness, the increase in spraying thickness leads to an enhancement in the load-carrying capacity as well as the flexural ductility. This is due to the increase in the tension-resisting area and the corresponding force. The plots also indicate that the toughness and dissipated energy increase with an increase in the weight-to-content ratio. The specimens reinforced by steel fibers exhibit an enhanced peak load-carrying capacity with an increase in the weight-to-content ratio and the highest flexural ductility at the weight-to-content ratio of 7%. However, it is difficult to state that the most effective ratio is 7% because of the uneven coating thickness of the FRPU and the nonuniform distribution of the steel fibers. The concrete beams reinforced by 2% or 6% CNTs rarely display more load-carrying capacity and flexural ductility than at a weight-to-content ratio of 4%. Based on the synthetic prediction shown in Figure 7, we can predict that the optimum weight-to-content ratio is approximately 4%. The specimens containing milled glass fibers depending on the weight-to-content ratio exhibit an extremely similar tendency as those using CNTs. The optimum weight-to-content ratio of glass fibers should be approximately 7% in terms of economy and strength.

Figure 8 compares the strengthening effect depending on the weight-to-content ratio of the reinforcement fibers and coating thickness. It can be expected that the load-carrying capacity and flexural ductility should be enhanced with an increase in the coating thickness or weight-to-content ratio because of the increased flexure-resisting strength. However, the C2, C6, and F10 series specimens represent the deteriorated load-carrying capacity and flexural ductility despite the increased coating thickness. It can be estimated that the results are derived from the uneven thickness of the FRPU, as well as the discontinuous and nonuniform distribution of the fibers. The specimens reinforced by steel fibers exhibit an enhanced load-carrying capacity and flexural ductility. However, the specimens of the S10 series represent less flexural ductility than of the S7 series because of the nonuniform distribution through an excessive steel fiber content. It has been

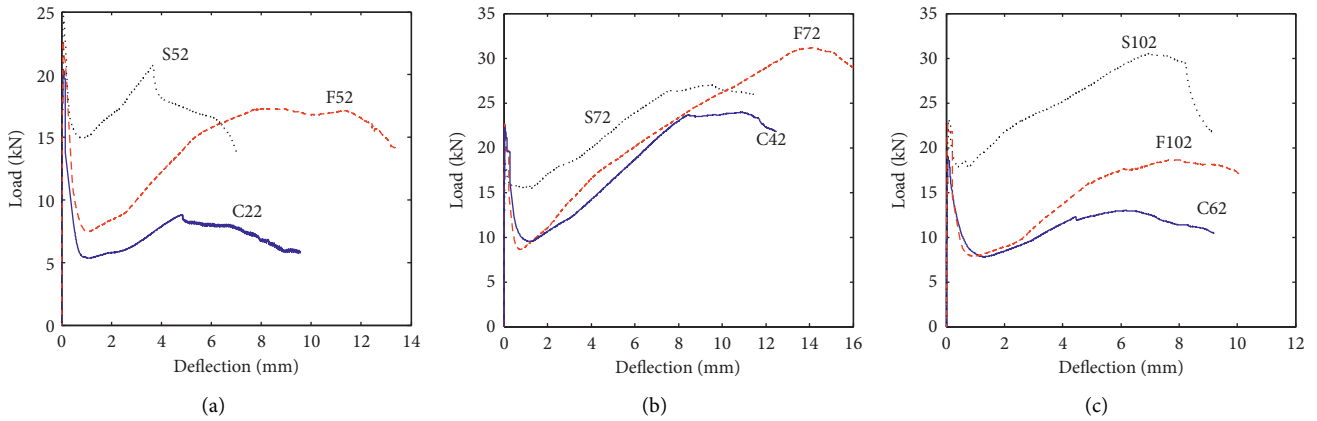


FIGURE 7: Load-deflection curves (spraying thickness of 5 mm): (a) group one; (b) group two; (c) group three.

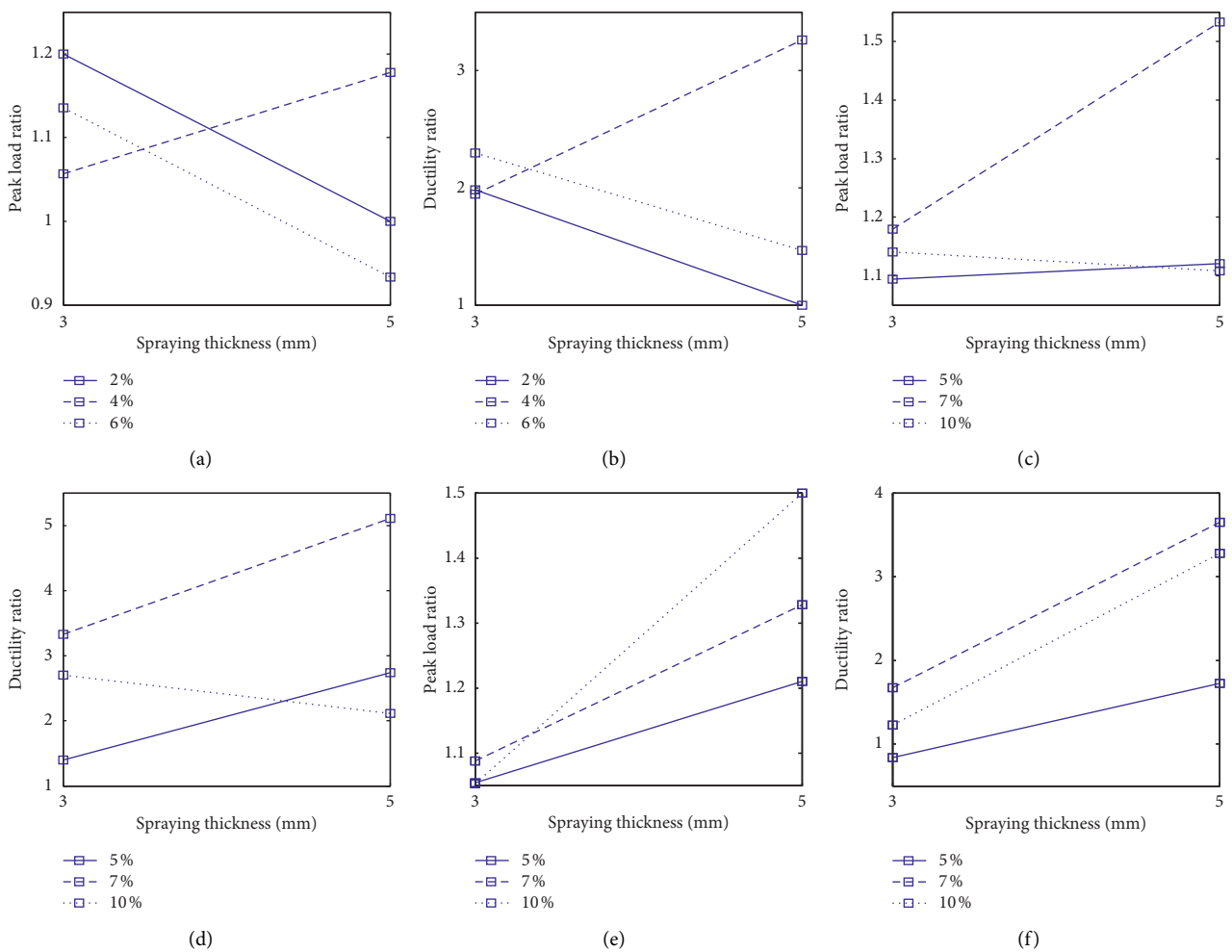


FIGURE 8: Peak load ratio and ductility ratio according to spraying thickness: (a) C series-load ratio; (b) C series-ductility ratio; (c) F series-load ratio; (d) F series-ductility ratio; (e) S series-load ratio; (f) S series-ductility ratio.

demonstrated that the specimens of the C4, F5, and F7 series retain a stable load-carrying capacity and flexural ductility upon the variation of the coating thickness and weight-to-content ratio of the fibers in comparison with the other specimens. It can be concluded from the experiments that the

FRPU method reinforced by 5% or 7% milled glass fibers is the most effective in terms of the economy, strengthening, and construction of all reinforcements.

This observation can be seen in Figure 9, which shows that the 4% CNT specimens have an enhanced load-carrying

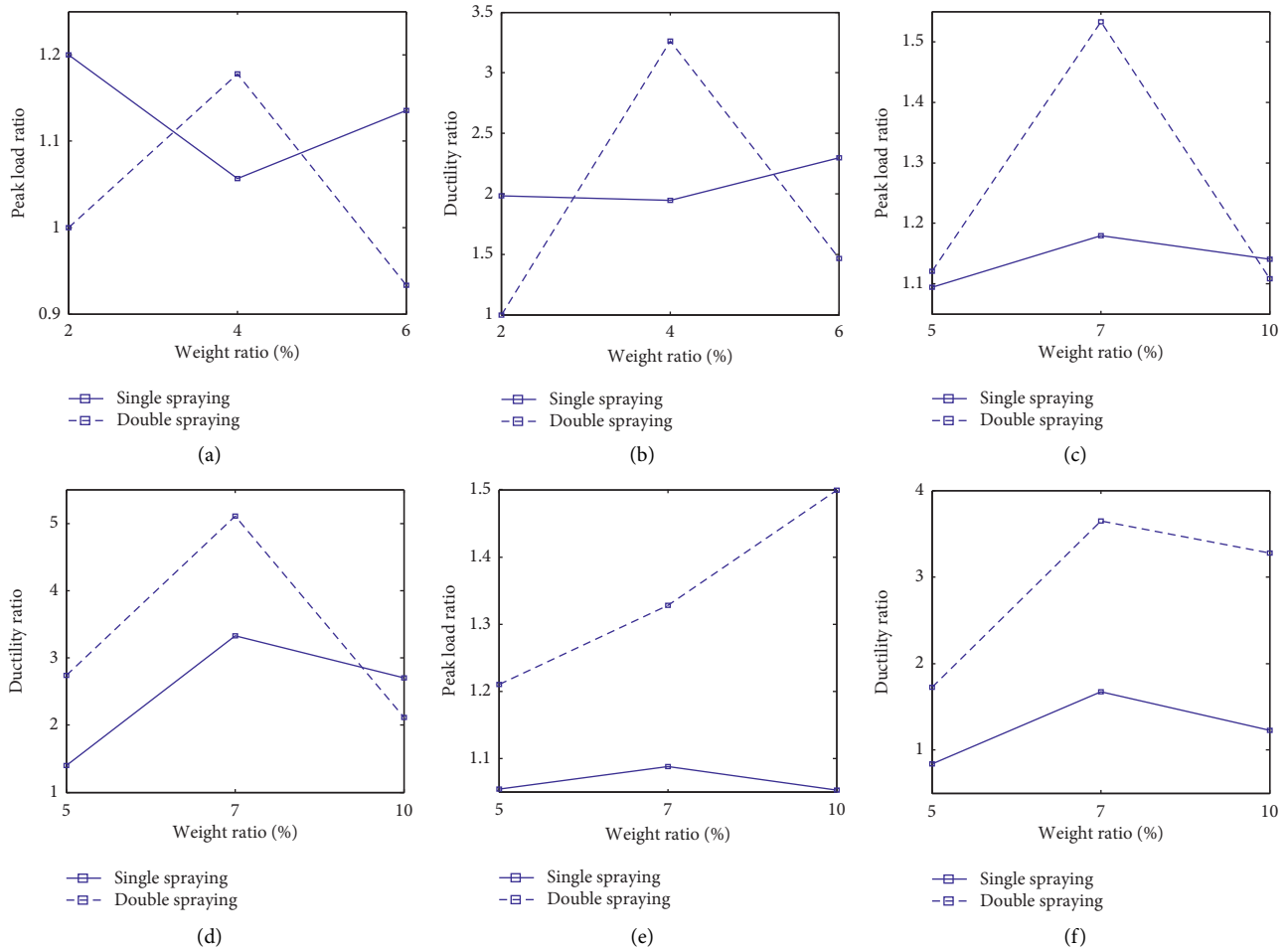


FIGURE 9: Peak load ratio and ductility ratio according to weight ratio: (a) CNT-load ratio; (b) CNT-ductility ratio; (c) glass fiber-load ratio; (d) glass fiber-ductility ratio; (e) steel fiber-load ratio; (f) steel fiber-ductility ratio.

capacity and flexural ductility. In addition, the specimens of 5% or 7% milled glass fibers exhibit stable results in enhancing the load-carrying capacity and flexural ductility. The specimens reinforced by steel fibers show an enhanced load-carrying capacity and flexural ductility with an increase in the coating thickness. However, this strengthening method has difficulty in terms of spraying, and a definite increase in the load-carrying capacity and flexural ductility can rarely be expected owing to the discontinuous flexural loading path through the nonuniform distribution of the steel fibers.

3. Conclusions

This study investigates the applicability of the FRPU coating technique in the retrofitting of concrete structures. The FRPU coating approach can avoid a failure by debonding from the concrete surface. The test parameters include the fiber type, such as glass, carbon, and steel fibers, the coating thickness, and the fiber weight-to-content ratio. The reinforcement by steel fibers has a limitation in terms of a spraying operation regardless of the weight-to-content

ratio, because fibers should be manually scattered on the member surface prior to spraying. The FRPU approach when applying CNTs has a difficulty in terms of the flexural capacity, because the low-density CNTs make up a high volume of the FRPU, which is a disadvantage owing to the expansiveness. The specimens with 5% or 7% milled glass fibers exhibit stable results in enhancing the load-carrying capacity and flexural ductility. This experiment indicates that the FRPU coating approach using milled glass fibers is more effective than the application of CNTs or steel fibers for enhancing the load-carrying capacity and improving the flexural ductility.

Data Availability

The data used to support the findings of this study are included within the article.

Conflicts of Interest

The authors declare that there are no conflicts of interest regarding the publication of this paper.

References

- [1] S. Parniani and H. Toutanji, "Monotonic and fatigue performance of RC beams strengthened with a polyurea coating system," *Construction and Building Materials*, vol. 101, no. 1, pp. 22–29, 2015.
- [2] A. E. Marawan, A. S. Debaiky, and N. N. Khalil, "Shear and flexural behavior of R.C. beams strengthened with polyurea spray," *International Journal of Advance Research in Science and Engineering*, vol. 4, no. 11, pp. 12–26, 2015.
- [3] K. Kamonchaivanich, K. Kuboyama, and T. Ougizawa, "Effect of elastic modulus and position of polyurea coating on flexural strength of coated ceramic tiles by experiments and finite element analysis," *Journal of Coatings Technology and Research*, vol. 16, pp. 1–11, 2019.
- [4] O. Gedik, C. Demir, and A. Ilki, "Effect of unconfined concrete strength on the strength and deformability predictions of FRP confined concrete," in *Proceedings of the Second Official International Conference of International Institute for FRP in Construction for Asia-Pacific Region*, pp. 265–270, Seoul, Korea, December 2009.
- [5] M. Samaan, A. Mirmiran, and M. Shahawy, "Model of concrete confined by fiber composites," *Journal of Structural Engineering*, vol. 124, no. 9, pp. 1025–1031, 1998.
- [6] H. Toutanji, "Stress-strain characteristics of concrete columns externally confined with advanced fiber composite sheets," *ACI Materials Journal*, vol. 96, no. 3, pp. 397–404, 1999.
- [7] Y. Xiao and H. Wu, "Compressive behaviour of concrete confined by carbon fiber composite jackets," *Journal of Materials in Civil Engineering*, vol. 12, no. 2, pp. 139–146, 2000.
- [8] A. Ilki and N. Kumbasar, "Compressive behaviour of carbon fibre composite jacketed concrete with circular and non-circular cross-sections," *Journal of Earthquake Engineering*, vol. 7, no. 3, pp. 381–406, 2003.
- [9] L. Lam and J. G. Teng, "Design-oriented stress-strain model for FRP-confined concrete," *Construction and Building Materials*, vol. 17, no. 6–7, pp. 471–489, 2003.
- [10] G. Manfredi and R. Realfonzo, "Models of concrete confined by fiber composites," in *Proceedings of the 5th International Conference on Fibre-Reinforced Plastics for Reinforced Concrete Structures, FRPRCS5*, vol. 1, pp. 865–873, London, UK, July 2001.
- [11] D. S. A. Gideon and P. Alagusundaramoorthy, "Flexural retrofit of RC beams using CFRP laminates," *IOP Conference Series: Materials Science and Engineering*, vol. 431, no. 7, Article ID 072006, 2018.
- [12] A. Li, C. Diagana, and Y. Delmas, "Shear strengthening effect by bonded composite fabrics on RC beams," *Composites Part B: Engineering*, vol. 33, no. 3, pp. 225–239, 2002.
- [13] M. B. S. Alferjani, A. A. B. A. Samad, B. S. Elrawaff, N. B. Mohamad, and M. H. B. Ahmad, "Shear strengthening of reinforced concrete beams using carbon fiber reinforced polymer laminate: a review," *American Journal of Civil Engineering*, vol. 2, no. 1, pp. 1–7, 2014.
- [14] T. B. Carlos, J. P. C. Rodrigues, R. C. A. De Lima, and D. Dhima, "Experimental analysis on flexural behaviour of RC beams strengthened with CFRP laminates and under fire conditions," *Composite Structures*, vol. 189, no. 1, pp. 516–528, 2018.
- [15] S. F. Brena, R. M. Bramblett, S. L. Wood, and M. E. Kreger, "Increasing flexural capacity of reinforced concrete beams using carbon fiber-reinforced polymer composites," *ACI Structural Journal*, vol. 100, no. 1, pp. 36–46, 2003.
- [16] S. F. Brena and B. M. Macri, "Effect of carbon-fiber-reinforced polymer laminate configuration on the behavior of strengthened reinforced concrete beams," *Journal of Composites for Construction*, vol. 8, no. 3, pp. 229–240, 2004.
- [17] P. J. Fanning and O. Kelly, "Ultimate response of RC beams strengthened with CFRP plates," *Journal of Composites for Construction*, vol. 5, no. 2, pp. 122–127, 2001.
- [18] P. Alagusundaramoorthy, I. E. Harik, and C. C. Choo, "Flexural behavior of R/C beams strengthened with carbon fiber reinforced polymer sheets or fabric," *Journal of Composites for Construction*, vol. 7, no. 4, pp. 292–301, 2003.
- [19] F. Ceroni, "Experimental performances of RC beams strengthened with FRP materials," *Construction and Building Materials*, vol. 24, no. 9, pp. 1547–1559, 2010.
- [20] H. V. S. Gangarao and P. V. Vijay, "Bending Behavior of Concrete Beams Wrapped with Carbon Fabric," *Journal of Structural Engineering*, vol. 124, no. 1, pp. 3–10, 1998.
- [21] G. Spadea, F. Bencardino, and R. N. Swamy, "Structural behavior of composite RC beams with externally bonded CFRP," *Journal of Composites for Construction*, vol. 2, no. 3, pp. 132–137, 1998.
- [22] T. Uomoto, H. Mutsuyoshi, F. Katsuki, and S. Misra, "Use of fiber reinforced polymer composites as reinforcing material for concrete," *Journal of Materials in Civil Engineering*, vol. 14, no. 3, pp. 191–209, 2002.
- [23] H. K. Mahiyar and M. Soni, "An experimental study of flexural strength of concrete beam reinforced with fiber reinforced polymer," *International Research Journal of Engineering and Technology*, vol. 4, no. 11, pp. 1933–1939, 2017.
- [24] C. E. Greene and J. J. Myers, "Flexural and shear behavior of reinforced concrete members strengthened with a discrete fiber-reinforced polyurea system," *Journal of Composites for Construction*, vol. 17, no. 1, pp. 108–116, 2013.
- [25] N. L. Carey and J. J. Myers, "Discrete fiber reinforced polymer systems for repair of concrete structures: polyurea-fiber characterization results," *American Concrete Institute*, vol. 275, no. 16, pp. 1–14, 2011.

Research Article

Experimental Study on the Structural Performance Degradation of Corrosion-Damaged Reinforced Concrete Beams

Ju-Seong Jung,¹ Bang Yeon Lee ,² and Kang-Seok Lee ³

¹Department of Architectural Engineering, Hanyang University, Seoul, Republic of Korea

²School of Architecture, Chonnam National University, Gwangju, Republic of Korea

³Department of Architectural Engineering, Hanyang University, Ansan, Republic of Korea

Correspondence should be addressed to Kang-Seok Lee; ksleenist@hanyang.ac.kr

Received 20 June 2019; Accepted 16 September 2019; Published 16 October 2019

Guest Editor: Charis Apostolopoulos

Copyright © 2019 Ju-Seong Jung et al. This is an open access article distributed under the Creative Commons Attribution License, which permits unrestricted use, distribution, and reproduction in any medium, provided the original work is properly cited.

It is very important to investigate the effects of the seismic performance of corrosion-damaged reinforced concrete (RC) members, in terms of their strength and lateral deformability, on the seismic performance of entire building systems. Such investigation allows accurate evaluation of the seismic performance of RC structures with corroded members, including beams and columns. However, current techniques for evaluating the seismic performance of existing RC structures do not take the effects of deterioration (including the corrosion of reinforcing bars) on the performance of RC members into account. The main objective of this research is to propose a practical methodology for evaluating the seismic performance of RC buildings with corrosion-damaged members. We extrapolate a structural performance degradation factor from the strength-deformation capability of corroded members to allow direct quantitative evaluation of their seismic performance. In this study, as a first step toward achieving this goal, we experimentally investigated the effect of reinforcing bar corrosion on the behavior of RC beams and the structural performance degradation factor. Our analysis was based on the strength-deformation capabilities of corrosion-damaged beams. We also propose a relationship between the half-cell potential of corroded reinforcing bars and the structural performance degradation behavior of RC beams. Our results indicate that there is a relatively strong correlation between the performance degradation factor and the average potential difference, with coefficients of determination (R^2) of the flexural and shear beams of 0.78 and 0.91, respectively. The potential difference, which was measured using the half-cell measurement method, can serve as one of the indicators of relative structural degradation, but we must ensure that the environmental measurement conditions are held constant.

1. Introduction

Reinforced concrete (RC) structures are the most common structural systems in modern society, due to their low construction and maintenance costs and high durability compared to other types of structures. The structural performance of RC structures, however, deteriorates over time for various reasons, such as changes in the environmental conditions, design load, and material properties, as well as structural design errors and defective construction. Among these factors, reinforcement corrosion is one of the primary causes of deterioration, affecting a large number of RC structures [1–10]. This results in a shortened service life and reduced structural performance (Figure 1).

Major causes of this corrosion include chloride and carbonation, arising from elements of the atmosphere or surrounding environment such as the sea, de-icing salts, and pollution. Hansson [1] and Shamsad [4] investigated the corrosion mechanism of steel bars and the effects of corrosion on RC members; structural deterioration was found to proceed according to the following stages: (1) Formation of white patches: atmospheric carbon dioxide reacts with calcium hydroxide in the cement paste, forming calcium carbonate. This calcium carbonate is carried by moisture and deposited onto the concrete surface, forming white patches. (2) Brown patches in reinforced areas: when a steel bar starts to corrode, a layer of iron oxide is formed on top of the bar, which is carried to the surface of the concrete by moisture. (3) Formation of



FIGURE 1: Structural performance deterioration of a reinforced concrete (RC) structure caused by reinforcement corrosion [10].

cracks: the corrosion products occupy more space than the original material; hence, they exert pressure on the concrete and crack it. As more corrosion occurs, additional, wider cracks are formed. (4) Spalling of concrete cover: due to loss of the bond between concrete and steel, the concrete starts forming multiple layers of scales and peels off. The sizes of the steel bars are also reduced. (5) Snapping of bars: due to a reduction in the size of the steel bars, they ultimately snap. The main bars also show a considerable reduction in size. (6) Buckling of bars: spalling of the concrete cover and snapping of bars lead to buckling of the main bars. This causes the concrete to bulge and can affect the integrity and life of the RC structures.

The decrease in yield strength resulting from the reduction of the effective area of the steel rebar reduces the tensile force that the steel rebar can resist. Furthermore, the compressive strength of concrete is reduced by spalling of its surfaces. As a result, the entire structure collapses due to the severe structural performance deterioration.

There have also been frequent earthquakes all over the world in recent years. If RC structures in earthquake-prone areas are seriously corroded, this will inevitably affect their seismic performance and safety. As shown in Figure 2, reinforcement corrosion of RC members has a significant impact on the structural performance deterioration (i.e., seismic performance degradation) caused by earthquakes [7], as seen following recent strong earthquakes including the 1995 Kobe Earthquake in Japan ($M=7.3$), the 1999 Jiji Earthquake in Taiwan ($M=7.3$), the 1999 Izmit Earthquake in Turkey ($M=7.4$), the 2008 Sichuan Earthquake in China ($M=8.0$), the 2010 Chile Earthquake ($M=8.8$), the 2012 Great East Japan Earthquake ($M=9.0$), the 2013 Lushan Earthquake in China ($M=7.0$), and the 2016 Kumamoto Earthquake in Japan ($M=7.0$).

Even though the intensity of the earthquakes was relatively low, we can see from observations of buildings damaged during the 2004 Niigata-ken Chuetsu Earthquake in Japan ($M=6.8$), as well as the 2017 Pohang Earthquake in Korea ($M=5.4$), that corrosion of RC members, including beams and columns, affected failure, as shown in Figure 3. The corrosion of steel leads to a loss of adherence between the reinforcement and concrete over time, in addition to significant losses in cross sections of reinforcement bars. As a result of these losses, reinforcement bars and concrete no

longer work in concert, such that the structural element loses a significant amount of its lateral load-carrying capacity.

Therefore, it is of great importance to investigate the effects of seismic performance, in terms of the strength and lateral deformability of corrosion-damaged RC members, on the seismic performance of the entire building system. This will enable us to accurately evaluate the seismic performance of RC structures with corroded members, including beams and columns.

However, current techniques for evaluating the seismic performance of existing RC structures, including those described in the Federal Emergency Management Agency guidelines FEMA 274 [11], FEMA 310 [12], and the Japan Building Disaster Prevention Association standard [13], do not fully take into account the influence of deterioration on the performance of RC members, including corrosion of steel bars.

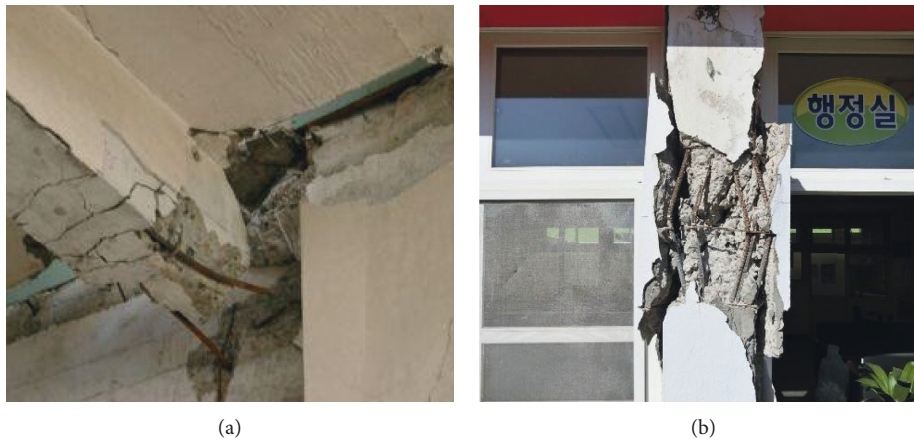
According to the FEMA 274 [11] and 310 [12] guidelines, the seismic performance of RC buildings should be evaluated by taking the extent of the damage and impact on the capacity of each deteriorated member into account. Deterioration of concrete and reinforcing steel can significantly reduce the lateral strength of concrete members. Site inspection may be required to assess the effects of deterioration of concrete and reinforcing steel. However, assessment of the seismic performance of RC buildings, including the influence of corrosion-damaged members, is simply based on heuristic judgments when following the FEMA 310 guideline, which does not specify any quantitative analysis procedure.

The Japanese standard [13] evaluates the seismic performance of existing RC buildings at each story, and in each direction, using the following seismic capacity index I_S : $I_S = E_O \times S_D \times T$. In this equation, E_O is the basic structural performance index calculated with respect to the ultimate horizontal strength, ductility, number of stories, and specific story concerned. S_D (irregularity index) is a subindex of the structural design that is used to modify E_O according to irregularities in the building shape and the distribution of stiffness along the building height. T (time index) is a subindex of the time-dependent deterioration of a building and is used to modify E_O according to deterioration of strength and ductility.

The time index is acquired via site inspections assessing the effects of structural deterioration and aging. This requires an initial inspection, a follow-up inspection, and more detailed additional inspections. During the initial inspection, $T=0.8$ is adopted for buildings that are over 30 years old, while $T=0.9$ is used in cases with significant spalling of the internal finishing. The smallest T values derived from the site inspection should be multiplied by E_O given above. In the follow-up and additional detailed inspections, $T_i=0.05$ is adopted if more than one-third of the total members inspected in each direction have corroded reinforcing bars (here, T_i is the time index for the story inspected, i). Finally, on the basis of the weighted T_i value of each inspected story, as well as the condition of members including beams and columns, the overall T is used to evaluate the seismic performance of aged RC buildings, which deteriorates with



FIGURE 2: Corrosion of RC members damaged during the 1999 Izmit Earthquake in Turkey [7].



(a)

(b)

FIGURE 3: Corrosion of RC beams and columns damaged during earthquakes. (a) The 2004 Niigata-ken Chuetsu Earthquake in Japan (b) The 2017 Pohang Earthquake in Korea.

corrosion. Compared to the FEMA 274 and 310 guidelines, the Japanese standard can be used to quantitatively evaluate the seismic performance of RC buildings, taking into account the influence of corrosion-damaged members by using T described in the equation. However, the strength-ductility degradation relationship between I_s and T , which is used to modify E_O , is not robust: the Japanese standard is an indirect evaluation methodology.

In previous studies, the seismic performance of RC structures was mainly assessed based on the strength and deformation capability of the building structure itself, i.e., by using a structural analysis program based on structural drawings and the measured material strength. In this case, the durability reduction factor is calculated directly and quantitatively, taking into account the deterioration of corrosion-damaged RC members, in addition to an indirect and qualitative assessment, for evaluating the seismic performance of RC structures.

Few studies on seismic performance have taken into account the influence of deterioration of corroded RC members [7, 14], and the quantitative reduction factor, based on the strength-deformation capability of corrosion-

damaged members relative to unaffected members, has not been determined conclusively. Different surveys, reports, and studies have highlighted that the corrosion of reinforcements is the main cause of deterioration of RC members [15, 16].

Therefore, the seismic performance of RC buildings with corrosion-damaged members should be evaluated quantitatively and directly, using a structural performance reduction factor based on the strength-deformation capability, i.e., energy dissipation capability. This will enable accurate evaluation of the seismic performance of RC structures.

The main objective of this research is to propose a practical methodology for evaluating the seismic performance of RC buildings with corrosion-damaged members. A structural performance degradation factor derived from the strength-deformation capability of corroded members is used to evaluate their seismic performance, quantitatively and directly.

Various techniques have been applied to determine the rate and pattern of corrosion in RC structures [17]. One of the most popular techniques is electrochemical measurement, which enables evaluation of corrosion-related parameters

such as the half-cell potential, concrete resistivity, and corrosion current density [4]. Half-cell potential can be used to determine the corrosion tendency via a reference electrode and a voltmeter. Half-cell potential was used by Pradhan and Bhattacharjee [18] to establish an indicator of corrosion initiation for concrete structures. Due to its simplicity and cost-effectiveness, the corrosion potential measurement method has been widely used for testing the corrosion of reinforcing bars in RC structures [19].

In this study, as a first step toward achieving the main research objective stated above, the effects of reinforcing bar corrosion on the behavior of RC beams and the structural performance degradation factor, which is based on the strength-deformation capability of corrosion-damaged beams, were investigated experimentally.

For this purpose, two types of beams were designed; 8 specimens were used to assess the flexural failure of beams and 8 to assess the shear failure of beams; thus, 16 specimens were used in total. The impressed current technique was applied to assess the accelerated corrosion of the reinforcing bar. For the beam test, we used a four-point bending test under simply supported conditions. The corrosion potential of the reinforcing bar was quantitatively measured based on the half-cell potential, as described previously. We then evaluated the relationship between the performance degradation factor and average potential difference, in terms of voltage, for corrosion-damaged RC beams subjected to flexure and shear.

2. Experimental Program

2.1. Materials. We used concrete with a compressive strength of 24.4 MPa. Cylindrical specimens were cast at the same time as the beams were manufactured and cured, under the same curing conditions. The compressive strength was measured using cylindrical specimens with dimensions $\phi 100 \times 200$ mm according to ASTM C39/C39M [20]. D16 and D13 deformed reinforcing bars, with a yield strength of 460 MPa and ultimate strength of 495 MPa, were used as longitudinal reinforcing bars and stirrups, respectively. The yield strength and ultimate tensile strength of the reinforcing bars were measured according to ASTM E8/E8M [21].

2.2. Design and Manufacture of Beams. To investigate the effect of corrosion of reinforcing bars on the flexural and shear behaviors of RC beams according to ACI 318 Building Code, two types of beams (16 specimens in total) were designed [22]. As shown in Figure 4, all specimens had a total length of 2,200 mm. The flexural failure type beams had a cross section of 150×250 mm, and the shear failure type beams had a cross section of 200×300 mm. The shear span ratio (a/d) of the shear failure type beam was equal to 3.

The flexural failure type beam was designed to have longitudinal reinforcements in the form of two D13 bars (tension) and two D10 bars (compression), as well as shear reinforcements in the form of D10 bars at 150 and 100 mm, with a closed-loop stirrup used in the pure bending region and the region between the support and load points. The

shear failure type beam was designed to have longitudinal reinforcements of three D13 bars in tension and two D10 bars in compression and shear reinforcements in the form of D10 bars at 150 and 100 mm, with an open-loop stirrup used in the pure bending region and the region between the support and load points. Specimens F-B0 and S-B0 were used as control flexural and shear failure type beam specimens, respectively, without corroded reinforcing bars. Specimens FB-C0 to FB-C7 and SB-C0 to SB-C7 were sequentially degraded by reinforcing bar corrosion. To accelerate the corrosion of the reinforcing bar, a copper wire was embedded at a position 450 mm from the support, as shown in Figure 4.

We manufactured the beam specimens by assembling a reinforcing bar cage, as shown in Figure 5. Next, the wire for accelerating the corrosion of the reinforcing bar was installed and the reinforcing bar cage was placed within the formwork. Finally, the concrete was placed in the specimen.

2.3. Accelerated Corrosion of Reinforcing Bars. The impressed current technique was adopted to accelerate the corrosion of the reinforcing bar. The beam specimens were placed in a tank 30 days after casting, as shown in Figure 6; 5% NaCl solution was used as an electrolyte. The solution level in the tank was adjusted to be approximately 2 cm below the top surface of the beams, to ensure adequate submersion of all reinforcing bars. Then, the beam specimens were incorporated with a direct current power supply. We used an embedded reinforcing bar as the anode and an external stainless-steel plate as the cathode, to accelerate the corrosion of the reinforcing bar. To simulate structural degradation of the reinforced beam according to the degree of corrosion of the reinforcing bar, the duration of the accelerated corrosion process was included as a test variable. The duration of the accelerated corrosion was increased with increasing beam specimen number to produce the desired sequential structural damage to the beams. The FB-C1 to FB-C7 and SB-C1 to SB-C7 specimens were sequentially removed from the tank and dried out. Then, the potential field on the concrete surface was measured using a half-cell electrode and a high-impedance voltmeter; this voltmeter is one of the devices recommended for measuring corrosion potential in ASTM C876 [23]. The measurement area was covered laterally by six points within ± 20 cm of the center line of the copper wire, which was embedded at a position 450 mm from the support, and vertically by four points at intervals of 62.5 cm for the flexural failure type beam and 75 cm for the shear failure type beam. Thus, there were 24 measurement points (4 points in each row and 6 points in each column) in total for each beam.

2.4. Test Program. All beams were subjected to a four-point bending test under conditions of limited support, as shown in Figure 7. The pure bending span between the two loading points was 600 mm for the flexural failure type beam and 500 mm for the shear failure type beam. The bending test was performed using a universal testing machine. A monotonic transverse load was applied under load control (loading

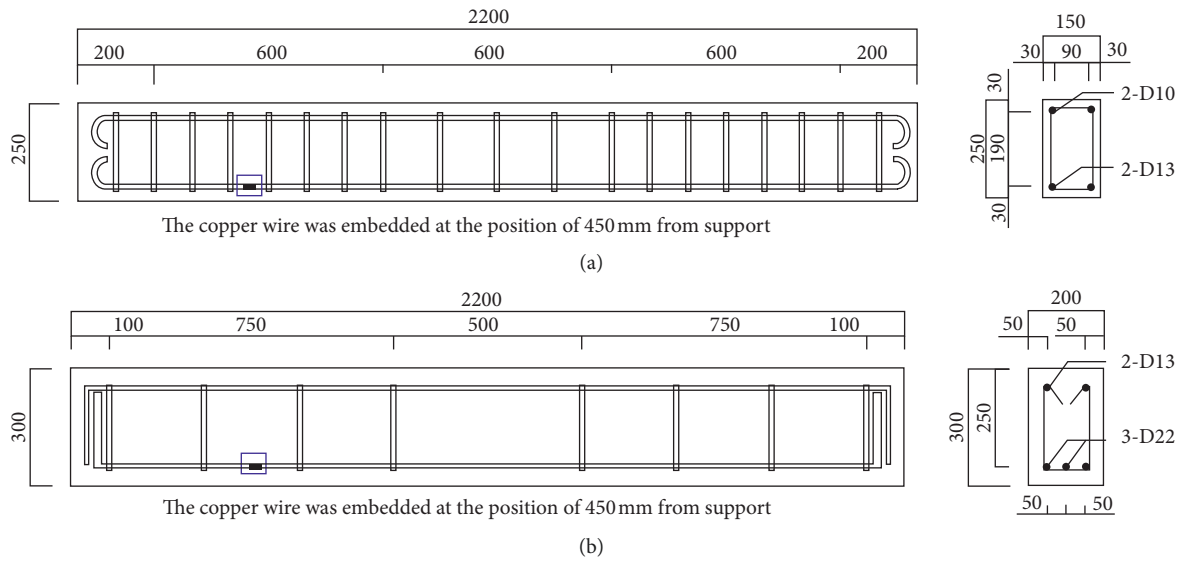


FIGURE 4: Reinforcement details of beams: (a) flexural failure type beam and (b) shear failure type beam.

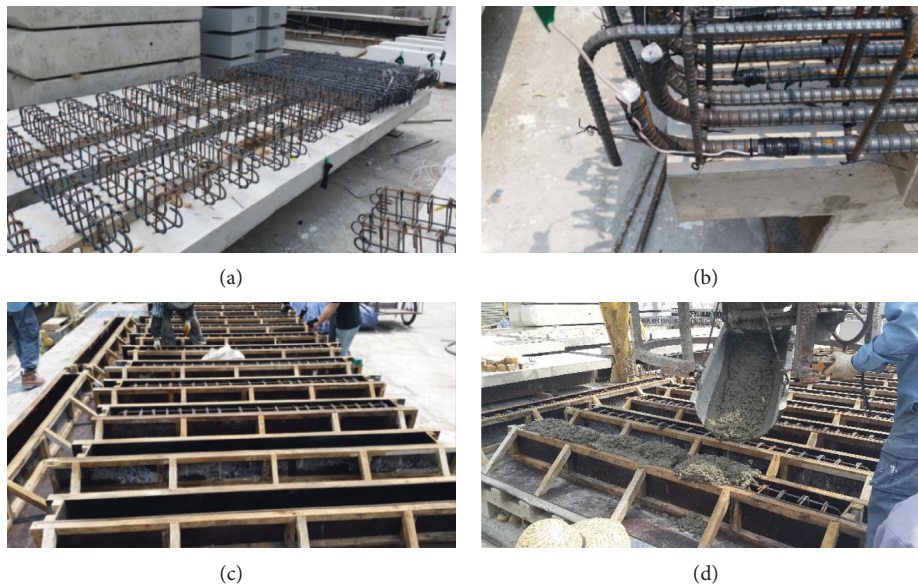


FIGURE 5: Beam manufacturing process: (a) assembly of reinforcing bar cage, (b) wire for corrosion of reinforcing bar, (c) installation of reinforcing bar cage, and (d) placement of concrete.

speed of 20 kN/min) until the load reached 50% of the expected maximum load. Then, load was applied under displacement control at a loading speed of 0.7 mm/min. After the peak load was reached, a further load was applied until the load reached 70% of the peak load and then released. Deflection at the midspan of each specimen was measured using linear variable differential transducers.

3. Results and Discussion

3.1. Half-Cell Potential of Reinforced Concrete Beam. In this study, the corrosion potential of the reinforcing bar is measured by using the CANIN+ corrosion analyzing instrument developed by Proceq [23]. On the basis of the

standard specified in ASTM C876 [24], the temperature was set to approximately 28°C for the measurement of the corrosion potential of reinforcing steel embedded in concrete. The results of the quantitative measurements (average voltage measured at 24 points) of the corrosion potential of the reinforcing bar in each beam are summarized in Table 1.

The half-cell potential of the reinforcing bars of the FB-C1 to FB-C7 and SB-C1 to SB-C7 specimens increased sequentially, i.e., increased with increased duration of the accelerated corrosion process. Figures 8 and 9 show the half-cell potential map of each measurement point.

According to ASTM C876 [24], if potentials over an area are more positive than -200 mV CSE (copper sulfate electrode), there is a greater than 90% probability that no

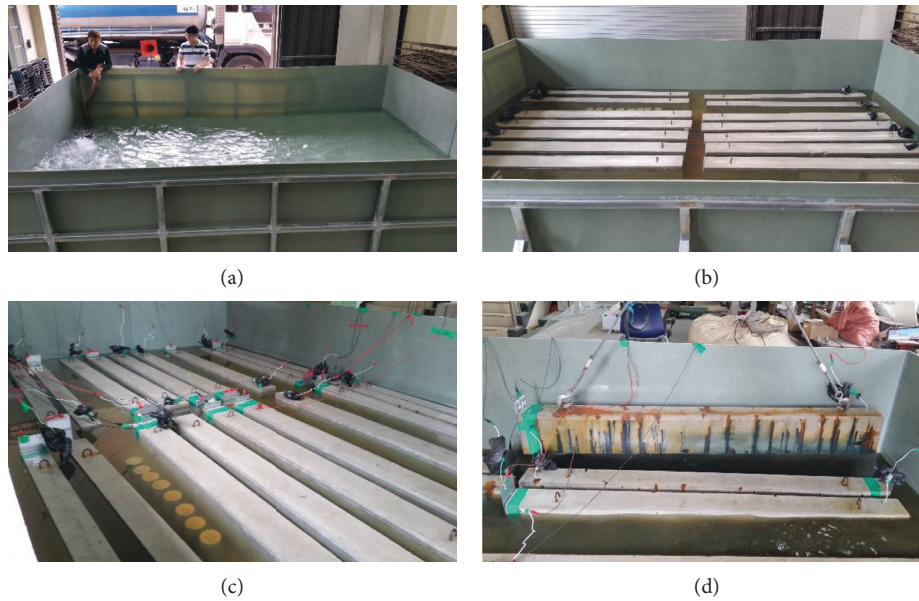


FIGURE 6: Accelerated corrosion setup: (a) tank with 5% NaCl solution, (b) immersion of beam, (c) accelerated corrosion, and (d) corroded beam.



FIGURE 7: Test setup.

TABLE 1: Average potential difference in voltage (unit: mV CSE).

Type of beam	C0	C1	C2	C3	C4	C5	C6	C7
FB-C series*	-63	-254	-265	-280	-292	-298	-374	-700
SB-C series**	-171	-269	-344	-551	-576	-659	-700	-700

*Beams controlled by flexure.**Beams controlled by shear.

corrosion of the reinforcing bar is occurring in that area at the time of the measurement. If the potentials over an area are more negative than -350 mV CSE, there is a greater than 90% probability that corrosion of the reinforcing bar is occurring in that area at the time of measurement. The half-cell potentials of the control beams, i.e., the FB-C0 and SB-C0 beams, which were not subjected to the accelerated corrosion process, were higher than -200 mV CSE. On the other hand, other beams with accelerated corrosion processes had half-cell potentials less than -200 mV CSE. We

observed that two beams (FB-C6 and FB-C7) in the FB-C series beams had half-cell potentials less than -350 mV CSE and five beams (SB-C3 to SB-C7) in the SB-C series beams had half-cell potentials less than -350 mV CSE.

3.2. Cracking and Failure Pattern. Figure 10 shows the cracking patterns at the midspan of the flexural failure type beams. In the case of the FB-C0 beam, the initial cracking took place near the midspan of the beam at a load of 10.4 kN, and the corresponding deflection at the midspan was 0.49 mm. The cracks spread from the midspan to the support with a crack spacing of 50~150 mm. The reinforcing bar started to yield at a load of 65.0 kN and the corresponding deflection was 7.0 mm. After the yield load, the width of the cracks increased significantly until the specimen failed. Final failure of the beam occurred due to crushing of the concrete at the top of the beam, with cracks reaching the upper parts of the beams.

Overall, the flexural behavior of the FB-C0 specimen was similar to the typical behavior of underreinforced beams. The FB-C1 to FB-C7 beams, which were each corroded to varying degrees, exhibited similar failure patterns to the FB-C0 beam. However, we observed that the amount of rust increased as we increased the duration of the accelerated corrosion, which is quantitatively represented by the half-cell potential. The deflection corresponding to the ultimate load varied significantly according to the duration of accelerated corrosion, between 80 and 110 mm.

Figure 11 shows the cracking patterns at midspan for the shear failure type beams. In the case of the SB-C0 beam, the crack started near the midspan of the beam at a load of 22.0 kN, and the corresponding deflection of the beam at the midspan was 0.52 mm. A diagonal crack was observed in the right part of the beam at a load of 90.2 kN (deflection:

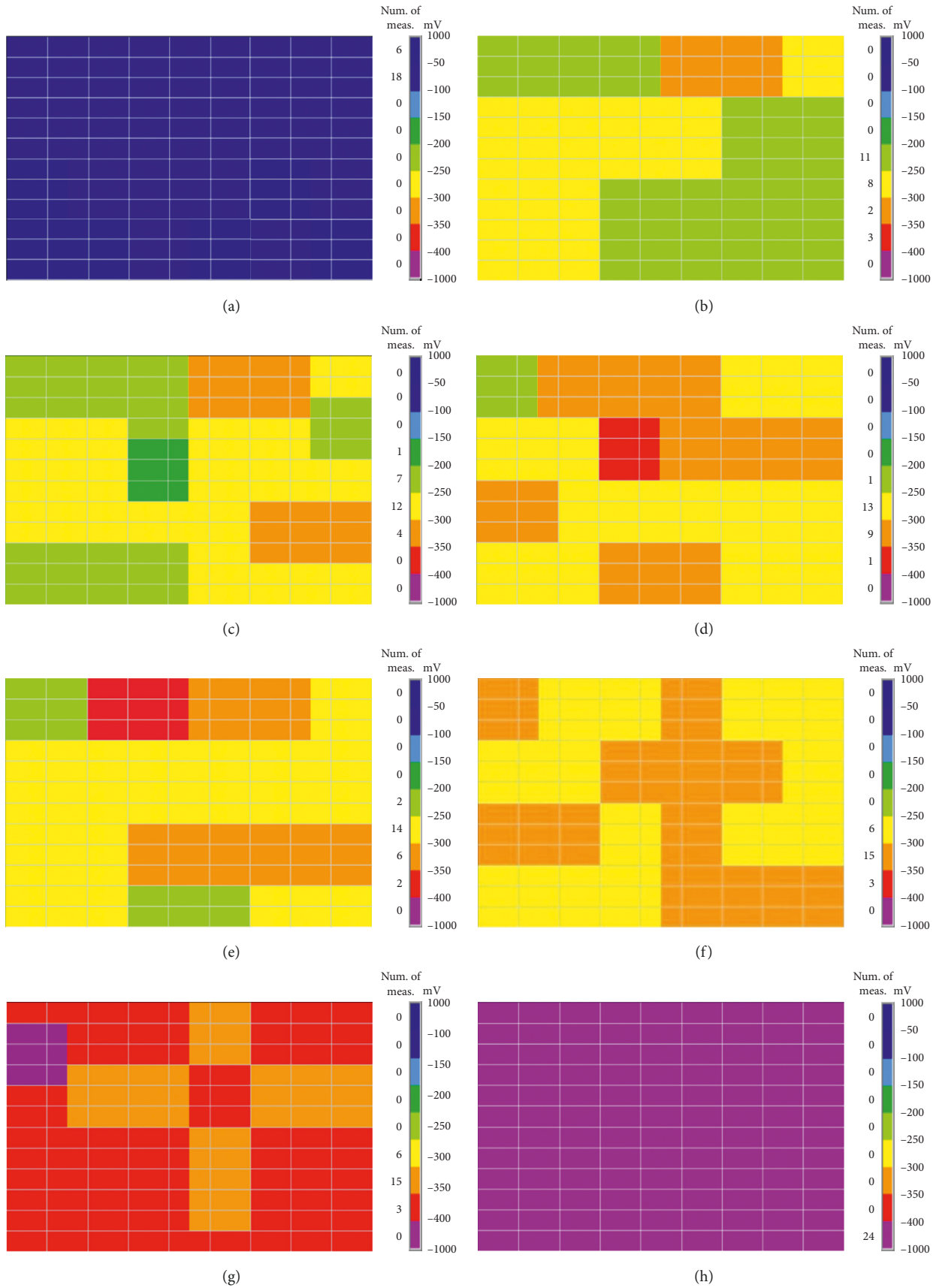


FIGURE 8: Potential map of beams controlled by flexure: (a) FB-C0, (b) FB-C1, (c) FB-C2, (d), FB-C3, (e) FB-C4, (f) FB-C5, (g) FB-C6, and (h) FB-C7.

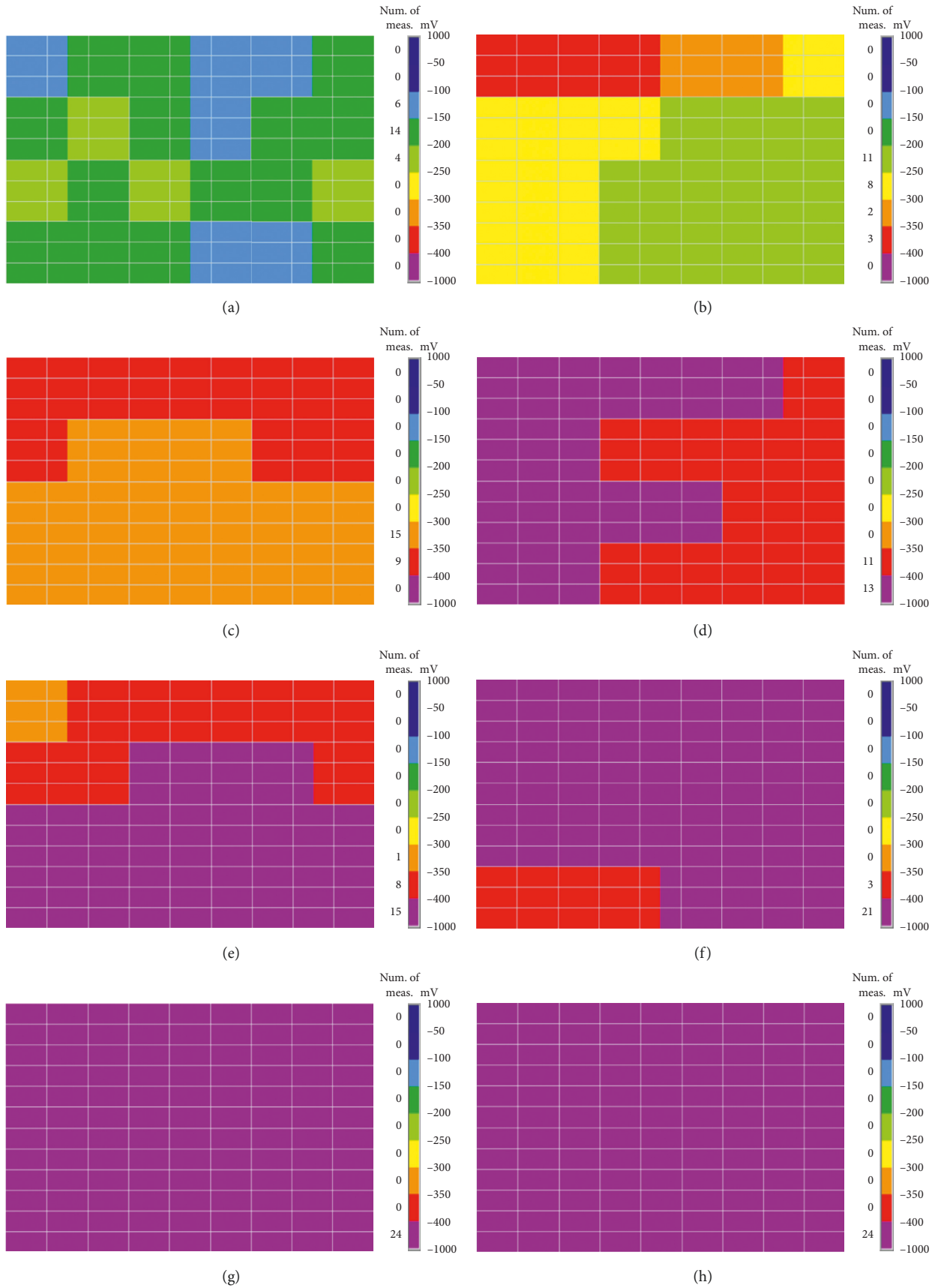


FIGURE 9: Potential map of beams controlled by shear: (a) SB-C0, (b) SB-C1, (c) SB-C2, (d) SB-C3, (e) SB-C4, (f) SB-C5, (g) SB-C6, and (h) SB-C7.



FIGURE 10: Cracking and failure patterns of flexural failure type beams: (a) FB-C0 beam, (b) FB-C4 beam, and (c) FB-C7 beam.

2.67 mm). The number and width of cracks increased until the maximum load (182 kN) was reached. After the ultimate load, we observed a fast load drop as a diagonal crack reached the top surface. Overall, the behavior of the SB-C0 specimen was relatively similar to the typical brittle behavior of shear failure beams. The SB-C1 to SB-C7 beams, which were each corroded to different extents, exhibited similar cracking strengths and corresponding deflections and similar failure patterns to the SB-C0 beam. However, we also observed that the amount of rust increased as we increased the duration of accelerated corrosion. The ultimate load and

maximum deflection varied significantly with the duration of the accelerated corrosion.

3.3. Load and Deflection. Figure 12 shows the load and deflection curves of the flexural failure type (FB-C series) beams and the shear failure type (SB-C series) beams, respectively. The FB-C series beams exhibited similar behavior prior to their ultimate state. The load and deflection values of each beam at the initial cracking of the concrete, the yielding of tensile reinforcement, and the ultimate load, ductility



(a)



(b)



(c)

FIGURE 11: Cracking and failure patterns of shear failure type beams: (a) SB-C0 beam, (b) SB-C4 beam, and (c) SB-C7 beam.

ratio, dissipated energy, and performance degradation factor are summarized in Table 2. The performance degradation factor (ϕ) was defined by the following equation:

$$\phi = \frac{E_r}{E_t}, \quad (1)$$

where E_t and E_r are the absorbable energy capacity before and after corrosion of the reinforcing bar, respectively.

All flexural failure type beams (FB-C series) exhibited similar cracking loads and deflections, ranging from 10.3 to 13.1 kN and 0.44 to 0.59 mm, respectively, and similar yield

loads and deflections, ranging from 62.6 to 63.2 kN and 6.21 to 6.48 mm, respectively. At the ultimate state, the difference between the ultimate loads was less than 11.7%. The maximum difference in displacement corresponding to the ultimate loads and degradation factor was 34.1% and 30.1%, respectively.

According to these test results, we concluded that the corrosion of reinforcing bars has a negative influence on the deformation corresponding to the ultimate load and energy dissipation capacity, which can be expressed as the degradation factor. The effect of corrosion on the flexural behavior of the beams prior to the ultimate state and ultimate load was

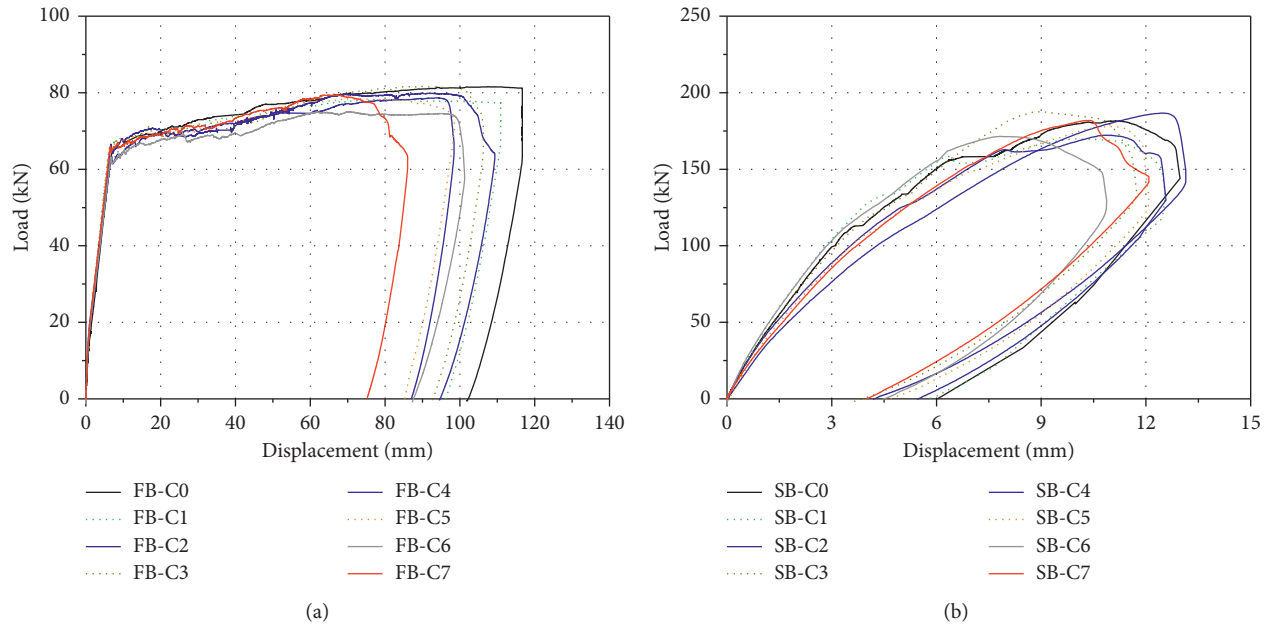


FIGURE 12: Load and deflection curves at the midspan of beams: (a) flexural failure type beams and (b) shear failure type beam.

TABLE 2: Test results for each specimen.

Beam	First cracking		Reinforcement yielding		Ultimate		Dissipation energy (kN-mm)	ϕ^* (%)
	Load (kN)	Deflection (mm)	Load (kN)	Deflection (mm)	Load (kN)	Deflection (mm)		
FB-C0	10.3	0.49	65.0	7.00	81.6	116.7	8,298	100.0
FB-C1	12.5	0.50	66.5	6.68	78.9	100.9	7,521	90.6
FB-C2	13.1	0.59	66.6	6.54	77.4	110.9	7,639	92.1
FB-C3	12.7	0.55	62.6	6.48	80.7	101.4	7,404	89.2
FB-C4	10.7	0.46	63.4	6.90	78.4	95.6	6,683	80.5
FB-C5	10.8	0.44	65.0	6.21	72.0	98.7	6,659	80.3
FB-C6	10.6	0.44	63.2	6.75	74.3	97.4	6,651	80.2
FB-C7	12.1	0.50	66.0	6.55	77.2	76.9	5,797	69.9
SB-C0	22.0	0.52	158.3	7.04	181.9	11.3	1,301	100.0
SB-C1	21.9	0.48	89.6	2.25	169.8	10.0	1,267	97.3
SB-C2	18.0	0.39	93.9	3.24	172.3	11.0	1,178	90.5
SB-C3	18.3	0.45	74.0	2.14	187.7	9.0	1,121	86.2
SB-C4	16.0	0.50	79.6	3.16	186.7	12.5	1,090	83.7
SB-C5	18.1	0.50	106.7	3.82	178.1	11.1	1,101	84.6
SB-C6	23.7	0.49	98.3	2.79	171.4	7.8	1,056	81.1
SB-C7	19.3	0.51	82.5	2.88	181.9	10.3	995	76.4

*Performance degradation factor.

less significant. The energy dissipation of the FB-C series beams decreased as we increased the half-cell potential. The decrease in energy dissipation of FB-C7, which exhibited a maximum absolute half-cell potential, was up to 30.1% compared to that of the FB-C0 control beam. This was attributed to the decrease in effective area of the reinforcing bar due to corrosion [2, 4, 7, 15, 16].

As expected, all SB-C series beams exhibited brittle failure behavior compared to the FB-C series beams. Furthermore, larger variations in the cracking, yielding, and ultimate state of beams with respect to the reinforcing bar corrosion were observed than in the case of the FB-C series beams. The maximum decrease in the first cracking load,

reinforcement yielding load, and ultimate load was 27.4%, 53.3%, and 10.3%, respectively. Although large decreases in the first cracking load and reinforcement yielding load were observed compared to the FB-C series beams, the effect of reinforcing bar corrosion on the ultimate state was less significant. The energy dissipation of the SB-C series beams also decreased with increasing half-cell potential. The energy dissipation of SB-C7, which also exhibited a maximum absolute half-cell potential, was 23.6% lower than that of the SB-C0 control beam.

Figure 13 shows the relationship between the performance degradation factor and average potential difference. We applied empirical regression models to derive the

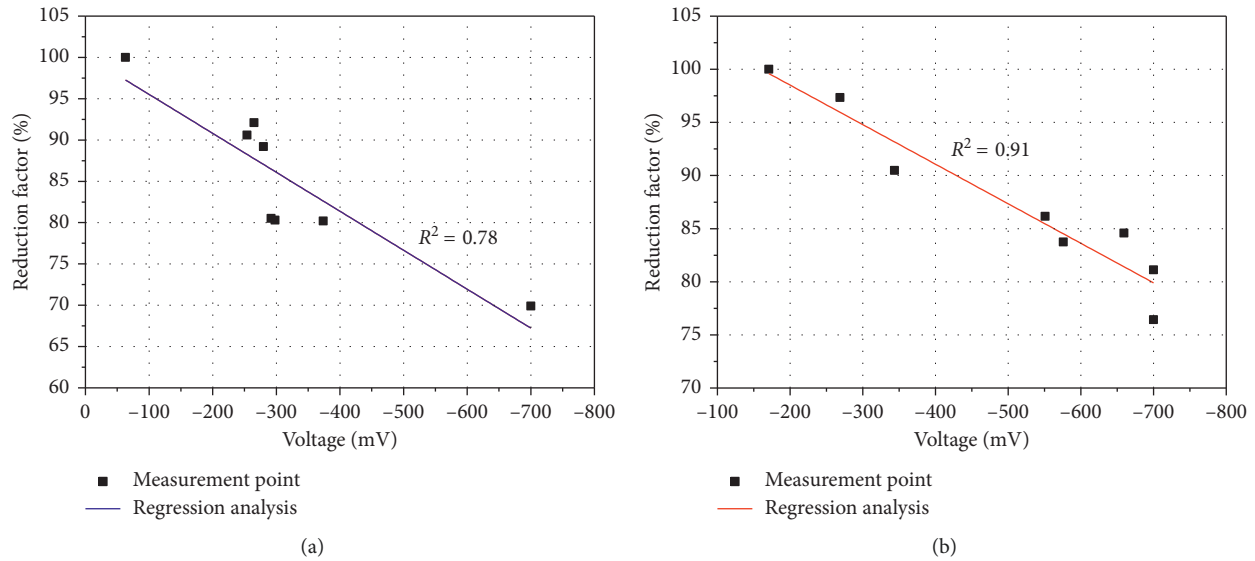


FIGURE 13: Relationship between the performance degradation factor and average potential difference in terms of voltage: (a) flexural failure type beams and (b) shear failure type beam.

quantitative relationship between the performance degradation factor and the average potential difference. As shown in Figure 13, we detected a relatively strong correlation between the performance degradation factor and average potential difference. The coefficients of determination (R^2) of the FB-C series beams and SB-C series beams were 0.78 and 0.91, respectively.

It is well known, on the other hand, that the value of the half-cell potential measurement cannot be used to estimate the structural properties of RC members because the test results of half-cell potential measurements are affected by the degree of humidity in the concrete, oxygen content near the reinforcement, microcracks, etc. [25]. The results shown in Figure 13 indicate that the potential difference measured using the half-cell method can serve as one of the parameters for indicating relative structural degradation, as long as the same environmental conditions are used.

By using relationship between the performance degradation factor and average potential difference in terms of voltage, the energy absorption capacity (the reduction factor in Figure 13), calculated based on strength-deformation capability of corrosion-damaged RC members, can be evaluated. The result of each energy absorption capacity of corrosion-damaged members can be utilized for predicting the seismic capacity of entire RC buildings. For instance, for the corrosion-damaged members, the basic structural performance index (E_O) calculated with respect to the ultimate horizontal strength and ductility for each member can be quantitatively and directly calculated when applying the Japanese standard for seismic evaluation of entire RC buildings.

4. Conclusions

We experimentally investigated the effect of the corrosion of reinforcing bars on the flexural and shear behaviors of RC beams and proposed a relationship between the half-cell potential of corroded reinforcing bars and structural

performance degradation behavior of RC beams. The following conclusions can be drawn from our experimental results:

- (1) The flexural and shear behaviors of the control beams were generally similar to the typical behaviors of underreinforced beams. The shear and flexural beams, corroded to varying degrees among specimens, exhibited similar failure patterns to the control beam. However, we also observed that the amount of rust increased, and the ultimate load and maximum deflection varied significantly, with the duration of accelerated corrosion.
- (2) Based on the test results on the flexural behavior of beams, we concluded that the corrosion of reinforcing bars negatively influences the deformation corresponding to the ultimate load and energy dissipation capacity, which we expressed as the degradation factor. The effect of corrosion on reinforcing bars prior to the ultimate state and ultimate load was less significant. The energy dissipation of the flexural beams decreased with increasing half-cell potential. The energy dissipation of the specimen that exhibited the maximum absolute half-cell potential decreased by up to 30.1% compared to that of the control beam.
- (3) All of the beams controlled by shear exhibited brittle failure behavior compared to those controlled by flexure, and larger variations in the cracking, yielding, and ultimate state of the former beams according to the reinforcing bar corrosion were observed than in the case of the flexural beams. The energy dissipation of the shear beams also decreased with increasing half-cell potential, just as in the case of the flexural beams. The decrease in energy dissipation of the specimen with the maximum absolute half-cell potential was 23.6% lower than that of the control beam.

- (4) We detected a relatively strong correlation between the performance degradation factor and average potential difference, and the coefficients of determination (R^2) of the flexural beams and shear beams were 0.78 and 0.91, respectively. The potential difference measured using the half-cell method can be used as an indicator of relative structural degradation if the environmental conditions are held constant. On the basis of relationship between the performance degradation factor and average potential difference, the energy absorption capacity, calculated based on strength-deformation capability of corrosion-damaged RC members, can be evaluated. The result of each energy absorption capacity of corrosion-damaged members can be utilized for predicting the seismic capacity of entire RC buildings.
- (5) The main objective of this research is to propose a practical methodology for evaluating the seismic performance of RC buildings with corrosion-damaged members. A structural performance degradation factor derived from the energy absorption capacity, calculated based on strength-deformation capability of corroded members, is used to evaluate their seismic performance, quantitatively and directly. As a first step toward achieving the main research objective, in this study, the effects of reinforcing bar corrosion on the behavior of RC beams and the structural performance degradation factor were investigated experimentally. The beam is not the lateral resisting member like the column. Therefore, the results investigated in this research could not be directly used for evaluating the seismic capacity of entire RC building. In order to propose a robust practical methodology for evaluating the seismic performance of RC buildings with corrosion-damaged members, the seismic performance degradation factor of lateral load resisting systems such as columns should be experimentally derived for further research, together with analytical investigations such as finite element analysis.

Data Availability

All datasets generated during this study are available from the corresponding author on reasonable request.

Conflicts of Interest

The authors declare that they have no conflicts of interest.

Acknowledgments

This research was supported by the National Research Foundation of Korea (2017R1A2B4008983 and 2015R1A5A1037548), funded by the Ministry of Education and the Ministry of Science and Information and Communications Technology, and by the Korea Agency for Infrastructure Technology Advancement grant (19CTAP-C153033-01-000000) funded by the Ministry of Land, Infrastructure, and Transport.

References

- [1] C. M. Hansson, "Comments on electrochemical measurements of the rate of corrosion of steel in concrete," *Cement and Concrete Research*, vol. 14, no. 4, pp. 574–584, 1984.
- [2] H. S. Lee, F. Tomosawa, and T. Noguchi, "Effects of rebar corrosion on the structural performance of singly reinforced beams," *Durability of Building Materials and Components*, vol. 7, no. 1, pp. 571–580, 1996.
- [3] D. M. Frangopol, K.-Y. Lin, and A. C. Estes, "Reliability of reinforced concrete girders under corrosion attack," *Journal of Structural Engineering*, vol. 123, no. 3, pp. 286–297, 1997.
- [4] A. Shamsad, "Reinforcement corrosion in concrete structures, its monitoring and service life prediction—a review," *Journal of Cement and Concrete Composites*, vol. 25, no. 4-5, pp. 459–471, 2003.
- [5] H.-W. Song, H.-B. Shim, A. Petcherdchoo, and S.-K. Park, "Service life prediction of repaired concrete structures under chloride environment using finite difference method," *Cement and Concrete Composites*, vol. 31, no. 2, pp. 120–127, 2009.
- [6] H.-S. Lee and Y.-S. Cho, "Evaluation of the mechanical properties of steel reinforcement embedded in concrete specimen as a function of the degree of reinforcement corrosion," *International Journal of Fracture*, vol. 157, no. 1-2, pp. 81–88, 2009.
- [7] M. Dogan, "Corrosion failure in concrete reinforcement to damage during seismic," *Engineering Failure Analysis*, vol. 56, pp. 275–287, 2015.
- [8] Z. Yu, Y. Chen, P. Liu, and W. Wang, "Accelerated simulation of chloride ingress into concrete under drying-wetting alternation condition chloride environment," *Construction and Building Materials*, vol. 93, pp. 205–213, 2015.
- [9] A. Kaveh, S. Allan, P. Alessandro, and C. Don, "Influence of chloride corrosion on the effective mechanical properties of steel reinforcement," *Structure and Infrastructure Engineering*, vol. 15, no. 8, pp. 1036–1048, 2019.
- [10] Namita, *Effects of Corrosion in Reinforcement: Signs & Preventive Measures Structural Engineering*, CivilDigital, CivilDigital.com, 2018.
- [11] Federal Emergency Management Agency, *FEMA 310 Handbook for Seismic Evaluation of Buildings—A Prestandard*, Federal Emergency Management Agency, Washington, DC, USA, 1998.
- [12] Federal Emergency Management Agency, *FEMA 356 Prestandard and Commentary for Seismic Rehabilitation of Buildings*, Federal Emergency Management Agency, Washington, DC, USA, 2000.
- [13] Japan Building Disaster Prevention Association, *English Version: Standard for Seismic Evaluation of Existing Reinforced Concrete Buildings*, Japan Building Disaster Prevention Association, Tokyo, Japan, 2005.
- [14] Y. Li, S. P. Yin, and W. j. Chen, "Seismic behavior of corrosion-damaged RC columns strengthened with TRC under a chloride environment," *Construction and Building Materials*, vol. 201, pp. 736–745, 2019.
- [15] J. G. Cabrera, "Deterioration of concrete due to reinforcement steel corrosion," *Cement and Concrete Composites*, vol. 18, no. 1, pp. 47–59, 1996.
- [16] R. Capozucca, "Damage to reinforced concrete due to reinforcement corrosion," *Construction and Building Materials*, vol. 9, no. 5, pp. 295–303, 1995.
- [17] A. Wei, Y. Wang, and M. Y. J. Tan, "Monitoring corrosion of reinforced concrete beams in a chloride containing

- environment under different loading levels,” *Structural Monitoring and Maintenance*, vol. 2, no. 3, pp. 253–267, 2015.
- [18] B. Pradhan and B. Bhattacharjee, “Half-cell potential as an indicator of chloride-induced rebar corrosion initiation in RC,” *Journal of Materials in Civil Engineering*, vol. 21, no. 10, pp. 543–552, 2009.
- [19] B. Assouli, G. Ballivy, and P. Rivard, “Influence of environmental parameters on application of standard ASTM C876-91: half cell potential measurements,” *Corrosion Engineering, Science and Technology*, vol. 43, no. 1, pp. 93–96, 2008.
- [20] ASTM C39/C39M-15, *Standard Test Method for Compressive Strength of Cylindrical Concrete Specimens*, ASTM International, West Conshohocken, PA, USA, 2015.
- [21] ASTM E8/E8M-15, *Standard Test Methods for Tension Testing of Metallic Materials*, ASTM International, West Conshohocken, PA, USA, 2015.
- [22] ACI Committee 318, *Building Code Requirements for Structural Concrete and Commentary (ACI 318-11) and Commentary*, American Concrete Institute, Farmington Hills, MI, USA, 2011.
- [23] Proceq, *CANIN+ Operating Instruction for Corrosion Analyzing Instrument*, Proceq, Schwerzenbach, Switzerland, 2009.
- [24] ASTM C876-09, *Standard test method for corrosion potentials of uncoated reinforcing steel in concrete*, ASTM International, West Conshohocken, PA, USA, 2009.
- [25] P. K. Mehta and P. J. M. Monteiro, *Concrete Microstructure, Properties, and Materials*, McGraw-Hill Companies, New York, NY, USA, 3rd edition, 1994.

Research Article

Experimental Study on Flexural Behavior of Prestressed Concrete Beams Reinforced by CFRP under Chloride Environment

Yunyan Liu  and Yingfang Fan 

College of Transportation Engineering, Dalian Maritime University, Dalian 116026, China

Correspondence should be addressed to Yingfang Fan; fanyf72@aliyun.com

Received 5 May 2019; Revised 15 July 2019; Accepted 24 July 2019; Published 29 August 2019

Guest Editor: Charis Apostolopoulos

Copyright © 2019 Yunyan Liu and Yingfang Fan. This is an open access article distributed under the Creative Commons Attribution License, which permits unrestricted use, distribution, and reproduction in any medium, provided the original work is properly cited.

In order to study the effects of initial damages, CFRP reinforcement, and chloride corrosion on the flexural behavior of prestressed concrete beams, ten prestressed concrete beams were designed and manufactured, which were preloaded with 0%, 40%, and 60% of the ultimate load to crack. Then, part of the beams were reinforced by CFRP and immersed in chloride condition for 120 days. After that, the four-point bending tests were performed. Then, the sectional strain, deformation, flexural stiffness, flexural capacity, ductility, and the cracking characteristics were researched. The test results demonstrate that the sectional strain of PC beams still follows the plane cross section assumption after a pure bending deformation considering of the initial cracks, chloride corrosion, and CFRP reinforcement. The initial damage accelerates the chloride corrosion, resulting in the loss of initial stiffness, ductility, and cracking load, and the reduction in flexural capacity is less than 10%, and the failure modes of these beams are prone to change from concrete crushing to shear failure. In the cracking stage, the reinforcement of CFRP inhibits the bending deformation, leading to the reduction in stiffness degradation rates and the increase of cracking load, and the ultimate load increases by 12.8%~18.7%. The reinforcement of CFRP constrains the development of cracks, increases the cracks numbers by 50%~130%, decreases the cracking rates of beam bottoms by 52.5%, and reduces the average crack widths by 65.8% at 195 kN. It can be seen that the reinforcing effect of CFRP is more significant compared with the weakening effect of short-term chloride corrosion and initial damage on the flexural behavior.

1. Introduction

Prestressed concrete structure has been widely promoted because of its high strength, excellent performance, and structure diversification. Also, these structures are more prone to be affected by the environment due to its composition and mechanical characteristics, such as high temperature, freezing, acid rain, and deicing salt corrosion. Chloride corrosion is the major influencing factor. Nowadays, the durability problems of these structures occur frequently, which needs to be replaced, repaired, and strengthened. The Sorell Causeway Bridge [1] in Australia was demolished, and the “S.Stefano” viaduct [2] in Italy collapsed suddenly, following the corrosion of prestressing tendons in the beams, due to the long-term exposure to an aggressive marine environment. Prestressing steel subjected

to high permanent stress has generally poor resistance to corrosion [3] compared to the ordinary steel bar. The loss of cross area and mechanical behavior of steel strands and the degradation of bond behavior between concrete and steel strands [4–6] will have a significant influence on the safety of prestressed concrete structures. Li and Yuan [7] believed that the effect of slight corrosion rates (less than 2.87%) is not significant to the flexural capacity, but will lead to the remarkable degradation of ultimate deflection for the beams with wire rupture failure. The tests of Rinaldi et al. [8] and Zhang et al. [9] show that the ultimate capacity of PC beams decreases with the increase of corrosion degree and turns the failure mode from ductile to brittle. An analysis model is proposed by Wang et al. [5] to predict the failure and flexural strength of PC beams under chloride corrosion condition. A numerical model is proposed by Coronelli to simulate the

effects of wire breaking in PC beams suffering from corrosion condition. Also, the local fracture of corroded steel strand in different locations in PC beam is simulated by Yang et al. [10] through a rapid corrosion test, and the test results show that the closer the corrosion fracture location is to the midspan, the more obvious the reduction in flexural stiffness and capacity is.

In practical engineering, the bridge is not only affected by the environment but also by fatigue loads. Some factors like low design standards overloaded for a long time or the vehicles' impact may lead to the damage on concrete bridges. The steels in the cracking area are always in a high stress state, even if the beam was unloaded completely, and there will be the residual cracks and deflection. The tests of Vicente et al. [11] and Recupero and Spinella [12] indicate that cracking and internal damage caused by cyclic loading will affect the bond behavior between steel strand and concrete, reduce the stiffness and natural frequency, and increase the vertical deflection and crack widths. The tests of Dasar et al. [13] show that the bending cracks of reinforced concrete beams exposed to the marine environment for a long time accelerate the corrosion rate of the steel, reduce the effective prestress and flexural capacity, and lead to the earlier failure.

Carbon fiber composite (CFRP) has the advantages of lightweight, high strength, corrosion resistance, and fatigue resistance. Therefore, CFRP is widely used to strength and repair damaged bridges, while greatly reducing installation time and cost [14]. At present, the reinforcement of corroded prestressed concrete structures by CFRP has attracted much attention. Adham and Khaled [15] hold that the flexural capacity of corroded prestressed concrete beams can be restored after CFRP repaired, but the reduction in ductility is irreversible. Shaw and Andrawes [16] repaired a corroded PC beam by mortar, GFRP, and CFRP, the results show that the mortar repair is alone insufficient in regaining the concrete initial strength and stiffness, and CFRP laminates are superior to GFRP laminates in regaining the stiffness and flexural capacity. The reinforcement of CFRP to prestressed concrete beams with damages has also been concerned by many scholars [17–20]. It is thought that the bearing capacity and stiffness of beams with damages due to overload and vehicle impact can be effectively restored after the CFRP reinforcement. At present, there are few research studies on the CFRP reinforcement of prestressed concrete beams with bending cracks and exposed to chloride environments, and such damage condition is more close to the actual project and more worthy to be studied.

The four-point bending tests were applied on all test beams. And the effects of CFRP reinforcement, initial bending cracks, and chloride corrosion on the distribution of cross-sectional strain, structural deformation, flexural stiffness, flexural capacity, crack propagation, and failure modes were researched.

2. Experimental Programs

2.1. Concrete Specimens. Ten pretensioned prestressed concrete beams were designed and manufactured. Commercial

concrete was adopted, and the concrete strength grade was C40. All beams have the same dimension of $150 \times 250 \times 2200$ mm. The beams were reinforced by four 14 mm deformed bars at top and bottom and seven 6 mm stirrups with 100 mm at beam end. The beams were pretensioned with two 12.7 mm strands, and the initial prestress of the strand is 558 MPa, which is about 0.3 times of the yield strength. The details are shown in Figure 1.

The average yield strength of the prestressed strand, the deformed bars, and the 6 mm plain bars was 1860 MPa, 335 MPa, and 235 MPa, respectively, and the elastic modulus was 195 GPa, 200 GPa, and 210 GPa, respectively. The average compressive strength of 28-day concrete for all the beams was 49.4 MPa.

2.2. Test Condition. In order to simulate the influence of initial cracks, CFRP reinforcement, and chloride corrosion on the flexural behavior of PC beams, ten beams were applied different loading conditions, respectively. The test conditions of all beams are listed in Table 1.

In order to simulate the influence of initial damage on the durability of PC beams, six beams were preloaded to crack with 40% and 60% of the ultimate load. The distributions and parameters of initial cracks are shown in Figure 2 and Table 2.

Then, the beams were reinforced by CFRP, and U-shaped hoops were set at both ends, such as beam C0-1, C40-1, C60-1, C0-2, C40-2, and C60-2. The reinforcing scheme of CFRP is shown in Figure 3, and the mechanical properties of CFRP are shown in Table 3.

After preloading and CFRP reinforcement, the beams were immersed in a deicing salt solution for 120 days. The components of the solution are CaCl_2 and MgCl_2 , and the concentration is 5%. It can be seen in Figure 4.

2.3. Loading Process. The actions of multifactor, such as initial damage, CFRP reinforcement, and chloride corrosion, change the bond performance between steel bars and concrete and affect the propagation of bending cracks. The design codes are very difficult to predict the flexural behavior and crack widths of these PC beams. The four-point bending tests were employed to study the effects of multifactor on the flexural behavior in the current study. Each beam was simply supported and had a pure bending span of 600 mm and two shear spans of 600 mm. Figure 5 shows the details of loading setup.

The loading process was divided into two stages. The first stage was controlled by load until reaching 85% of the ultimate load of the control beam. The load was applied step by step at a rate of 5 kN per step until crack load, then the rate was 10 kN per step. The second stage was controlled by deflection, and the loading increment was 0.6 mm per step. The loading test was stopped when the carrying capacity dropped to 75% of the ultimate load.

The vertical deflections at the midspan were measured by a displacement sensor. Electrical resistance strain gauges were pasted on the midspan section to measure concrete strains. Arrangement of the gauges is shown in Figure 5. One

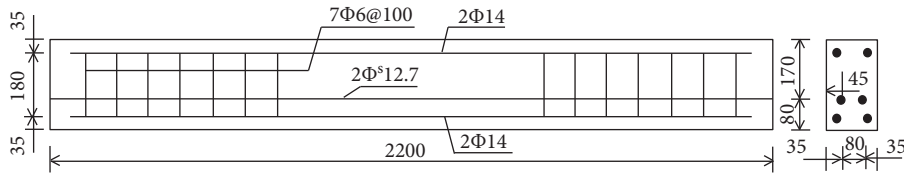


FIGURE 1: Beam details (unit: mm).

TABLE 1: Test conditions.

Beam	Preloading (kN)	Reinforcement	Environment condition
A1	0	—	—
C0-3	0	—	Chloride corrosion for 120 d
C40-3	85	—	
C60-3	125	—	
C0-1	0	CFRP reinforcement	—
C40-1	85		
C60-1	125		
C0-2	0	CFRP reinforcement	Chloride corrosion for 120 d
C40-2	85		
C60-2	125		

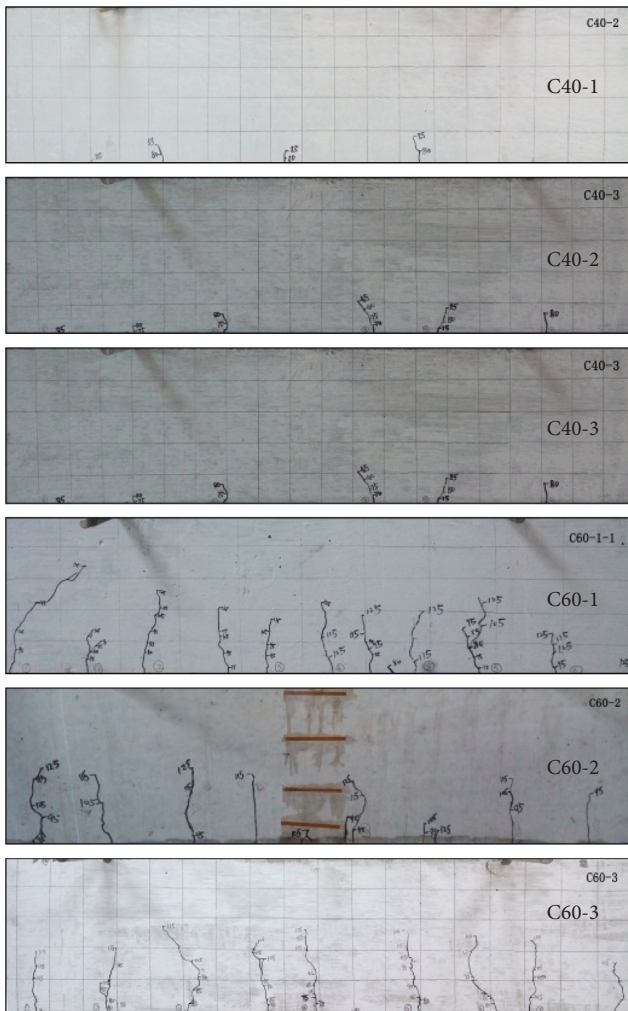


FIGURE 2: Initial cracks on the PC beams after preloading.

side of the beam was painted white and was marked with 5×5 cm grids to facilitate the detection of cracks.

3. Test Results and Discussion

3.1. Distribution of Cross-Sectional Strain. The strain distribution curves of PC beams are shown in Figure 6. In the approximately elastic stage, the strains of concrete at different heights are small and vary linearly. After cracking, the strains increase rapidly. And the section in the midspan, perpendicular to the beam longitudinal axis, is still plane after a pure bending deformation. It is found that the sectional strain at the midspan of the test beams still follows the plane section assumption after preloading, chloride corrosion, and CFRP reinforcement.

According to the strain distributions of beams C0-3, C40-3, C60-3, C0-2, C40-2, and C60-2, it can be seen that, after the immersion in chlorine salt for 120 d, the steel bars were corroded and expanded, resulting in microcracks in the surrounding concrete. During the loading process, the corrosion microcracks developed rapidly until the strain gauge failed. And the corrosion microcracks in the beam with the initial damage cracked earlier under the loading process. At the same time, CFRP pasted on the bottom has little effect on chloride corrosion.

It can be seen from Figure 6 that the ultimate compressive strain of control beam A1 and CFRP reinforced beams C0-1, C40-1, and C60-1, which are under natural conditions, is about 0.002. The ultimate compressive strain of CFRP reinforced beams C0-2, C40-2, and C60-2 in chloride condition is about 0.002. And the ultimate compressive strain of beams C0-3, C40-3, and C60-3 is about 0.001. It follows that the ultimate strain of concrete decreases with the corrosion of steel in the beam, and the

TABLE 2: Parameters of initial cracks on the midspan.

Beam	Crack number in midspan	Space (mm)	Sum of cracks (mm)	Crack width at bottom	Crack height (mm)
C40-1	4	150	6	0.04	40
C40-2	3	200	4	0.06	45
C40-3	3	170	6	0.06	50
C60-1	8	80	12	0.12	130
C60-2	7	100	11	0.12	125
C60-3	8	80	11	0.15	137

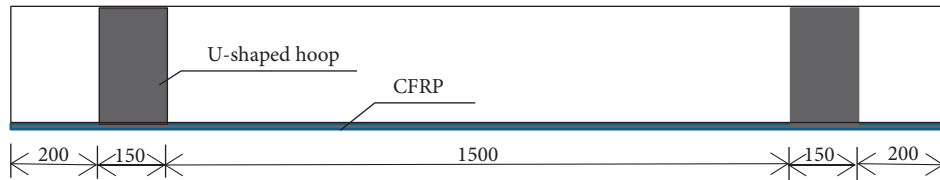


FIGURE 3: Reinforcing scheme of CFRP (unit: mm).

TABLE 3: Mechanical properties of CFRP.

Material	CFRP
Standard value of tensile strength	3493.5 MPa
Elasticity modulus	240 GPa
Elongation	1.7%
Bending strength	737.5 MPa
Shear strength	48.7 MPa
Positive tensile bond strength	3.6 MPa



FIGURE 4: Deicing salt corrosion.

reinforcement of CFRP decreases the effect of corrosion on the ultimate strain. Also, the relationship between the reduction of strain and corrosion and CFRP reinforcement remains to be studied.

With the increase of load grades, the neutral axis moved up from the middle of the beam. After cracking, the movement increases and the height of the compression zone decreases gradually. The compressive concrete depths of each PC beam under the ultimate load are shown in Figure 7. Under natural condition, the compressive concrete depth of the CFRP reinforced beam is higher than that of the control beam, and that of each beam decreased compared with that of the control beam under chloride corrosion for 120 d. Also, the compressive concrete depths of beams C0-1, C40-1, C60-1, C0-3, C40-3, and C60-3 decrease with the increase of the initial damage degree, while the law of C0-2, C40-2, and C60-2 is not obvious.

The chloride condition leads to the corrosion of the steel strand. As the corrosion degree increases, the sectional area

of the steel strand decreases. The experiment in the literature [21] indicates that the corroded steel strand is more prone to slip during the bending test, and the slip rate and ultimate slip value increase with the corrosion degree. The bond slip between the steel strand and the concrete has occurred during the preloading process. Therefore, the bond performance between the steel strand and concrete has been weakened after preloaded to crack or corroded by chloride condition. And the tension stress of the steel strand decreased than that in the control beam under same load grade. For the CFRP reinforced beam, the section curvature and the arm of force between steel bars, steel strand, CFRP, and compressive concrete are smaller than those of the control beam under the action of equivalent load. It makes the neutral axis height lower than the control beam and the compressive concrete depth higher than the control beam. Also, the section curvature and the arm of force decrease with the increase of damage and corrosion degree. Due to the limited data and errors, the distribution of cross-sectional strains of PC beams and the variation in the compressive concrete depths under the action of multifactor are still to be studied.

3.2. Flexural Behavior

3.2.1. Load-Deflection Curves. According to the test results, the load-deflection curve of PC beams in the midspan is drawn, as shown in Figure 8. With the increase of load grade, the deflection in the midspan goes through three stages:

- (1) In the approximate elastic stage, the deformation of the PC beam behaves linearly and slowly. However, the initial flexural stiffness of the beams decreases with initial damage, so the deformation rates of these beams in this stage are higher than that of the control beam. After chloride corrosion of 120 d, the stiffness of the beams decreases further and the deformation rates increase further than that of the control beam.
- (2) In the cracking stage, the bottom concrete was loaded to crack and exited the work. CFRP gives play

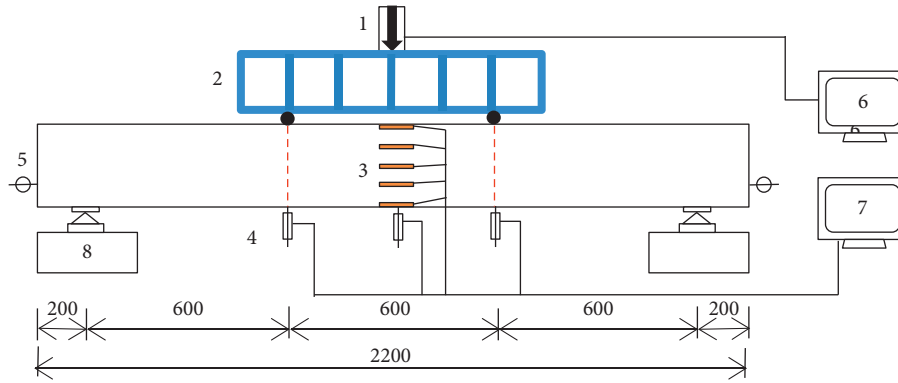


FIGURE 5: Loading test setup (unit: mm). Note: 1, load cell; 2, steel spreader beam; 3, strain gauge; 4, displacement sensor; 5, dial indicator; 6, computer; 7, data acquisition system.

to its high tensile strength, so that the stiffness degradation rate and the deformation rate of CFRP strengthened beam decrease. Under natural conditions, the initial damage has little effect on the flexural stiffness; however, the coupling of chloride corrosion and initial damage reduces the stiffness and accelerates the deformation of the structure in this stage.

- (3) In the failure stage, the test beams yield and maintain a high bearing capacity, and the deflection in the midspan increases rapidly. Arriving at the ultimate bearing capacity, the structure is destroyed.

3.2.2. Flexural Stiffness. In order to analyze the degradation of the flexural stiffness of PC beams under different working conditions, all test beams are considered as homogeneous elastic material models. As the loading time is short and the deflections along the longitudinal sections are different, so the “minimum stiffness principle” is adopted. For the members under flexural load, the deflection is obtained by quadratic integration of curvature:

$$w = \iint \left(\frac{1}{\rho} \right) dx^2 = \iint \frac{M_x}{B_s} dx^2, \quad (1)$$

where w is the deflection, ρ is the radius of curvature, M_x is the bending moment of the beam plane, and B_s is the short-term stiffness. The midspan deflection of the test beam is obtained by solving the above integral. The test beam is simply supported by static loading at two points. The short-term stiffness of the test beam can be obtained by transforming the formula (1), as shown in the following formula:

$$B_s = S \frac{(M_x l_o^2)}{f} = S \frac{P l_o^3}{6f}, \quad (2)$$

where S is the deflection coefficient related to the supporting condition and load form, through calculation, the value of S is $23/216$. P is the load value, f is the deflection in the midspan, and l_o is the calculated span.

According to formula (2), the short-term stiffness of the midspan section is calculated, as shown in Figure 9. Before

cracking, the flexural stiffness of the test beams is basically unchanged, and the initial stiffness of the nondestructive beams C0-1, C0-2, and C0-3 is close to that of the control beam. Under the chloride condition, the initial flexural stiffness of beams C40-3 and C60-3 with initial cracks decreases by about 32.5% and 47.8% compared with the control beam and that of the CFRP reinforced beams C40-2 and C60-2 decreases by about 44.1% and 39.7%, respectively. Under the natural conditions, the initial stiffness of the CFRP reinforced beams C40-1 and C60-1 decreases by about 12.8% and 20.4%, respectively, compared with the control beam. After cracking, the stiffness of the test beams decreases with the increase of load grade. Moreover, the degradation rates of the stiffness of CFRP reinforced beam are lower than that of the control beam.

It can be seen that the change rule of the stiffness of the test beams is consistent with that of the deflection in the midspan. The initial flexural stiffness of the test beams is decreased due to the initial cracks. After the chloride corrosion, the cross-sectional areas of the internal steel bars and strands are decreased, the bond behaviors between the steel strand and concrete are weakened, and the effective prestress is decreased accordingly. Therefore, the flexural stiffness of the test beams decreases with the increase of damage degree under the same load grade. After strengthened by CFRP, CFRP exerts its high tensile performance in the cracking stage and inhibits the structural deformation, and the degradation rates of the flexural stiffness of the CFRP reinforced beams are reduced compared with the control beam. However, CFRP reinforcement has little effect on the initial flexural stiffness.

3.2.3. Cracking Load and Ultimate Load. The effective prestress of the PC beam is calculated according to the cracking load of midspan concrete, as shown in Table 4. It can be seen that the effective prestress and cracking load of control beam A1 are similar to the theoretical value. It can be considered that there is no sustained loss of effective prestress since the end of the curing period. However, after chloride corrosion of 120 d, the effective prestress of beam C0-3 decreased by 20% compared with the theoretical value,

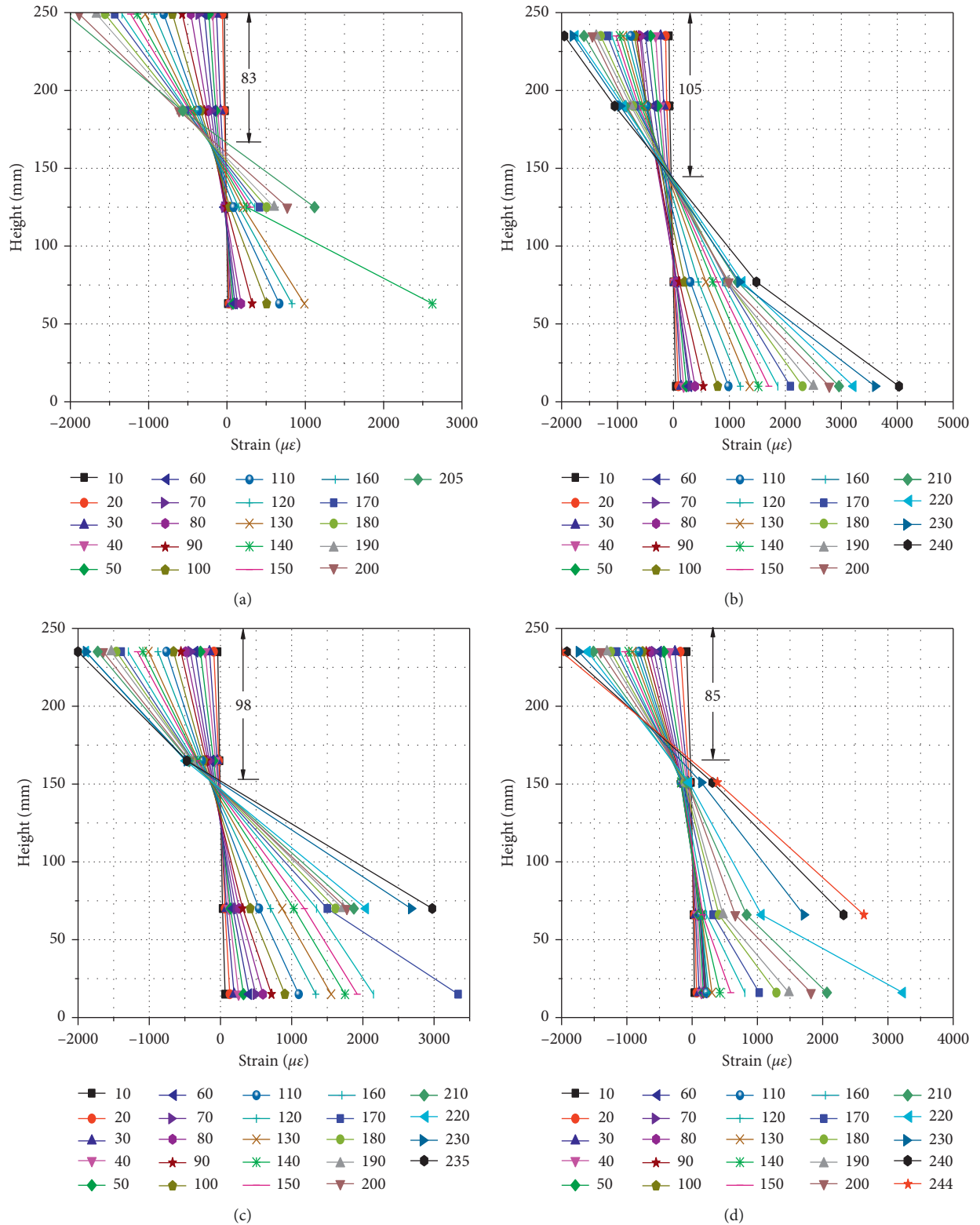
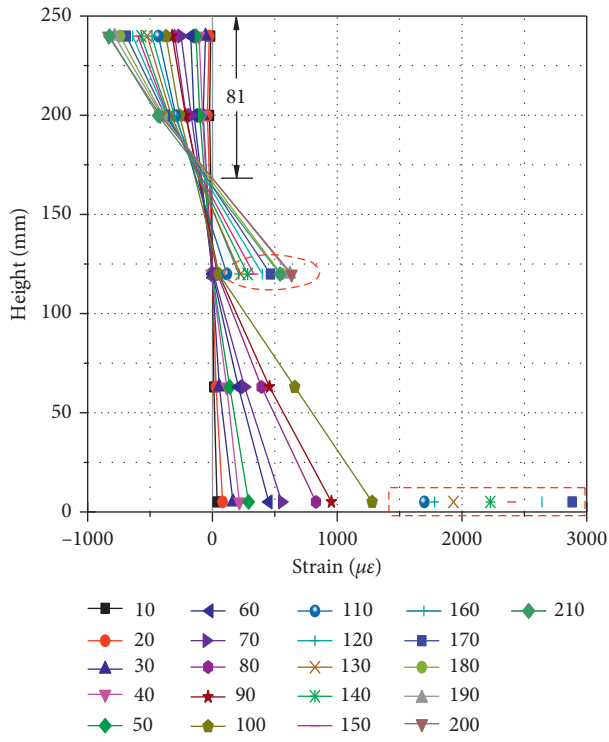
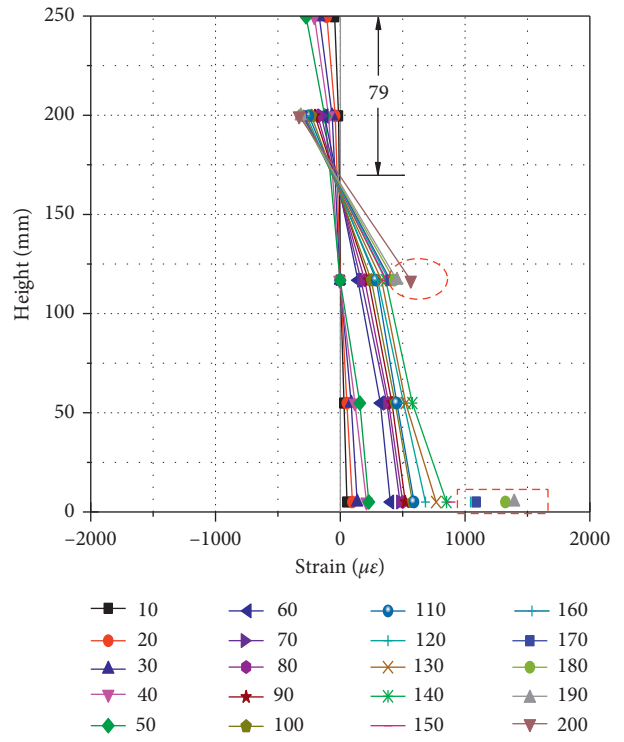


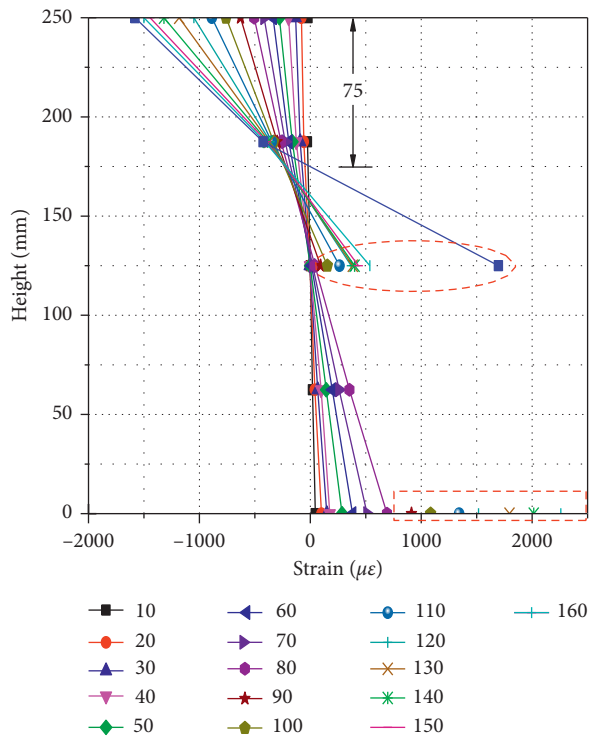
FIGURE 6: Continued.



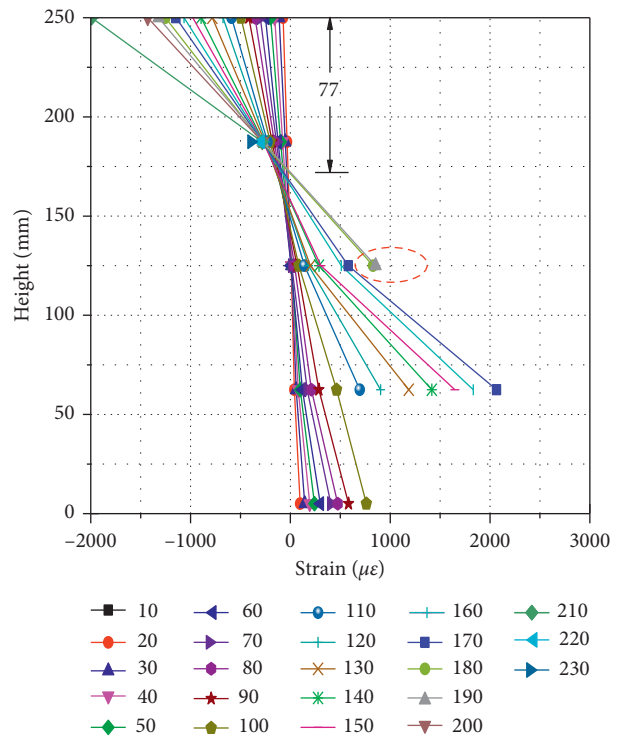
(e)



(f)



(g)



(h)

FIGURE 6: Continued.

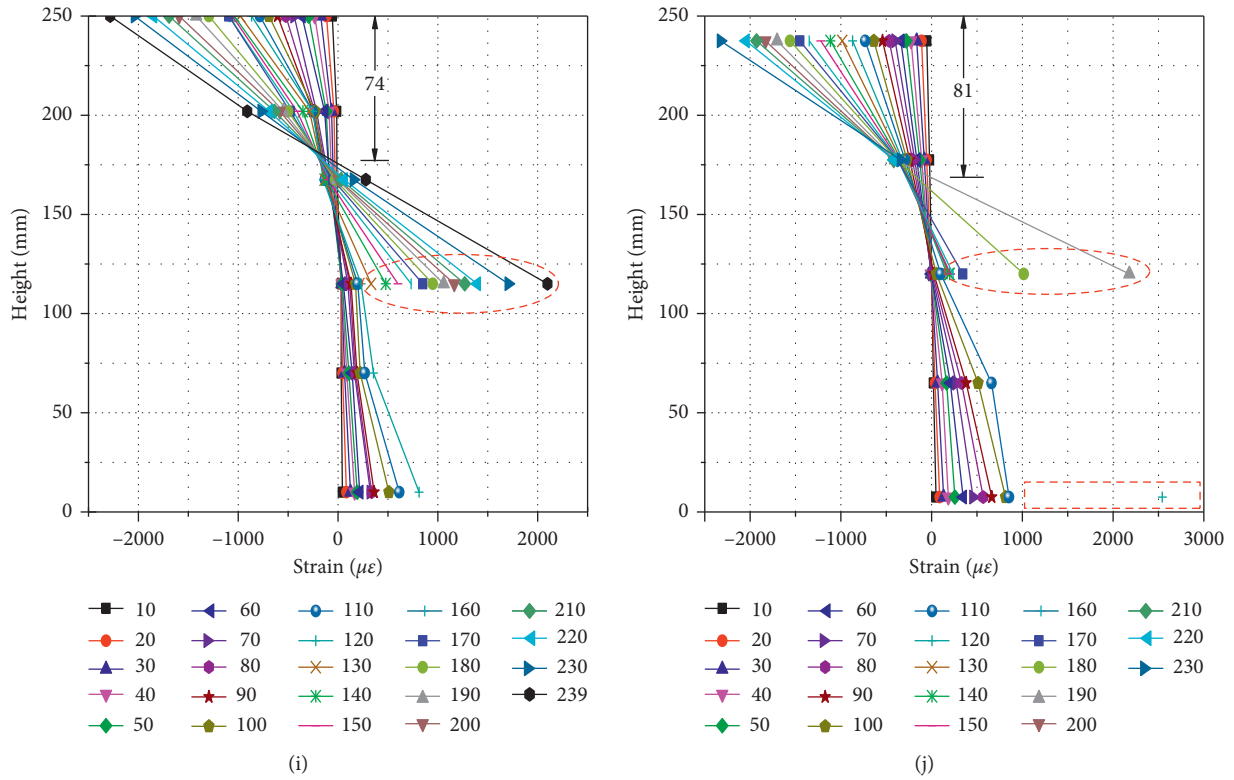


FIGURE 6: Distribution of strain at the midspan. (a) Beam A1, (b) beam C0-1, (c) beam C40-1, (d) beam C60-1, (e) beam C0-3, (f) beam C40-3, (g) beam C60-3, (h) beam B2, (i) beam C40-2, and (j) beam C60-2.

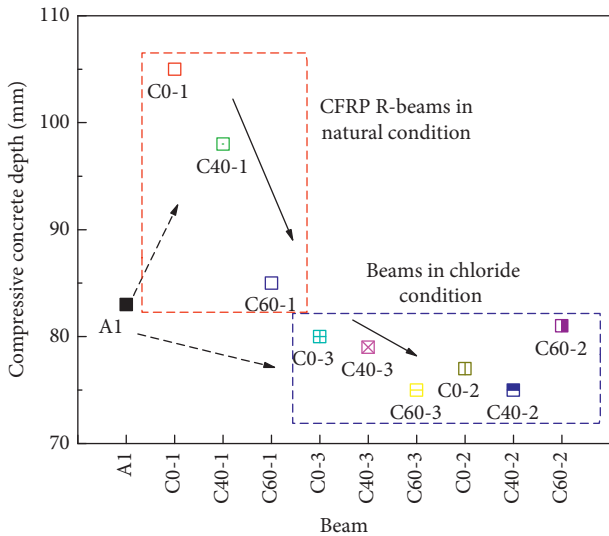


FIGURE 7: Compressive concrete depths at midspan.

and the cracking load decreased by 14%. It shows that the chloride corrosion on the steel strand leads to the degradation of its bond behavior with concrete.

The flexural behaviors of the test beams under the various working conditions are shown in Table 5. The cracking load of the test beams decreased after chloride corrosion and increased after the CFRP reinforcement compared with that of the control beams.

After chloride corrosion of 120 d, the ultimate loads of beams C0-3, C40-3, and C60-3 were reduced by 1.2%, 2.4%, and 9.0%, respectively, compared with the control beam A1. When the initial damage degree is low, the weakening effect of short-term chloride corrosion on the flexural behavior is not obvious, and the weakening effect increases with the initial damage degree. Under natural conditions, the ultimate loads of the CFRP reinforced beams were increased by 15.0%~18.7%. Under chloride condition, the ultimate loads of the CFRP reinforced beams were increased by 12.8%~16.2%. Chloride corrosion reduces the flexural capacity slightly. It is considered that the strengthening effect of CFRP significantly increases the flexural capacity, while the chloride corrosion and initial damage weaken the flexural behavior. When the three factors are coupled, the strengthening effect of CFRP is dominant compared with the weakening effect of chloride corrosion and initial damage.

3.2.4. Ductility. As can be seen from Table 5, CFRP pasted on the beam bottom exerts its high tensile strength to restrain the bending deformation, and ultimate deflection decreases. Therefore, the ductility of the CFRP reinforced beam decreases. Under the chloride condition, the structure with initial damage is more likely to be corroded by chloride, resulting in early failure of the structure. Therefore, the ultimate deflection and ductility are reduced significantly.

CFRP reinforcement can inhibit the structural deformation, but not reduce the chloride corrosion. Therefore,

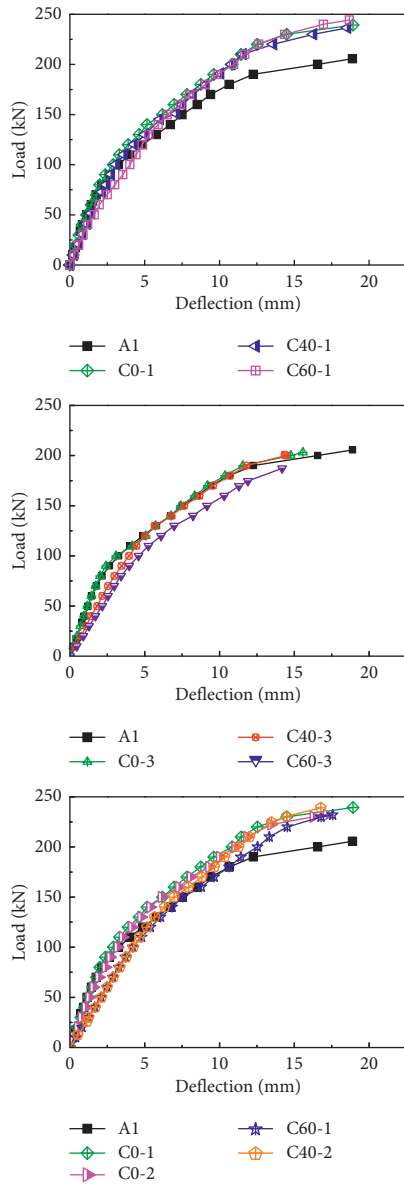


FIGURE 8: Load-deflection curves.

the ultimate deflection and ductility of the CFRP reinforced beams in chloride condition are further reduced than those of the control beams and slightly larger than those of unreinforced beams.

Due to the limited data, the changes in flexural capacity and ductility under the coupling of multiple factors still need to be further studied.

3.3. Cracking and Failure

3.3.1. Crack Patterns. During the loading process, new cracks appeared firstly in the middle span and below the loading points of the test beams. The cracks in the pure bending span developed vertically upward with the increase of load steps. When the neutral axis reached to the maximum height, the cracks are no longer continued. Then the oblique cracks in the shear spans extended rapidly. The

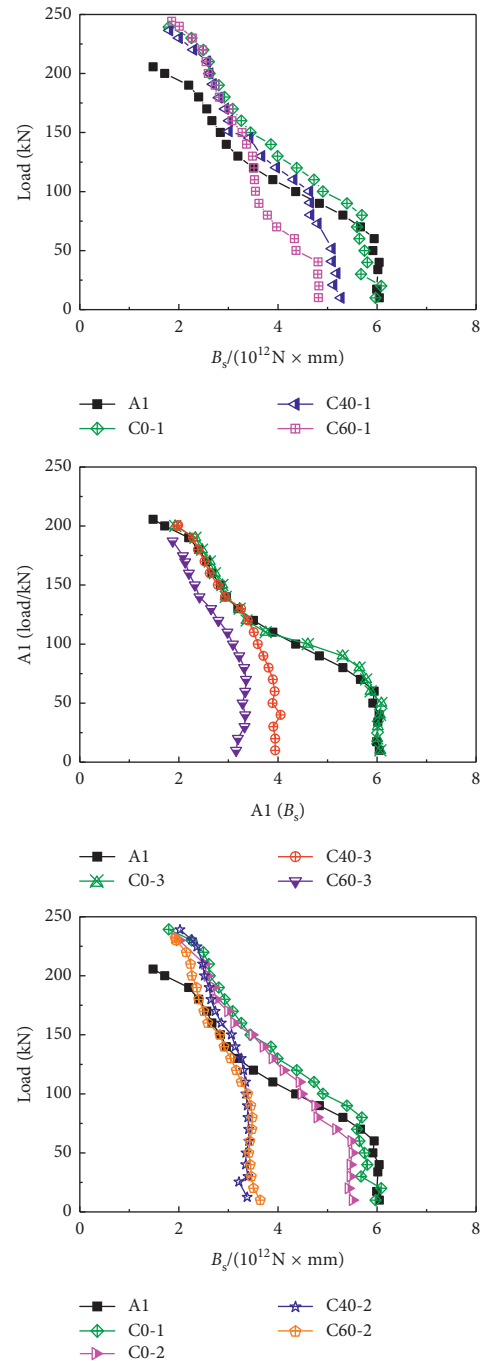


FIGURE 9: Flexural stiffness.

distribution maps of cracks are shown in Figure 10. The parameters of cracks in the pure bending span are shown in Table 6.

During the cracking stage, initial cracks, CFRP reinforcement, and chloride corrosion all have impacts on the cracks of PC beams. According to their locations and causes, the cracks in Figure 10 can be divided into three categories, as is shown in Figure 11:

- (1) Major cracks caused by bending stress appear in the midspan and below the loading points of the test beams. And the distribution of major cracks depends

TABLE 4: The effective prestress.

PC beam	Cracking load (kN)	Effective prestress (kN)
Theoretical value	70.3	1032.9
Control beam A1	70.0	1029.4
Beam C0-3	60.0	827.8

TABLE 5: Summary of the results.

No.	Rebound strength (MPa)	Cracking load (kN)	Ultimate load (kN)	Ultimate deflection (mm)	Yield load (kN)	Yield deflection (mm)	Ductility factor
A1	49.5	70	205.68	19.71	194.58	12.31	1.60
C0-1	49.6	80	239.28	18.92	220.02	12.53	1.51
C40-1	49.6	70/75	236.54	18.55	215.86	12.37	1.50
C60-1	50.5	75/95	244.23	18.69	224.26	13.29	1.41
C0-2	49.8	85	231.94	17.16	221.36	13.13	1.31
C40-2	48.4	70/75	239.02	16.77	228.05	13.27	1.26
C60-2	51.1	75/75	236.98	17.11	219.65	14.68	1.33
C0-3	51.2	60	203.20	15.57	187.29	11.03	1.41
C40-3	50.2	70/50	200.70	14.84	190.98	11.90	1.25
C60-3	51.2	70/60	187.25	14.18	174.70	11.74	1.21

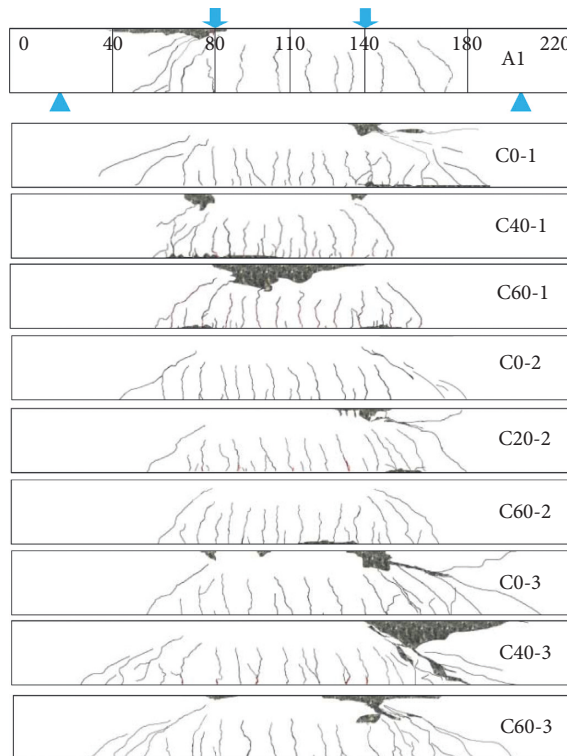


FIGURE 10: Distribution maps of cracks.

on the comprehensive bonding properties between the steel bar and concrete. Corrosion of steel bars caused by chloride leads to microcracks surrounded the steel bars. Bending stress makes the microcracks continue to develop and form the second type of major cracks. Therefore, such cracks occur above the corroded steel bars.

- (2) Minor cracks occur near the major cracks. The local bond stress between concrete and CFRP increases

with the increases of load. When the local tensile stress of concrete between major cracks reaches the ultimate tensile strength, the minor cracks appear between major cracks. Due to the low influence height of bond stress, such cracks are relatively short.

- (3) CFRP peeling cracks are the third kind of cracks. Arriving at the ultimate load, there has a tendency of local peeling between the CFRP and concrete at the beam bottoms, and the peeling cracks are short and inclined or even parallel to the bottom surface and intersect with the major cracks and then cause the peeling off of the CFRP and concrete.

3.3.2. Failure Modes. The failure modes of the test beams are shown in Figure 12. In the bending test, the major cracks in the pure bending span of the control beam are vertically upward and evenly distributed with the increase of load grade. When the ultimate load is reached, the concrete beams A1, C0-1, C40-1, C60-1, and C40-2 are crushed.

Under the chloride condition, the crack patterns and the numbers of unreinforced beams C0-3, C40-3, and C60-3 are similar to that of the control beam, and part of the major cracks are developed from the position where the steel bars or strand was corroded. In addition, the reduction in the cross-sectional area of the steel bars and stirrups leads to the weakening of shear capacity. Arriving at the ultimate load, the oblique cracks are penetrated from the support to the loading point, leading to the concrete crushing at the loading point, and the compressive strength of the concrete on the midspan was not fully utilized. And the structure is subjected to shear failure.

Compared with the control beam, the surface cracks in the CFRP reinforced beams are denser, and there are more short minor cracks and peeling cracks. For example, under natural conditions, the crack numbers of the CFRP reinforced beams in the midspan are about 1.7~2.3 times that of

TABLE 6: Parameters of cracks in the pure bending span.

Beam	Number	Average spacing (mm)	Height (mm)	Maximum width (mm)	Crack patterns	Failure mode
A1	7	91	170	0.18	MAC	CCF
C0-1	15	45	150	0.12		
C40-1	16	39	165	0.28		CCF, CRF
C60-1	12	52	155	0.25	MAC, MIC, PEC	
C0-2	12	47	155	0.12		
C60-2	14	42	150	0.15		CCF, CRF
C40-2	12	52	162	0.11		
C0-3	8	80	165	0.24		
C60-3	8	77	160	0.22	MAC	CCF, CSF
C40-3	9	74	155	0.20		

Note. MAC, major crack; MIC, minor crack; PEC, CFRP peeling crack; CCF, concrete crush failure; CSF, concrete shear failure; CRF, CFRP rupture failure.

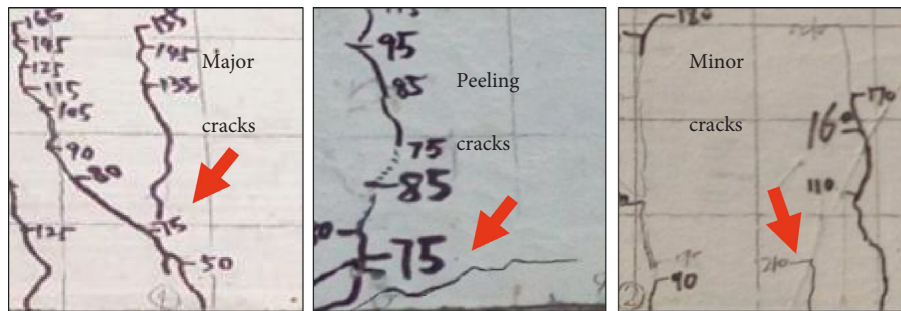


FIGURE 11: Classification of cracks.

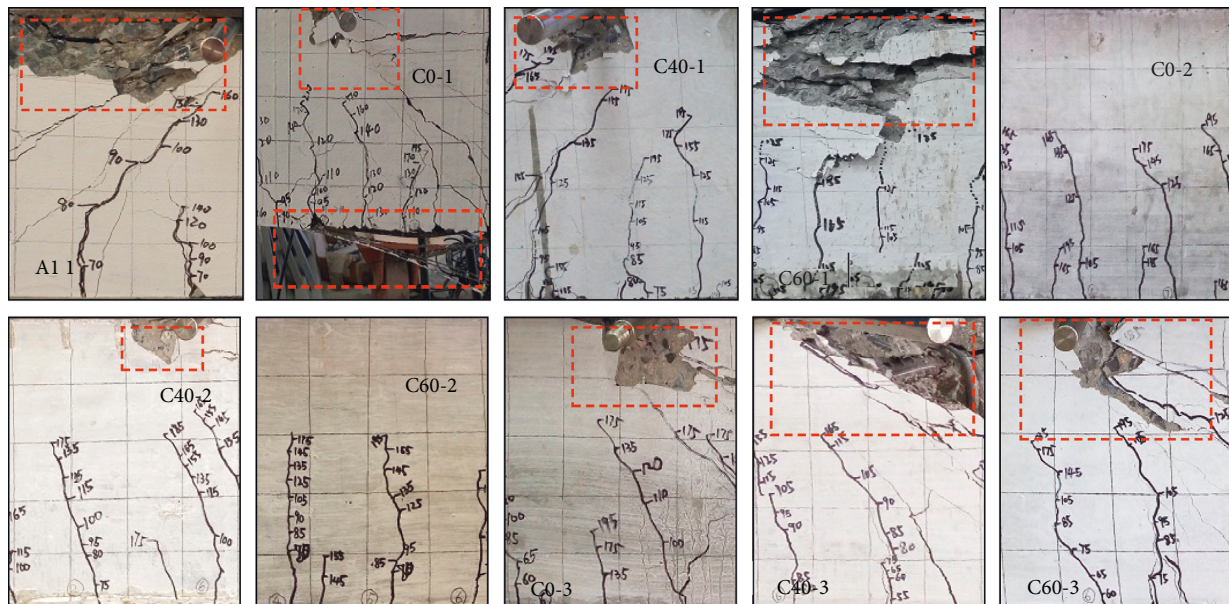


FIGURE 12: Failure modes of the test beams.

the control beam, and under chloride environment, the crack numbers of the CFRP reinforced beams in the midspan are about 1.5~2 times that of the control beam A1. Arriving at the ultimate load, the concrete of the CFRP reinforced beams in the midspan or under the loading point are crushed, and CFRP is fractured and peeled off. In this experiment, the damage on CFRP is not serious, which can

prevent the concrete from disintegrated and falling off on a large scale.

3.3.3. *Crack Widths.* The average widths of the major cracks on different heights of PC beams are shown in Figure 8. It can be seen that the crack widths shift linearly with the

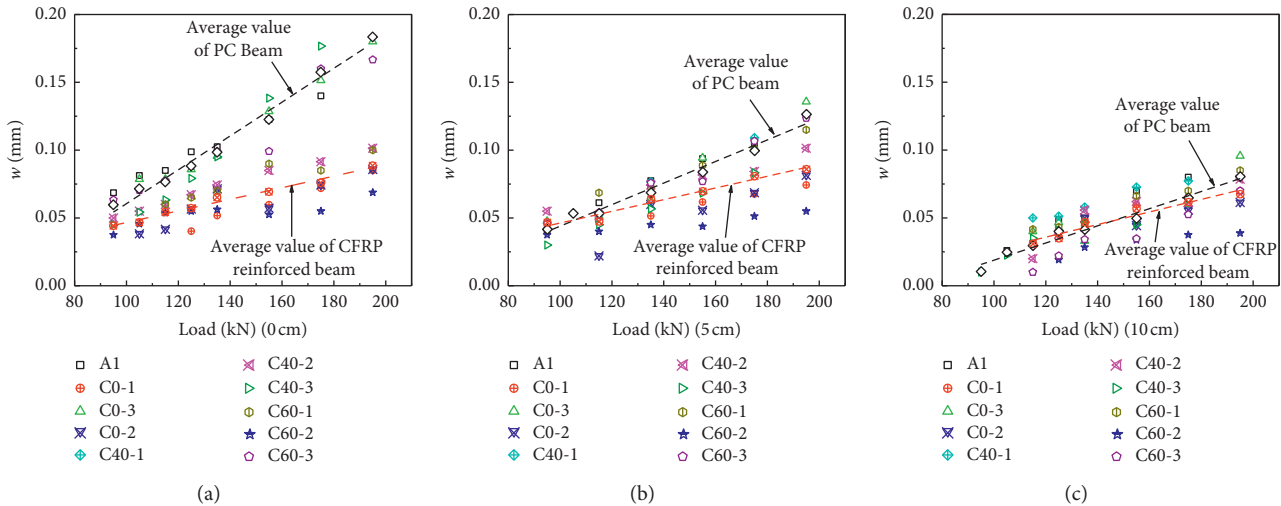


FIGURE 13: Crack widths and loads curves. (a) Average widths of cracks on the bottom, (b) at 5 cm, and (c) at 10 cm.

increase of load steps. The average widths of cracks on bottoms of CFRP strengthened beams C0-1, C0-2, C40-1, C40-2, C60-1, and C60-2 are all significantly smaller than that of the unreinforced beams A1, C0-3, C40-3, and C60-3. The cracking widths of the CFRP reinforced beams are slightly smaller than that of the unreinforced beams at a height of 5 cm from the beam bottom. At a height of 10 cm from the beam bottom, the gaps of the crack widths between the CFRP reinforced beams and the unreinforced beams are not obvious.

As can be seen from Figure 13, the reinforcement of CFRP has a greater impact on the development of cracks compared with initial damage and short-term chloride corrosion. Therefore, the average crack widths of CFRP reinforced and unreinforced beams were fitted with the linear method. When the load is 115 kN, the average crack widths of the CFRP reinforced beams at 0 cm, 5 cm, and 10 cm from the beam bottom decrease by 29%, 11%, and 5%, respectively, compared with that of the unreinforced beams. When the load is 195 kN, they decrease by 52.5%, 32.5%, and 17.5%, respectively. At the same time, the average crack widths of the unreinforced beams at 5 cm and 10 cm are 31.1% and 56.3% smaller than those at the bottom, while the average crack widths of the CFRP reinforced beams at 5 cm and 10 cm are only 3.1% and 24% smaller than those at the bottom.

The cracking rates of the test beams are shown in Figure 14. The cracking rates of unreinforced beam gradually decrease with the increase of cracking heights. For example, the cracking rate at the beam bottom is $1.25 \mu\text{m}/\text{km}$, and the cracking rate at 5 cm and 10 cm decreased by 36.4% and 71.0%, respectively. The cracking rates of the CFRP reinforced beams at 0 cm, 5 cm, and 10 cm are almost same, and the cracking rates are 65.8%, 45.7%, and 26.7% lower than that of the unreinforced beams, respectively.

In conclusion, the average crack widths and cracking rates of the CFRP reinforced beams at the same heights are always smaller than those of the unreinforced beams, and the gaps between them increase with the load steps and decrease with the increase of crack heights. Initial damage and short-term

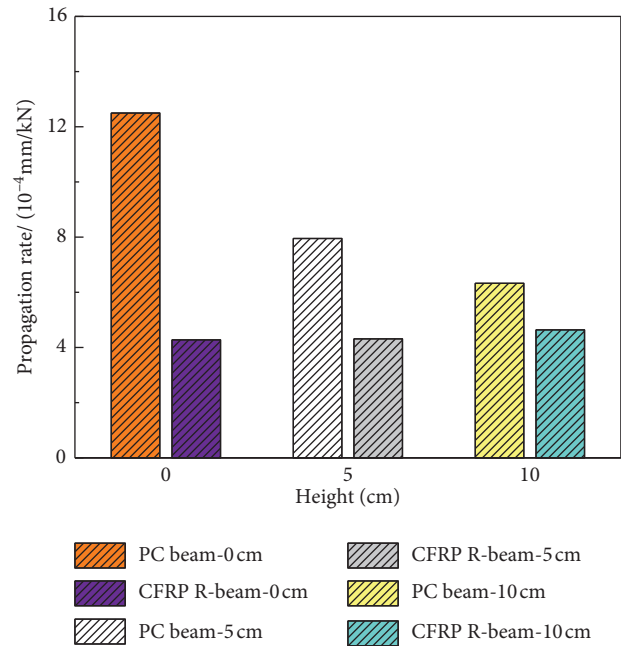


FIGURE 14: Cracking rates.

chloride corrosion have no obvious effects on the process of cracking. However, CFRP has a significant constraint on the development of cracks, and the effect decreases with the increase of crack heights. Also, the influence height of constraint is related to the thickness, layer numbers of CFRP, and other factors, which need to be further studied.

4. Conclusions

Ten pretensioned concrete beams designed with different test conditions were tested. And the effects of initial cracks, CFRP reinforcement, and chloride corrosion on the flexural behavior, cracking characteristics, and failure modes were discussed. The following conclusions can be drawn based on the test.

- (1) Considering the initial cracks, chloride corrosion, and CFRP reinforcement, the sectional strain of the test beams still follows the plane section assumption after a pure bending deformation.
- (2) The initial flexural stiffness is reduced by initial cracks and chloride corrosion, and CFRP reinforcement has little effect on the initial flexural stiffness. Before cracking, the flexural stiffness of the test beams is basically unchanged with the load steps. In the cracking stage, the stiffness decreases with the increase of load steps. And CFRP pasted on the beam bottom exerts its high tensile performance in this stage, inhibits the structural deformation, and reduces the degradation rate of flexural stiffness compared with the control beam.
- (3) The effect of chloride corrosion increases with the degree of initial cracks. Under the chloride condition of 120 d, the effective prestress of the PC beams is weakened, cracking loads and ductility are reduced, and the ultimate loads are reduced by less than 10%. And the failure mode is prone to change from concrete crushing failure to shear failure. After the reinforcement of CFRP, the cracking loads of the test beams increase, the ductility of these beams is reduced compared to the control beam and increased compared to the chloride corrosion beams, and the ultimate loads increase than the control beam by 12.8%~18.7%. When the three factors are coupled, the enhancement effect of CFRP is more obvious than the weakening effects of short-term chloride corrosion and initial damage.
- (4) CFRP reinforcement has a constraint effect on the development of cracks, and the effect decreases with the increases of crack height. Therefore, the average crack width and cracking rate of the CFRP reinforced beams at the same height are always smaller than those of the unreinforced beams. When the load grade is 195 kN, the average crack widths of the CFRP reinforced beams at 0 cm, 5 cm, and 10 cm from the beam bottom are 52.5%, 32.5%, and 17.5% smaller than that of the unreinforced beams, and the cracking rates are reduced by 65.8%, 45.7%, and 26.7%, respectively.

Data Availability

The data used to support the findings of this study are included within the article.

Conflicts of Interest

The authors declare that they have no conflicts of interest.

Acknowledgments

This work was conducted with the financial support from the National Natural Science Foundation of China (grant nos. 51578099 and 51178069). The support is gratefully acknowledged.

References

- [1] M. P. Torill and R. E. Melchers, "Performance of 45-year-old corroded prestressed concrete beams," *Structures and Buildings*, vol. 166, pp. 547–559, 2013.
- [2] P. Colajanni, A. Recupero, G. Ricciardi, and N. Spinella, "Failure by corrosion in PC bridges: a case history of a viaduct in Italy," *International Journal of Structural Integrity*, vol. 7, no. 2, pp. 181–193, 2016.
- [3] F. Li, Y. Yuan, and C.-Q. Li, "Corrosion propagation of prestressing steel strands in concrete subject to chloride attack," *Construction and Building Materials*, vol. 25, no. 10, pp. 3878–3885, 2011.
- [4] L. Wang, X. Zhang, J. Zhang, J. Yi, and Y. Liu, "Simplified model for corrosion-induced bond degradation between steel strand and concrete," *Journal of Materials in Civil Engineering*, vol. 29, no. 4, article 04016257, 2017.
- [5] L. Wang, X. Zhang, J. Zhang, L. Dai, and Y. Liu, "Failure analysis of corroded PC beams under flexural load considering bond degradation," *Engineering Failure Analysis*, vol. 73, pp. 11–24, 2017.
- [6] F. Li and Y. Yuan, "Effects of corrosion on bond behavior between steel strand and concrete," *Construction and Building Materials*, vol. 38, pp. 413–422, 2013.
- [7] F.-M. Li and Y.-S. Yuan, "Experimental study on bending property of prestressed concrete beams with corroded steel strands," *Journal of Building Structures*, vol. 31, no. 2, pp. 78–84, 2010.
- [8] Z. Rinaldi, S. Imperatore, and C. Valente, "Experimental evaluation of the flexural behavior of corroded P/C beams," *Construction and Building Materials*, vol. 24, no. 11, pp. 2267–2278, 2010.
- [9] X. Zhang, L. Wang, J. Zhang, Y. Ma, and Y. Liu, "Flexural behavior of bonded post-tensioned concrete beams under strand corrosion," *Nuclear Engineering and Design*, vol. 313, pp. 414–424, 2017.
- [10] R. Yang, J. Zhang, L. Wang et al., "Experimental research for flexural behavior on concrete beams with local corrosion fracture of strands," *Journal of Central South University (Science and Technology)*, vol. 49, no. 10, pp. 2593–2601, 2018.
- [11] M. A. Vicente, D. C. González, and J. A. Martínez, "Mechanical response of partially prestressed precast concrete I-beams after high-range cyclic loading," *Practice Periodical on Structural Design and Construction*, vol. 20, no. 1, pp. 1–22, 2015.
- [12] A. Recupero and N. Spinella, "Preliminary results of flexural tests on corroded prestressed concrete beams," in *Proceedings of the Fib Symposium 2019: CONCRETE-Innovations in Materials, Design and Structures*, pp. 1323–1330, Kraków, Poland, May 2019.
- [13] A. Dasar, R. Irmawaty, H. Hamada, Y. Sagawa, and D. Yamamoto, "Prestress loss and bending capacity of pre-cracked 40 year-old PC beams exposed to marine environment," *Matec WEB of Conferences*, vol. 47, article 02008, 2016.
- [14] N. Spinella, P. Colajanni, A. Recupero, and F. Tondolo, "Ultimate shear of RC beams with corroded stirrups and strengthened with FRP," *Buildings*, vol. 9, no. 2, p. 34, 2019.
- [15] E. M. Adham and S. Khaled, "Flexural behavior of corroded pretensioned girders repaired with CFRP sheets," *PCI Journal*, vol. 59, no. 2, pp. 129–143, 2014.
- [16] I. Shaw and B. Andrawes, "Repair of damaged end regions of PC beams using externally bonded FRP shear reinforcement," *Construction and Building Materials*, vol. 148, pp. 184–194, 2017.

- [17] L. K. Jarret, K. A. Harries, R. Miller, and R. J. Brinkman, "Repair of prestressed-concrete girders combining internal strand splicing and externally bonded CFRP techniques," *Journal of Bridge Engineering*, vol. 19, no. 2, pp. 200–209, 2014.
- [18] E. R. Calvin and R. J. Peterman, "Evaluation of prestressed concrete girders strengthened with carbon fiber reinforced polymer sheets," *Journal of Bridge Engineering*, vol. 9, no. 2, pp. 185–192, 2004.
- [19] D. Cerullo, K. Sennah, H. Azimi, C. Lam, A. Fam, and B. Tharmabala, "Experimental study on full-scale pre-tensioned bridge girder damaged by vehicle impact and repaired with fiber-reinforced polymer technology," *Journal of Composites for Construction*, vol. 17, no. 5, pp. 662–672, 2013.
- [20] A. Elsafty, M. K. Graeff, and S. Fallaha, "Behavior of laterally damaged prestressed concrete bridge girders repaired with CFRP laminates under static and fatigue loading," *International Journal of Concrete Structures and Materials*, vol. 8, no. 1, pp. 43–59, 2014.
- [21] Y. Liu, Y. Fan, J. Yu et al., "Flexural behavior test of corroded prestressed concrete beams under chloride environment," *Acta Materiae Compositae Sinica* no. 37, In press, in Chinese.

Research Article

Effect of Sulphate and Chloride Ingress on Selected Cements Mortar Prisms Immersed in Seawater and Leather Industry Effluent

Jackson Muthengia Wachira ¹, Reginah Wangui Ngari,² Joseph Karanja Thiong'o,² and Joseph Mwiti Marangu ³

¹Department of Physical Sciences, University of Embu, Embu, Kenya

²Department of Chemistry, Kenyatta University, Nairobi, Kenya

³Department of Physical Sciences, Meru University of Science & Technology, Meru, Kenya

Correspondence should be addressed to Joseph Mwiti Marangu; jmarangu2011@gmail.com

Received 15 May 2019; Accepted 15 July 2019; Published 21 August 2019

Guest Editor: Charis Apostolopoulos

Copyright © 2019 Jackson Muthengia Wachira et al. This is an open access article distributed under the Creative Commons Attribution License, which permits unrestricted use, distribution, and reproduction in any medium, provided the original work is properly cited.

Cement structures are major capital investments globally. However, exposure of cement-based materials to aggressive media such as chloride- and sulphate-laden environments such as coastal areas affects their performance. Ordinary Portland cement (OPC) is the main cement used in buildings and civil structures such as dams and bridges. This paper reports the findings of an experimental investigation on the effect of ingress of Cl^- and SO_4^{2-} on compressive strength development and the ions' diffusivity in selected OPC brands in Kenya. The aggressive media used included seawater (SW) and wastewater from leather industry (WLI). Three brands of commonly used cements of OPC in Kenya were used. Mortar prisms were prepared from each brand of cement at different water-to-cement ratios (w/c) of 0.5, 0.6, 0.65, and 0.7 and allowed to cure for 28 days in a highly humid environment. The aggressive ions' ingress in the mortar prisms was accelerated using a potential difference of $12 \text{ V} \pm 0.1 \text{ V}$. Analysis of diffusivity and diffusion coefficient of Cl^- and SO_4^{2-} was finally done. Compressive strength analysis was done before (at the 2nd, 7th, 14th, and 28th day) and after exposure to the aggressive ions. The results showed that the diffusivity of chlorides was more pronounced than that of sulphates. Diffusivity was observed to be higher at higher w/c ratios for all cement categories. It was observed that compressive strength increased with curing age, with the highest observed at 28 days. Cement A was generally found to have the highest compressive strength for all w/c ratios. The compressive strength was observed to increase after the mortar prisms were exposed to SW as opposed to the ones exposed to WLI. Generally, it was also observed that the strength gain increased with increase in w/c. The loss in strength was also observed to increase with increase in w/c.

1. Introduction

Long-term durability of concrete structures is the main concern for safety and economic reasons. Deterioration of concrete structures is generally caused by ingress of aggressive agents into the concrete [1]. A large number of concrete structures such as harbors, decks, piers, floating offshore platforms, power plants, and waste disposal facilities are generally subjected to environments which contain aggressive agents [2]. These aggressive agents may include sulphates, chlorides, moisture, and carbon (IV) oxide [2].

The steel rebar corrosion of the reinforced concrete (RC) caused by the ingress of chloride ions is the most severe problem affecting the durability of concrete constructions, especially in saline environments. Once a sufficient quantity of chloride has been accumulated on the surface of the embedded steel rebar, pitting corrosion will occur [3]. Corrosion of RC is a problem throughout the world, demanding significant amounts for repair and rehabilitation. Extensive research has been done to establish relationships between the chloride ions content and the onset of corrosion [4–8]. Haque and Kayyali [9] showed that not all chloride

ions that ingress into concrete remain free in the pore solution. Some of the ions get bound by the hydration products in a chemical reaction to form chloroaluminate hydrate. The portion of chloride ions that remains free is responsible for causing damage to the RC structures. Elsewhere, Sagüés [10] observed that the concentration level of Cl^- to OH^- (Cl^-/OH^-) in the pore solution determines the depassivation of steel rebar in the concrete, while Mundra et al. [11] suggested that, for external chlorides, the Cl^-/OH^- ratio below 3 does not cause significant corrosion but with internal chlorides, corrosion will occur at a lower level.

Sulphate attack is considered a major deteriorative problem occurring when the cement-based materials, such as concrete, mortars, and buildings, are exposed to sulphate ions environment [12]. The sources of aggressive ions to the mortar/concrete may include deicing salts, seawater, groundwater, bacterial action in sewers, wastewater from industries, use of sulphate or chloride contaminated mix water, and natural gypsum in the aggregate, among others [1, 13–16].

In the leather-making industry, a great deal of wastewater containing high concentrations of sulphate is discharged which comes from many processes such as liming, deliming, bating, pickling, and chrome tanning [17]. This wastewater with high concentrations of sulphates is not treated especially in tannery, but discharged directly into the integrated wastewater [17, 18]. These ions may be carried into inner sections of concrete by ionic diffusion, capillary absorption, permeation, and convective flow through the pore system, among others [19].

Ordinary Portland cement (OPC) is the main cement used in buildings and civil structures such as dams and bridges in Kenya [1]. It is mostly preferred to blended cements due to the fact that it exhibits shorter setting times and achieves high early strength (28 days) than blended cements [1, 20]. However, it is more prone to attack by aggressive media, for example, chlorides and sulphates, among others. This is attributed to the fact that the hydration of OPC results in production of about 20 percent by weight of $\text{Ca}(\text{OH})_2$, which makes it highly susceptible to the aggressive ions [1]. This potentially results in degradation of the cement-based structures. This subsequently reduces the service life of these structures. The use of OPC has continued regardless. In the Kenyan market, there are many brands of OPC, yet not much study has been carried out on their resistance to ingress of aggressive of Cl^- and SO_4^{2-} ions. Therefore, the present study aimed at investigating the effect of ingress of Cl^- and SO_4^{2-} on compressive strength development and the ions diffusivity in selected OPC brands in Kenya. The aggressive media used included seawater (SW) and wastewater from leather industry (WLI).

2. Materials and Methods

2.1. Materials. Materials were sampled from their respective places in Kenya. OPC (42.5 N/mm) was obtained from the respective appointed distributors in Nairobi, Thika Town, and Githurai Township in Kenya, respectively. Letters A, B, and C are used to refer to OPCs from companies A, B, and C,

respectively. For each company cement category, 20 kg was procured from the appointed distributor in the respective towns. The 20 kg of each cement category was mixed thoroughly to make a homogeneous 60 kg sample in each cement category.

Seawater from the Indian Ocean and Pirates Beach, Mombasa County, Kenya, and wastewater from Leather Industries of Kenya Limited, Thika, Kiambu County were used. The seawater and wastewater from leather industry were labelled as SW and WLI, respectively.

River sand was obtained from sand transporters and distributors in Githurai Township, Kiambu County, Kenya. Sand as obtained from the sampling point was washed by spraying tap water and sun-dried for two days to a constant weight (ASTM C0117, 2004). The dried sand was sieved to meet the standard sand aggregates grade (ASTM C 593, 2005). To remove coarse materials, the dry sand was sieved through a 2360 μm sieve. The aggregates that passed through the 2360 μm sieve were then passed through a series of sieves which were 1180 μm , 600 μm , 300 μm , and 150 μm (ASTM C 593, 2005). Standard sand was finally prepared by mixing 384.00 g of sand retained on 1180 μm sieve, 427.00 g of sand retained on 600 μm sieve, 181.00 g of sand retained on 300 μm sieve, 223.00 g of sand retained on 150 μm , and 135.00 g of sand that passed through a 150 μm sieve to make 1350 g of standard sand (ASTM C 593, 2005). The sand retained in each sieve was stored in dry polythene bags until needed.

2.2. Methods

2.2.1. Preparation of Mortar Prisms. Mortar prisms measuring 40 mm \times 40 mm \times 160 mm were prepared in accordance with EAS 148-1:2000. In this regard, 450 ± 1 g of different brands of OP was separately weighed and placed in the mixing bowl of an automatic programmable mixer, model number 1305. For a water-to-cement ratio of 0.5, 225 ± 1 ml of distilled water was then added. The mixing bowl with its contents was clamped onto the mixer. 1350 ± 1 g of the graded sand was placed in an automatic pour trough and added automatically to the mixing bowl little by little while the machine was running at a speed of 30 revolutions per second. The machine was allowed to run for ten minutes. The mould and the hopper were firmly mounted on the vibrating table after the vibrator had been switched on. The first layer of the mortar into the compartments of the mould was placed from right to left of the mould within 15 ± 1 seconds so that the compartments were approximately half-full. After an interval of 15 ± 1 seconds, during which the vibrator remained running, the second layer was placed in the mould within the next 15 seconds, again working from right to left. The vibrator switched off automatically after 120 ± 1 seconds. The excess mortar was removed using a straightedge spreader. The surface of the mortar was smoothed using the same straightedge spreader held almost level. The vibration machine mould clamps were loosened to release the mould. The mould with the mortar was gently lifted off the vibrating table and stored

in a cabinet maintained at $22 \pm 1^\circ\text{C}$. The mortar prisms were left in the mould for 24 hours after which they were demoulded and marked with a crayon marker for identification. The mortars were finally cured in deionized water for additional 27 days in a curing room maintained at $22 \pm 1^\circ\text{C}$. To prepare 0.6, 0.65, and 0.7 w/c ratio mortar, 270 ± 1 ml, 292.5 ± 1 ml, and 315 ± 1 ml water was used, respectively, following the same procedure. 27 mortar prisms were made for each category of cement.

Compressive strength measurements were taken using compressive strength machine model number ADR-Auto 250 at the age of 2, 7, 14, and 28 days and after separate curing in tap water and aggressive media. The 28-day water-cured mortars were also exposed to aggressive media for 36 hours, and the changes in the compressive strength after exposure were calculated using the following equation:

$$\%CS_{\text{gain/loss}} = \frac{CS(\text{after exposure}) - CS(28^{\text{th}} \text{ day})}{CS(28^{\text{th}} \text{ day})}, \quad (1)$$

where $\%CS_{\text{gain/loss}}$ is the calculated percent gain or loss in compressive strength, $CS(\text{after exposure})$ is the strength after exposure, and $CS(28^{\text{th}} \text{ day})$ is the strength at the 28th day.

For each category of cement, three prisms were removed from the curing tank; any deposits wiped out and covered with a damp cloth until tested. Their identities were noted down. A prism was placed in the test machine with one face on the supporting rollers and with its longitudinal axis normal to the supports. The load was then applied vertically by means of the loading roller at a rate of 50 N/s until failure to obtain prism halves. The prism halves were kept damp until tested. The halves were then crushed by smoothly applying load at a rate of 2400 ± 200 N/s. Triplicate measurements of compressive strength were taken.

2.2.2. Chemical Analysis of Test Cements. About 100 g of each cement sample was pulverized to pass through a $76 \mu\text{m}$ sieve and used for the analysis of cement oxides in accordance with KS EAS 18:2008.

(1) Analysis of Al_2O_3 , SiO_2 , and Fe_2O_3 . Analysis of Al_2O_3 , SiO_2 , and Fe_2O_3 was carried out in accordance with KS EAS 18:2008. A buffer solution was prepared by dissolving 2.5 g of $\text{SnCl}_2 \cdot \text{H}_2\text{O}$ in 10 ml concentrated HCl in a 100 ml volumetric flask. The solution was then topped to the mark with distilled water. 1000 ppm stock solution of aluminium was prepared by dissolving 1.0 g of aluminium in 20.0 ml HCl and 1 ml of HgNO_3 in a 1000 ml volumetric flask. The resultant solution was then topped to the mark using distilled water. For the preparation of working standards, 10.0 ml of the stock solution was put in a 100 ml volumetric flask. 2.0 ml of the buffer solution and 2.0 ml of a potassium chloride solution containing 100 g/l were then added. The resultant solution was then topped to the mark using distilled water. From the working standards, solutions of 20 ppm, 40 ppm, 60 ppm, and 100 ppm were made through serial dilutions. SiO_2 and Fe_2O_3 standards were made through serial dilution of titrosol solutions of the oxides

provided with the AAS machine. 0.100 g of the pulverized cement sample was weighed and placed at the bottom of a 100 ml plastic bottle. 1.0 ml of aquarengia ($\text{HNO}_3 : \text{HCl}, 1 : 3$) and 3.0 ml of hydrofluoric acid were added and the bottle was corked. The mixture was then stirred taking care so as to maintain the sample at the bottom of the bottle. The resultant mixture was allowed to stand for 12 hours. 50.0 ml of boric acid was added, and the solution was left to stand for one hour. The resultant solution was topped to the mark using distilled water and left to stand for two hours. AAS model AA.10 was used to determine the amounts of Al_2O_3 , SiO_2 , and Fe_2O_3 . Calibration of the machine was done using the working standard solution diluents and the blank solution. Analyses were done in triplicate. Each time analysis was done, the standard solutions were prepared afresh.

(2) Analysis of CaO and MgO. Analysis was done according to KS EAS 18:2008. A buffer solution was prepared by dissolving requisite amounts of La_2O_3 and CsCl in 20.0 ml distilled water–25.0 ml concentrated HCl mix in a 100 ml volumetric flask. The resultant solution was then topped to the mark using distilled water. 1000 ppm of CaO and 200 ppm of MgO stock solution was prepared by dissolving 2.5 g anhydrous CaCO_3 and 0.7 g of anhydrous MgCO_3 in 500.0 ml of 1 : 4 nitric acid : distilled water mixture in a 1000 ml volumetric flask. 20.0 ml of the buffer solution was added to the solution, and the resultant solution was topped to the mark using distilled water. From the stock solution, 50, 100, 300, and 500 ppm CaO and 10, 20, 60, and 100 ppm MgO were prepared through serial dilution. Blank solution was prepared using the same procedure but without the addition of CaCO_3 or MgCO_3 . 0.5 g pulverized cement sample and 0.5 g of ammonium acetate were mixed in a 250 ml beaker. 10.0 ml of concentrated HCl was added into the beaker while stirring until no more bubbles were observed. The beaker's content with a glass cover lid was heated over a water bath at $80\text{--}100^\circ\text{C}$ for about 30 minutes. 50.0 ml hot water was added while stirring. The solution was then filtered through a Whatman filter paper number 542 into a 1000 ml volumetric flask. The residue was washed with 5.0 ml hot concentrated HCl twice followed by hot water until it was confirmed free of chloride ions using AgNO_3 solution. 10 ml buffer solution was added to the solution while stirring. The solution was cooled and then topped to the mark using distilled water. Analysis was then done in triplicate using AAS model AA.10. Calibration curve was prepared from the stock solution diluents and the blank solution. Each time analysis was done, standard solutions were prepared afresh.

(3) Analysis of K_2O and Na_2O . A buffer solution was prepared by dissolving 30.0 g aluminium in 400 ml of 50% HNO_3 acid in a 1000 ml volumetric flask, and the solution was topped to the mark using distilled water and mixed well by inversion. 500 ppm K_2O and 250 ppm Na_2O stock solution was prepared by dissolving 0.7915 g KCl and 0.4715 g NaCl in 500 ml distilled water in a 1000 ml volumetric flask. To the resultant solution, 20.0 ml buffer solution was added and the solution was topped to the mark using distilled water. From the stock solution, 10, 20, 30, 40, and 50 ppm K_2O and 5, 10, 15, 20, and

25 ppm Na₂O were prepared through serial dilution. In each case, an amount of concentrated HCl equivalent to half the amount of the stock solution was added. Blank solutions were made using the same procedure but without the addition of KCl and NaCl. 0.5 g of the pulverized cement sample was put in a 50 ml beaker and 25.0 ml distilled water and 5.0 ml concentrated HCl were added as stirring continued. The resultant solution was topped to the mark using distilled water and heated to boiling on a hot plate for fifteen minutes. The solution was filtered through a Whatman filter paper number 542 into a 500 ml volumetric flask. The filter paper was washed six times with hot water. 10.0 ml of the buffer solution was added to the solution while stirring. The solution was cooled and then topped to the mark using distilled water. Calibration curve was prepared using the stock solution diluents and the blank solution. Analysis in triplicate was finally done by flame photometry using flame photometer number WFX 210A.

2.2.3. Bogue's Calculation of the Major Cement Phases. Bogue's equations given in (2)–(5) were used to calculate the approximate mineralogical composition of the major phases in OPC based on the data obtained from chemical analysis [21]:

$$C_3S = 4.071CaO - 7.6SiO_2 - 6.718Al_2O_3 - 1.43Fe_2O_3 \quad (2)$$

$$C_2S = 2.867SiO_2 - 0.7544C_3S \quad (3)$$

$$C_3A = 2.65Al_2O_3 - 1.692Fe_2O_3 \quad (4)$$

$$C_4AF = 3.043Fe_2O_3 \quad (5)$$

The approximate mineralogical compositions of the cements were presented in percentages of the main phases.

2.2.4. Migration Test. Migration test was carried out in accordance with ASTM C 1556 (2004). The mortar prisms cured for 28 days were cut to 100 mm length using a cutting machine model number MC 100 type EFNOUT KT with a 2.0 mm diamond blade. An electrochemical cell setup consisting of 500 ml of 0.3 M NaOH was placed in the anodic compartment and an equal volume of SW, WLI, or TW was placed in the cathodic compartment. Stainless steel electrodes were then placed in the two compartments as the electrodes. The electrodes were connected to a 12 V ± 0.1 V electric source. Current between the two electrodes was recorded using a milliampere ammeter after every 30 minutes. Temperature was also monitored throughout the exposure period. The exposure period of 36 hours started when the solutions were placed in the respective compartments, covered, and the electrodes were connected in the circuit. The solutions were stirred periodically using a glass rod.

After the exposure period, the mortar prisms were removed from the setup and allowed to drain for about 20 minutes. Three mortar prisms were subjected to

compressive strength analysis while the other three were subjected to chloride and sulphate profiling. The mortar prisms were sliced into 10 mm slices using a well-oiled block cutter model MC-100 number 88-07-521 with a 2.0 mm diamond blade. The slices were then dried in an oven Binder model at 50–70°C for 60 seconds ± 5 seconds. Each slice was pulverized using a standard pulverizing machine Siebtechnik model TS 250 so as to pass through a 76 μm mesh sieve. Each pulverized sample was stored in a dry well-labelled plastic container and shaken well to enhance mixing. The pulverizer machine basins were thoroughly cleaned and dried before another sample was ground. The pulverized samples were then analyzed for chlorides and sulphates. Triplicate analyses were done for each cement category.

2.2.5. Sulphate Analysis. Sulphate analysis was done using the turbidimetric method in accordance with ASTM C 1580 (2007). Buffer solution was prepared by mixing 30.0 g magnesium chloride, MgCl₂·6H₂O, 5.0 g sodium acetate, CH₃COONa·3H₂O, 10.0 g potassium nitrate, KNO₃, and 20.0 ml acetic acid, and CH₃COOH in 500 ml distilled water and made up to 1000 ml using distilled water. A 100 ppm sulphate stock solution was prepared by dissolving 0.1479 g anhydrous sodium sulphate, Na₂SO₄, in 500.0 ml distilled water in a 1000 ml volumetric flask, and the resultant solution was made to the mark using distilled water. From the stock solution, 1 ppm, 5 ppm, 10 ppm, 20 ppm, and 30 ppm were prepared through serial dilutions. The diluents were used to prepare the calibration curve.

Ten grams of the pulverized sample was placed in a 250 ml beaker, and 75 ml of distilled water was added slowly while stirring. The solution was placed on a hot plate and allowed to boil for two minutes then diluted to 100 ml using distilled water and heated for 15 minutes. The resultant solution was then filtered using Whatman filter paper number 542 into a beaker. The residue was washed with hot water until no white precipitate was formed when AgNO₃ solution was added to the filtrate. The filtrate was diluted to 250 ml and boiled. 10 ml of the diluted sample solution was placed in a 250 ml conical flask. 20 ml buffer solution was added, and the resultant solution was stirred with a magnetic stirrer, while stirring about 0.2 g of BaCl₂ was added and the solution was stirred at a constant speed for 60 ± 2 seconds. The resultant solution was left to sit for five minutes during which the absorption cell was filled with distilled water and used to zero the instrument at 420 nm wavelength. Analysis of the samples was run on a Beckman DU 520 spectrophotometer. The sample solution was then transferred into the cell of the photometer and turbidity measured at 5 ± 0.5 minutes. The same procedure was applied to the standards and their turbidity determined. The turbidity of the test solution was calculated by taking the difference between solution with BaCl₂ and the one without. Calibration curves were used to determine sulphate concentration in ppm of cement. Triplicate analyses were done for each category of the test cement. The results were presented as sulphate concentration versus depth of ingress. From the graph, sulphate diffusion coefficients, D_{app} , were derived

from error fitting curves in equation (6) using the method of least squares [22].

$$\frac{\partial C}{\partial t} = D \frac{\partial^2 C}{\partial x^2}, \quad (6)$$

where C is the concentration of the aggressive ion at a depth x and at the moment t and D is the diffusion coefficient.

The diffusion of chloride or sulphate ions in concrete is approximated from solution to Fick's second law equation [23] under non-steady-state conditions assuming boundary conditions $C_{(x,t)} = 0$ at $t = 0$, $0 < x < \infty$, $C_{(x,t)} = C_s$ at $x = 0$, $0 < t < \infty$, constant effects of coexisting ions, linear chloride binding, and one-dimensional diffusion into semi-infinite solid. The analytical solution to equation (7) is equation (8) [23, 24]:

$$C_{(x,t)} = C_s \left[1 - \operatorname{erf} \left(\frac{x}{2\sqrt{D_{\text{mig}}t}} \right) \right], \quad (7)$$

where $C_{(x,t)}$ is the concentration of the ion at any depth x in the mortar bulk at time t , C_s is the surface concentration while D_{mig} is the migration diffusion coefficient and erf is the error function. Apparent diffusion coefficients, D_{app} , are calculated from the following equation:

$$D_{\text{app}} = \frac{D_{\text{mig}} RT \text{Int}^2}{Z_i F \Delta E}, \quad (8)$$

where ΔE is the effective applied voltage in V, t is the duration of exposure in seconds, D_{app} is the apparent diffusion coefficient, and D_{mig} is the migration diffusion coefficient.

2.2.6. Chloride Analysis. Cl^- analysis was carried out using the Mohr method, precipitation titration. A 5% K_2CrO_4 indicator was prepared by dissolving 1.0 g of K_2CrO_4 in 20.0 ml of distilled water. Standard (0.1 M) AgNO_3 solution was prepared by dissolving 9.0 g of AgNO_3 in about 200.0 ml distilled water in a 500 ml volumetric flask and the solution topped to the mark using distilled water. The resultant solution was standardized against NaCl. NaCl was dried for one hour at 140°C in an oven and cooled to room temperature in desiccators. 0.25 g portions of NaCl were weighed into a 250 ml Erlenmeyer flask and dissolved in about 100.0 ml of distilled water. Small quantities of NaHCO_3 were added until effervescence ceased. About 2 ml of K_2CrO_4 was added and the solution was titrated to the first permanent appearance of red colour.

Individual 10.0 g pulverized sample was placed in a 250 ml Erlenmeyer flask. 150 ml of 2:1 nitric acid:distilled water was added to the sample in the flask. A glass cover lid was placed, and the flask and its content were placed on a hot plate until the volume of the solution reduced to about 100 ml. The solution was allowed to cool for about 15 minutes. The solution was then neutralized by adding small quantities of calcium carbonate until effervescence ceased. The solution was then filtered through a Whatman filter paper number 541 into a 200 ml volumetric flask. The filter paper was rinsed thrice with distilled water, and the

resultant solution was topped to the mark. 10.0 ml aliquot of the solution was pipetted into a conical flask. About 2.0 ml the indicator was added, and titration was carried out in the usual way with the 0.1 M AgNO_3 . Triplicate analyses were done for each cement category. A chloride-free CaCO_3 blank was run through the same procedure. The amount of chloride was determined using the following equation:

$$[\text{Cl}^-] = \frac{3.5450(V_1 - V_2)M}{W}, \quad (9)$$

where V_1 is the volume of AgNO_3 solution used for sample titration (equivalent point), V_2 is the volume of AgNO_3 solution used for blank titration (equivalent point), M is the molarity of AgNO_3 solution, and W is the weight of sample in grams.

The results were represented in chloride profiles. From the profiles, chloride diffusion coefficients, D_{mig} , were derived from error fitting curves in equation (7) using the method of least squares. Apparent diffusion coefficients, D_{app} , were calculated using equation (8).

2.2.7. Chemical Analysis of SW and WLI. About 500 ml of each media was sampled for the analysis of Na^+ , K^+ , Ca^{2+} , Mg^{2+} , Cl^- , and SO_4^{2-} . The samples were filtered to remove solid matter. Sodium and potassium ion concentrations were analyzed using flame photometry, while Ca^{2+} and Mg^{2+} were analyzed using atomic absorption technique. Buffer solutions for the analysis of Ca^{2+} and Mg^{2+} were prepared as described in Analysis of CaO and MgO in Section 2.2.2 and for Na^+ and K^+ as described in Analysis of K_2O and Na_2O in Section 2.2.2. Sulphate concentration in sampled SW and WLI was determined using the procedure described in Section 2.2.5 while chloride concentration was determined using the procedure described in Section 2.2.6.

3. Results and Discussion

3.1. Chemical Analysis of the Test Cements. Table 1 gives the results for chemical analysis of oxides in percent by mass (except for Cl^-) of the test cements.

Table 2 gives the results of the Bogue calculation.

From Table 1, it was observed that for all the test cements, the sum of the proportions of CaO and SiO_2 was at least 50 percent by mass. This allows the formation of the most important cement phases during the formation of clinkers. The phases are C_3S and C_2S . Kenya Standards stipulates a minimum of 50 percent by mass of CaO and SiO_2 for OPC (KS EAS 18-1:2001). The ratio (CaO/SiO_2) was 2.99, 3.00, and 2.99 for cements A, B, and C, respectively. The Kenya Standards stipulates a minimum of 2.0 for OPC. From Bogue's approximations, all the test cements met the two-thirds by mass of calcium silicates (C_3S and C_2S) stipulated by the Kenya Standards. The silicates upon mixing with water hydration make cement gain strength.

The Kenya Standards (KS EAS 18-1:2001) stipulates a maximum of 0.10 percent of chloride content and a maximum of 3.5 percent sulphate of SO_3 . From the results, all the test cements used in this study met this requirement. In the chemical analysis of cement, gypsum is indicated by SO_3 . The

TABLE 1: Results for chemical analysis of the test cements in percent by mass.

Oxide (%)	Sample		
	A	B	C
SiO ₂	21.721 ± 0.1655	20.786 ± 0.2257	20.078 ± 0.3202
CaO	64.956 ± 0.0524	62.400 ± 0.2212	60.221 ± 0.3129
Al ₂ O ₃	3.624 ± 0.0690	3.9020 ± 0.1096	3.0290 ± 0.0189
Fe ₂ O ₃	3.163 ± 0.0675	2.6000 ± 0.0236	2.8510 ± 0.0538
Na ₂ O	0.288 ± 0.0055	0.2660 ± 0.0038	0.3620 ± 0.0009
K ₂ O	0.566 ± 0.0001	0.5710 ± 0.0029	0.5280 ± 0.0034
MgO	0.751 ± 0.0001	0.8710 ± 0.0008	0.9860 ± 0.0041
SO ₃	3.443 ± 0.0132	3.4420 ± 0.0167	3.4160 ± 0.0020
Cl ⁻	0.030 ± 0.0010	0.0210 ± 0.0010	0.0370 ± 0.0010

TABLE 2: Results for the Bogue calculation of the test cements.

Brand	Mineral (%)			
	C ₃ S	C ₂ S	C ₃ A	C ₄ AF
A	70.433 ± 0.0220	9.219 ± 0.0018	4.712 ± 0.016	9.626 ± 0.0028
B	66.073 ± 0.0190	9.739 ± 0.0037	3.791 ± 0.029	7.912 ± 0.0021
C	68.092 ± 0.0362	6.207 ± 0.0052	3.204 ± 0.042	8.676 ± 0.0034

role of gypsum is to control the setting time of cement when mixed with water. Slower setting results in greater strength to the set mass.

The alkali and alkaline metal oxides are important because they provide alkalinity in hydrated cement and/or concrete pore systems. The alkalinity protects reinforcing bars against corrosion. A disruption of the pore system would result in corrosion of the rebar. The test cement alkali metal oxides were within the recommended range of 0.100–2.000%, and the alkaline metal oxides were within the stipulated range of 40–67% (KS EAS 18-1 : 2008). The oxides besides providing alkalinity (pH > 10) for the pore water system also provide a medium through which cement phases react [25].

The aluminium oxide and iron oxides of the test cements were within the recommended range of 1.5–8% for OPC [26]. These oxides serve as a flux during clinkerization, thus promoting fusion. This aids in the formation of the calcium silicates at a lower temperature (<2000°C). This makes the process of cement manufacture economical [27]. Given that the cement samples were obtained from the market, the results indicate that the Kenya Standards and East African Standards are observed by the various cement manufacturers in Kenya.

3.2. Compressive Strengths. Compressive strength is a performance measure used by engineers in designing buildings and other structures. The compressive strength results are used in quality control, acceptance of concrete/mortar, and evaluation of adequacy of curing. Compressive strength results for the test cements at various w/c ratios and at 2, 7, 14, and 28 days are represented in Figures 1–4.

From Figures 1–4, it was observed that the compressive strengths increased with curing period at all w/c ratios and for all the test cements. The increase in the compressive strength with curing days was significant. The increase in the compressive strength was significant for all w/c ratios. Hydration

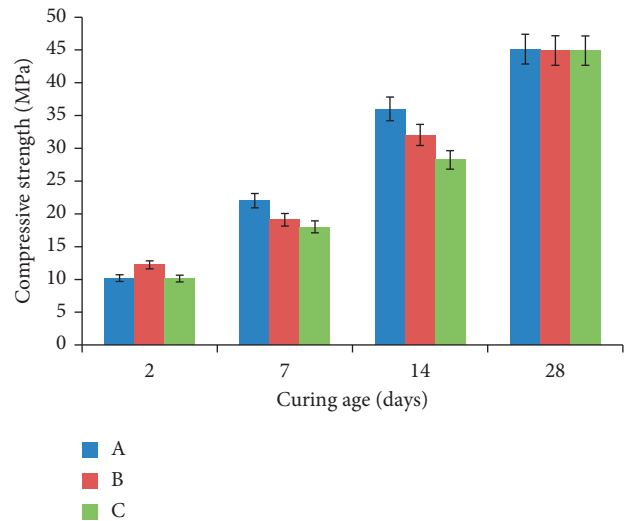
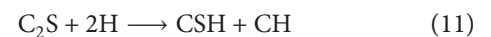
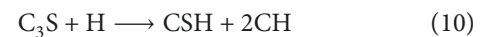


FIGURE 1: Compressive strength at 2, 7, 14, and 28 days for all brands of OPC at w/c 0.5.

is mainly achieved through curing of cement-based materials. The older the concrete/mortar, the greater the hydration that has occurred and the higher the compressive strength [20, 28–31]. Cement gains strength upon hydration. The hydration reactions of C₃S and C₂S are given by



During hydration, CSH is formed which contributes to the strength of the mortars. The Kenya Standard (KEBS KS02-1262, 1993) recommends a minimum strength of 42.5 MPa for OPC at 28 days for w/c = 0.5 and 10 MPa at 2 days. All the test cements met the standard requirement.

There was a decrease in the compressive strength with increase in w/c ratios for all the test cements. This can be

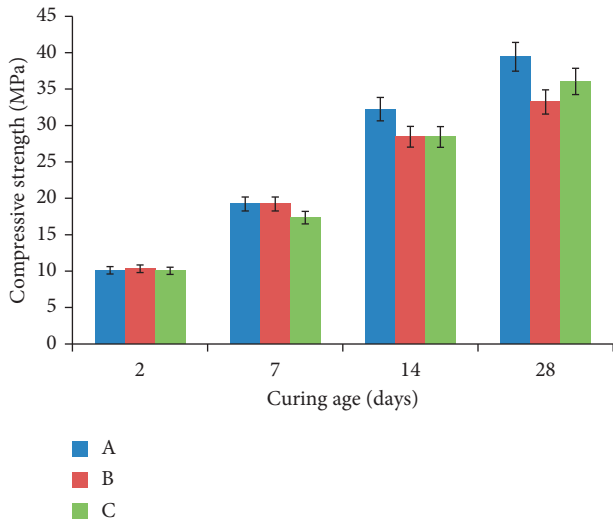


FIGURE 2: Compressive strength at 2, 7, 14, and 28 days for all brands of OPC at w/c 0.6.

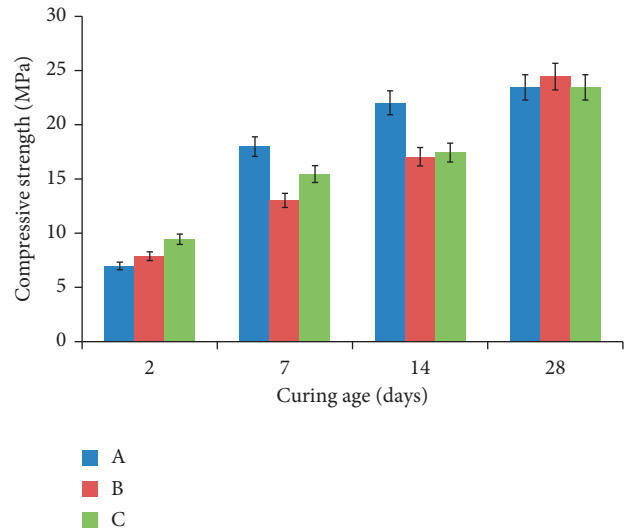


FIGURE 4: Compressive strength of all brands of OPC at w/c 0.7.

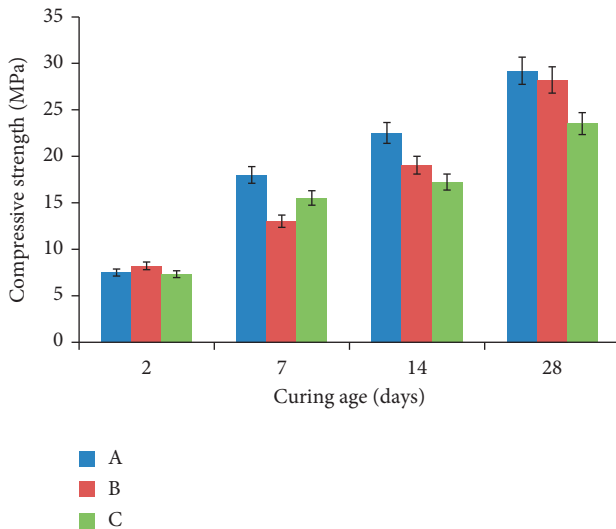


FIGURE 3: Compressive strength at 2, 7, 14, and 28 days for all brands of OPC at w/c 0.65.

attributed to increased porosity at high w/c ratio. The key constituents of all concrete mixes are the binder system and the amount of water present [32, 33]; w/c ratio is considered as the most important factor affecting mortars/concrete strength [33]. This is because it affects the porosity of the hardened paste. The quantity of water used also affects the flow or rheology of the mixture as well as cohesion between paste and aggregate [34]. As a result, it influences the overall strength of the mortar.

It was observed that cement A had generally the highest compressive strength compared to the other test cements. From Bogue’s calculation (Table 2), A, B, and C had 79.652%, 75.812%, and 74.299%, respectively, of combined C₃S and C₂S. These are the two main phases that contribute to the strength development of cements [35]. Hydration of silicates contributes significantly to the strength development of

TABLE 3: Results for analysis of SW and WLI in ppm.

Ion	Concentration in SW (ppm)	WLI
Cl ⁻	18754.67 ± 1.5275	885.00 ± 1.0000
SO ₄ ²⁻	2666.33 ± 1.5275	3300.67 ± 1.1547
Mg ²⁺	1279.33 ± 1.1547	157.00 ± 1.0000
Ca ²⁺	409.00 ± 1.0000	286.67 ± 1.5275
Na ⁺	10750.67 ± 1.1547	1853.33 ± 1.5275

cements. Cement A had the highest amount of C₃S and C₂S (79.652%) and hence the observed compressive strength. Hydration of silicates leads to substantial strength gain.

3.3. *Chemical Analysis of SW and WLI.* Table 3 gives the results for analysis of SW and WLI in ppm.

SW was found to have a higher chloride concentration than WLI. It was therefore expected that mortar prisms subjected to SW would have more gain in compressive strength than the ones subjected to WLI. This was observed in this study. Chlorides are known to be accelerators of compressive strength development in mortars or concrete [1]. On the other hand, WLI was found to have a higher sulphate concentration than SW. Mortar prisms subjected to it were expected to suffer more from sulphate attack [36–38]; this was observed in this study.

3.4. *Compressive Strength Development on Exposure to Aggressive Media and Tap Water.* The change in the compressive strength of the cement mortars subjected to SW, WLI, and TW was compared to their respective strength at 28 days, and their percentage gain/loss was determined. Figures 5–7 show these results after exposure to SW, WLI, and TW, respectively.

There was an observed increase in the strength for all the test cements immersed in SW for all w/c ratios. It was also observed that the strength increased with w/c ratio. Chlorides are known to be accelerators of compressive strength in

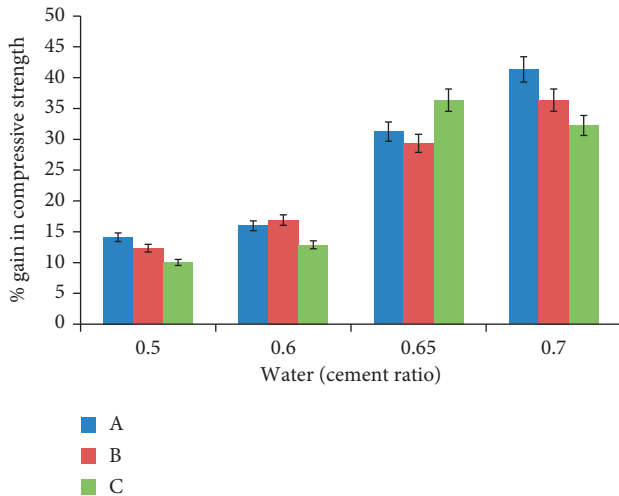


FIGURE 5: Percent gain in compressive strength after exposure to SW.

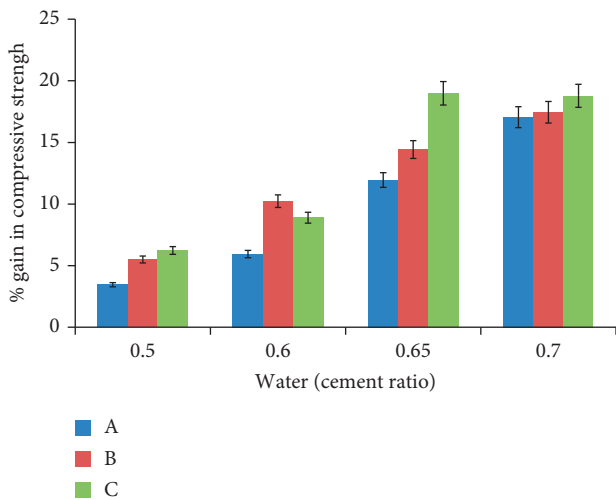


FIGURE 6: Percent loss in compressive strength after exposure of mortars to WLI.

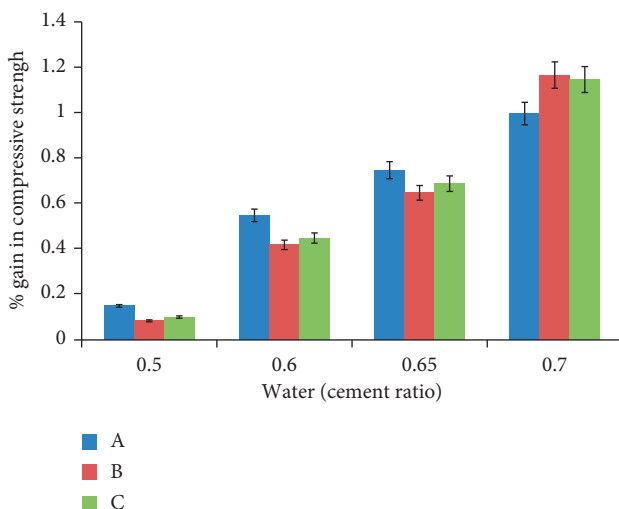


FIGURE 7: Percent gain in compressive strength after exposure of mortars to TW.

mortars/concrete. Seawater contains both chloride and sulphate ions. The presence of chloride ions in the hydrated cement pore water activates residual cement hydration, hence enhancing the strength. Chlorides are more active in enhancing the strength gain than sulphates due to their small charge and ionic sizes. The small size allowed more chlorides into the mortar. This in turn may have allowed more residual hydration products to be formed majorly, Friedel's salt that might have crystallized in the pores. This results in pore refinement and densification of the mortar matrix hence increased compressive strength. Both chlorides and sulphates are known to initiate residual cement hydration [39].

It was also observed that gain in compressive strength increased with increased w/c ratio. High w/c ratio results in increased voids and spaces through which the residue cement hydration reactions occur. Increased voids and spaces due to high w/c ratios give more room for more residual hydration. Generally, cement A had the highest percent gain across all the w/c ratios. This could be attributed to the high content of C_2S and C_3S phase which is observed in Table 2. The phase may have been activated by ingressed Cl^- .

The percent loss in compressive strength after exposure of the mortar to WLI is given in Figure 6 at different w/c ratios.

It was observed that there was a decrease in compressive strength when the mortars were exposed to WLI for all w/c ratios. The loss of the compressive strength may be attributed to the formation of many different compounds such as Na_2SO_4 (thenardite), $Na_2SO_4 \cdot 10H_2O$ (mirabilite), $Na_3H(CO_3)_2 \cdot 2H_2O$ (trona), $Na_2CO_3 \cdot H_2O$ (thermonatrite), and $NaHCO_3$ (nahcolite), and $CaSO_4 \cdot 2H_2O$ (gypsum), $CaSiO_3 \cdot CaCO_3 \cdot CaSO_4 \cdot 15H_2O$ (thaumasite), and $8.5CaSiO_3 \cdot 9.5CaCO_3 \cdot CaSO_4 \cdot 15H_2O$ (birunite). Sodium sulphates can result in damage to the concrete due to cyclic formation of the anhydrous and hydrated forms of these salts [40]. Expansion of concrete may be attributed to the formation of ettringite [31]. Ettringite forms as a result of the chemical reactions between sulphate ions with aluminate phase of cement and $Ca(OH)_2$ [20].

Mortars subjected to a 3.5% sodium chloride and 5% sodium sulphate solution were found to have a percent reduction of about 20.7% and those subjected purely to a 5% sodium sulphate solution 68.3%. This trend elucidated the predominant role of the Cl^- in mitigating sodium sulphate attack. Presence of chloride ions leads to a reduction in the deterioration effects of sulphate ions [41]. The percent expansion of the specimens subjected to combined action of sulphate and chloride ions is less than would be if the specimens were subjected to individual action of sulphate ions. The rate of diffusion of chloride ions is much higher than that of sulphate ions and this allows the chlorides to react with C_3A and C_4AF [42]. The reaction leaves little C_3A available for sulphate ions to react to form ettringite. In this study, cement A had the highest amount of C_3A (4.781%). This may mean that little amount of C_3A was available to react with sulphate ions to form ettringite; hence, cement A experienced least expansion for all w/c ratios. The aggressive media used had both chloride and sulphate ions, and the loss in the compressive strength was significantly different for all w/c ratios. Magnesium attack may also have occurred

resulting in decalcification. In the case of magnesium sulphate attack, brucite, $Mg(OH)_2$, which has low solubility, and its relatively great amount of gypsum released lead to degradation [43]. This is so because magnesium also takes part in the reactions, replacing calcium in the solid phases. The displaced calcium precipitates as gypsum. OPC with low C_3A content is more easily attacked by sulphates [36]. In this study, cement C had the lowest C_3A content and was therefore more attacked. Figure 7 gives the percent gain in compressive strength after exposure of mortars to TW.

It was observed that there was a slight increase in compressive strength subjecting the mortar to TW. TW contains ions such as chlorides which were expected to accelerate compressive strength development. However, the concentration of these ions was too low to cause a substantial increase in strength development. The slight increase in strength was therefore more due to continued hydration process than the presence of the stated ions. Most concrete structures are expected to come into contact with TW as a normal media. From the results, it was observed that WLI is an aggressive media since all the mortars experienced a reduction in compressive strength when compared to those exposed to TW. On the contrary, mortars exposed to SW had gained compressive strength even more than those exposed to TW. This was expected due to the high concentration of chlorides in SW than in TW. TW has a chloride concentration of less than 250 ppm and sulphate concentration of less than 400 ppm (KS 05-459, 1996). However, this did not mean that SW was not an aggressive media. Chlorides, as stated earlier, are used as compressive strength development accelerators in concrete structures [44, 45]. Ingressed chlorides and sulphates cause a gain in compressive strength. Increased strength of the hydrated cement mortars results in a densification of the microstructure of the hydrated cement after exposure to aggressive ions.

3.5. Chloride and Sulphate Profiling

3.5.1. Chloride Profiles. Figures 8–15 show the chloride profiles against the depth of cover of each category of mortar prisms after exposure to SW and WLI, respectively, at various w/c ratios. The profiles involved the determination of the concentration of the chloride ions ($\times 10^{-1}$) at different depths of cement mortar bulk of the test cements.

Figures 12–15 give chloride profiles after exposure to WLI for OPC at different w/c ratios.

From Figures 8–15, it is observed that, as w/c increased, there was an increase in chloride ingress across all the test cements. This can be attributed to continuous and inter-linked voids that provided pathways for ion ingress in hydrated cement mortars at increased w/c ratios. The penetrability of concrete is related to the pore structure of the cement paste matrix. As w/c ratio increases, the porosity of the resultant mortar increases [46]. Increased porosity could have resulted in a higher diffusivity of chlorides and sulphates into the mortar. From the figures again, it was also observed that the ion ingress was highest in the first few millimeters (20 mm) from where their concentration

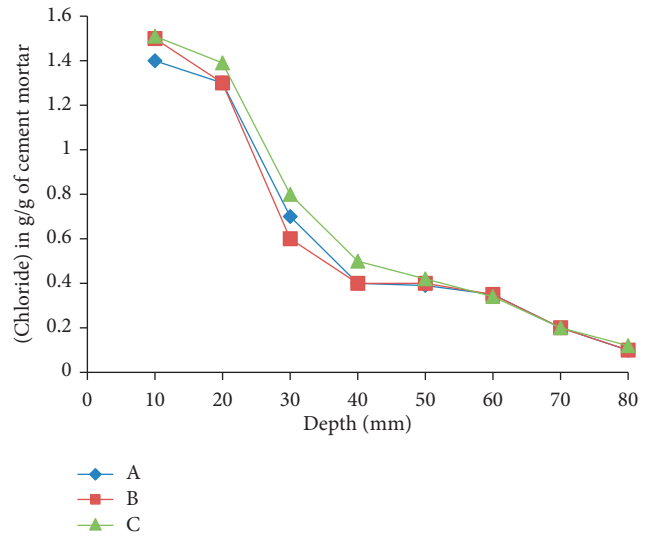


FIGURE 8: Chloride profiles at w/c 0.5.

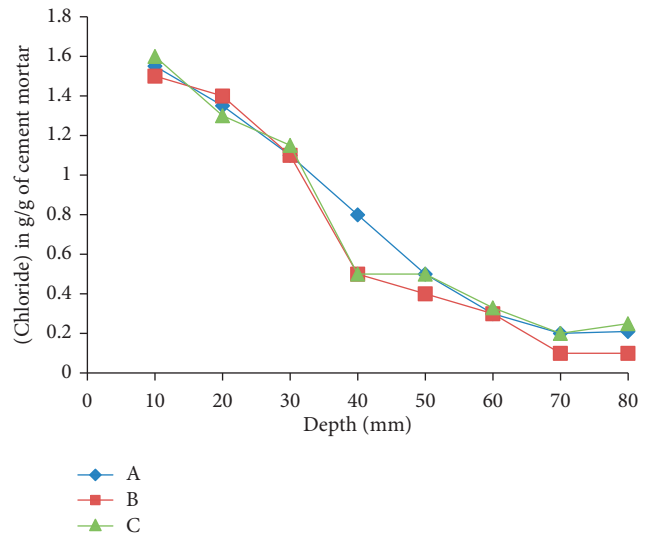


FIGURE 9: Chloride profiles at w/c 0.6.

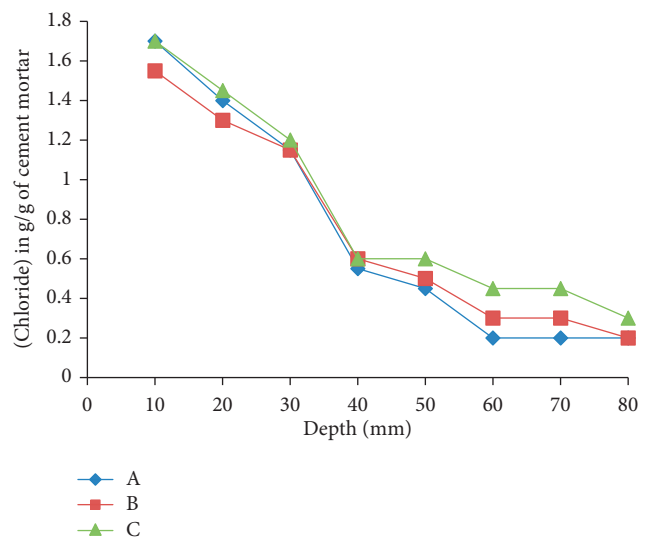


FIGURE 10: Chloride profile at w/c 0.65.

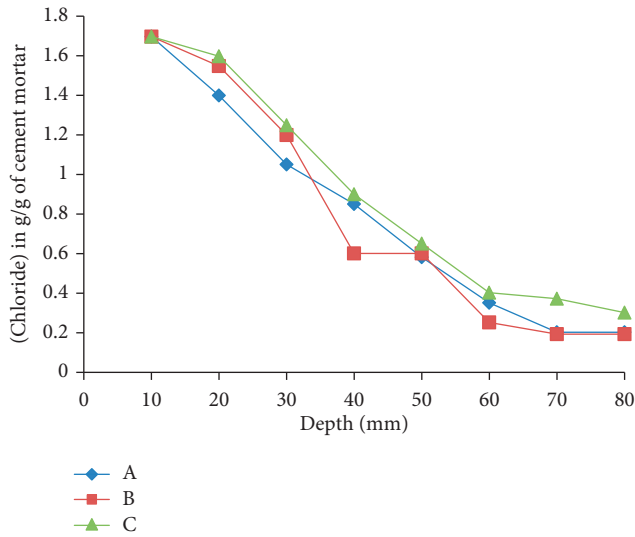


FIGURE 11: Chloride profiles at w/c 0.7.

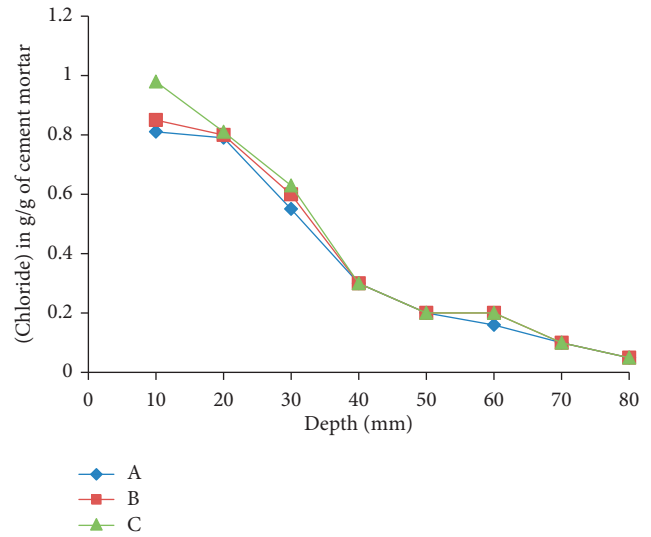


FIGURE 13: Chloride profiles at w/c 0.6.

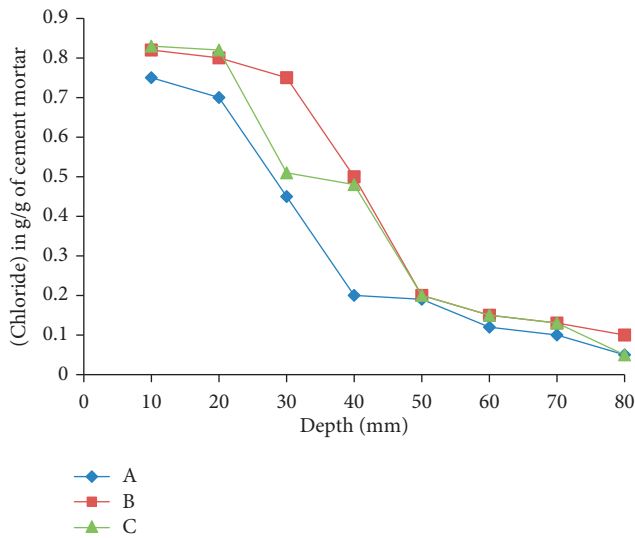


FIGURE 12: Chloride profiles at w/c 0.5.

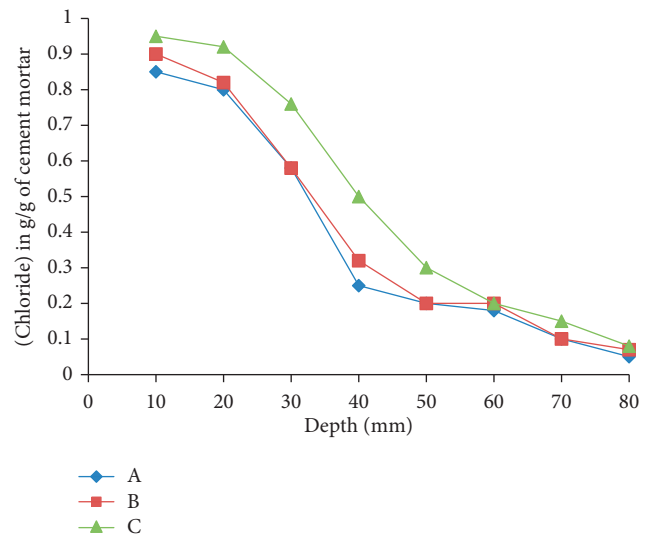


FIGURE 14: Chloride profiles at w/c 0.65.

dropped significantly. This was attributed to the proximity to the exposed surface to the aggressive media. Diffusivity of chloride ions is affected by the amount of C_3A and C_4AF in the cement [47]. A higher amount of C_3A in cement results in a lower diffusivity of chloride ions. C_3A and C_4AF are known to bind chlorides, thus decreasing their ingress. The reaction between C_3A and free chlorides in the hydrated cement results in its reduction from the pore solution. In this study, Figures 14 and 15 show clearly that cement C had a higher total chloride ingress than B and A. The order of the amount of C_3A was $C < B < A$. It can be seen from Table 2 that C had the least amount of C_3A . This showed that it had the lowest proportion of the phase that binds chlorides. C was therefore observed to have the highest chloride diffusivity compared to B and A. This can be attributed to chloride binding capacity of the cement involved. Cements with a high C_3A content are likely to bind chlorides more

than those with low C_3A content [47, 48]. When more chlorides are bound, their diffusivity and thus RC corrosion risk are lowered.

Generally, higher w/c ratios were expected to show increased chloride ingress into the bulk compared lower w/c ratio. This was observed in this study. As the w/c ratio increased, there was a marked rise in the total chloride ingress in all the profile depths of all the test cements. Increase in w/c ratio leads to an increase in porosity. This was dependent upon the depth of penetration which was again dependent upon the brand of OPC.

3.5.2. Sulphate Profiles. Figures 16–23 show sulphate profiles at various w/c ratios after exposure to SW and WLI, respectively.

It was observed that diffusivity of sulphates increased with increase in w/c ratio. This was attributed to porosity and

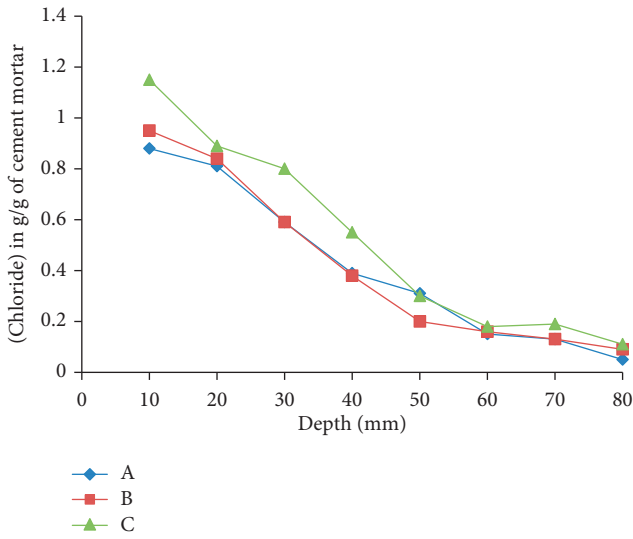


FIGURE 15: Chloride profiles at w/c 0.7.

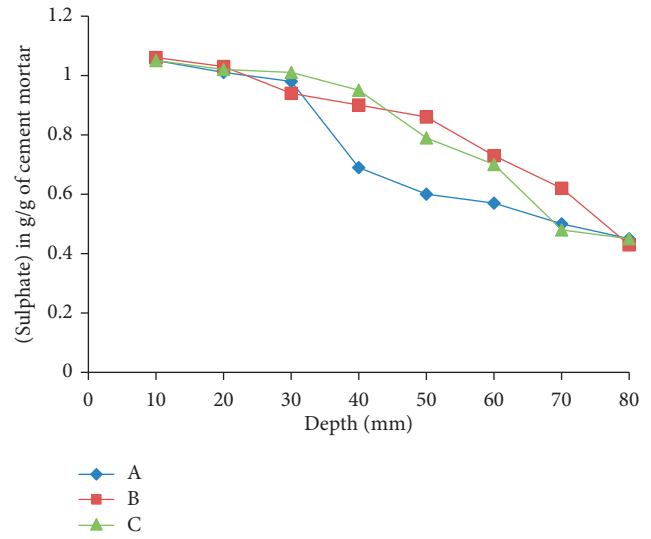


FIGURE 17: Sulphate profiles at w/c 0.6.

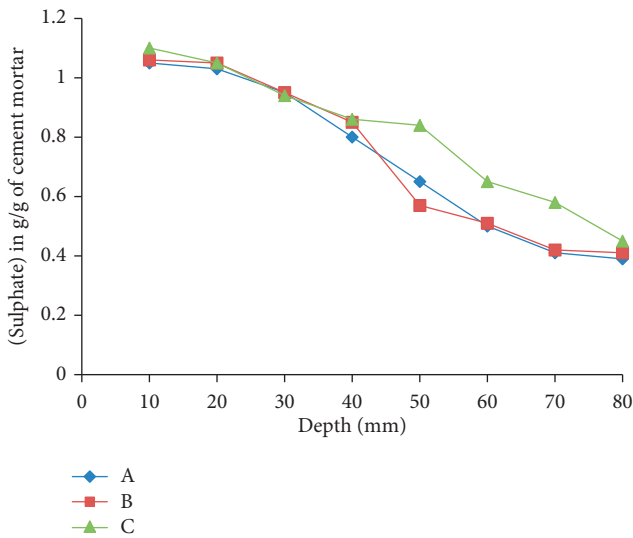


FIGURE 16: Sulphate profiles at w/c 0.5.

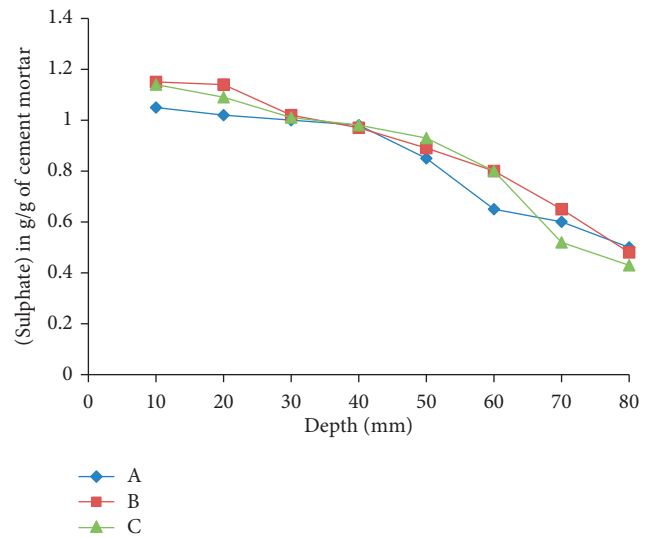


FIGURE 18: Sulphate profiles at w/c 0.65.

permeability of the mortar/concrete [47, 48]. Expansive products are expected to be formed when mortars are subjected to sulphates and fill the voids at high w/c ratio [49]. Possible cracks may have provided a pathway for the ingress of sulphate ions. The mortars may also have suffered sulphate attack which may have resulted in the formation of gypsum, brucite, and ettringite. These products are expansive and thus create voids in the mortar making it more permeable. From the profiles, the concentration was highest in the first 20 mm and then a drop was experienced. This may be attributed to their ionic size. Sulphate ions being bulky ions were not expected to ingress to deep depths. In the presence of chloride ions, sulphate ions are first bound to the hydration products of cements [50]. However, the chloride and sulphate diffusivity can be used as a general quality parameter for evaluation of resistance of concrete against chloride and sulphate intrusion.

3.5.3. *Apparent Diffusion Coefficient.* Figure 24 shows one of the error fitting curves for apparent chloride diffusion coefficient (D_{app}) of cement A mortar. Similar curves were used for the determination of the apparent diffusion coefficients for other test cements. In this study, the equation to solution of Fick's law under non-steady-state conditions for diffusion in a semi-infinite solid was used. Tables 4 and 5 give the D_{app} and r^2 values for different cement mortars and w/c values after exposure to SW and WLI, respectively, for Cl^- , and Tables 6 and 7 give the D_{app} and r^2 values for different cement mortars and w/c values after exposure to SW and WLI, respectively, for SO_4^{2-} .

The D_{app} generally increased with increasing w/c ratio for both chlorides and sulphates. As would have been expected generally, the diffusivity and permeability are higher for the 0.7 w/c systems than 0.5, 0.6, and 0.65. Lowest diffusivities of chloride and sulphate ions for 0.5 w/c were observed for all the test cements. This shows that low

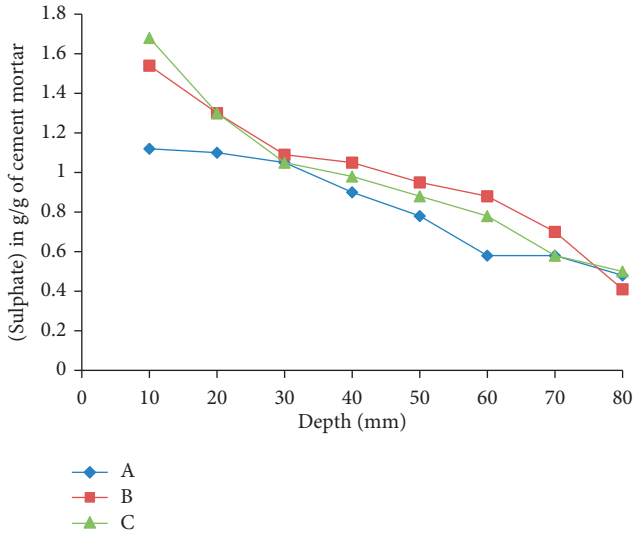


FIGURE 19: Sulphate profiles at w/c 0.7.

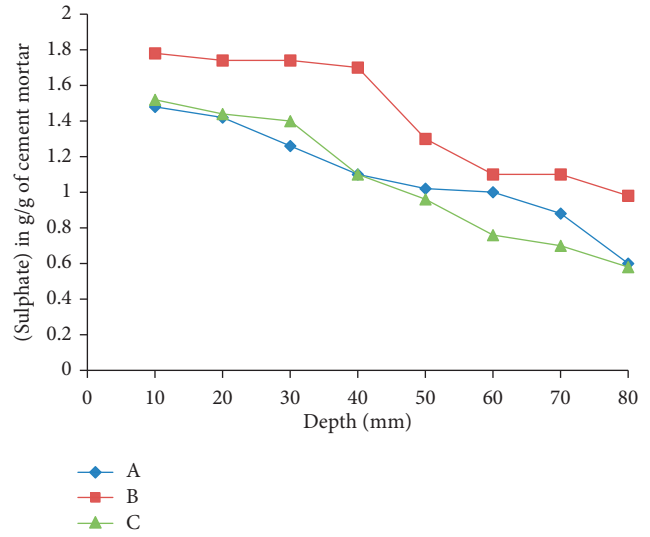


FIGURE 21: Sulphate profiles at w/c 0.6.

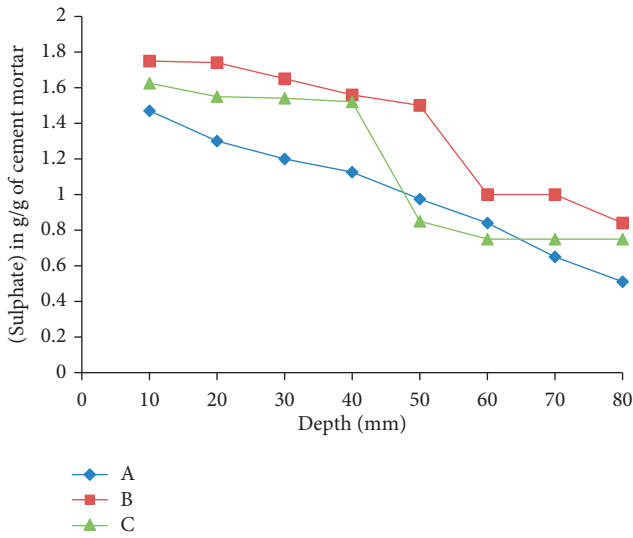


FIGURE 20: Sulphate profiles at w/c 0.5.

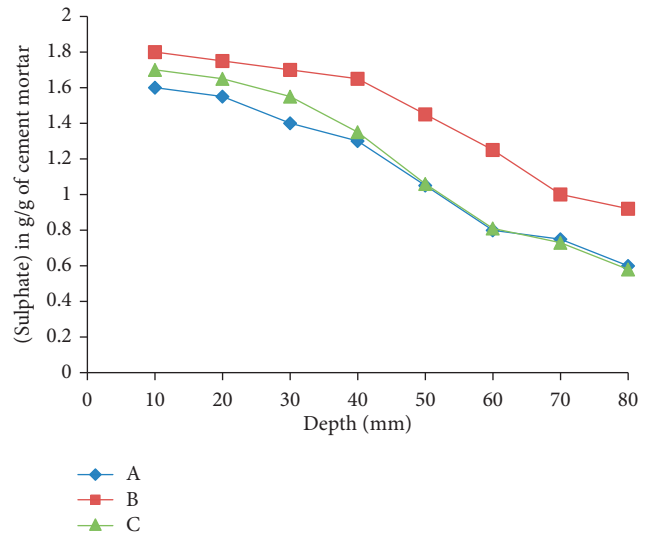


FIGURE 22: Sulphate profiles at w/c 0.65.

w/c ratio gave better resistance to ingress of ions. Increasing w/c ratio increased diffusivity of chlorides and sulphates. High w/c ratio affects porosity. Although increased porosity gives more room for increased cement hydration, extremely high w/c ratios are harmful as the increased porosity acts as pathways for harmful ions and products [51].

It was generally observed that increasing w/c ratio reduced the resistance of the mortars to both Cl^- and SO_4^{2-} diffusion. Diffusivity and permeability of mortars and pastes decrease with increased degree of hydration as a result of curing. Mortars made from cement A were found to have lower Cl^- and SO_4^{2-} diffusivity compared to both B and C for all w/c ratios. This may be due to higher degree of hydration in mortars made from A compared to B and C due to its highest C_3S content which is responsible for the high degree of hydration.

From Table 2, A had the highest C_3A , and this may mean that C_3A may have reacted with chloride ions so that free chloride ions decreased. This then resulted in reduced chloride diffusivity. It was also observed that diffusivity of chlorides in mortars exposed to WLI was slightly higher than those exposed to SW. This was attributed to the higher sulphate ion concentration in WLI compared to SW. From Table 3, it was observed that sulphate concentration was higher in WLI than in SW. The amounts of free chloride ions in the pore water remain high when sulphate ions are added because chloride binding was reduced in the presence of sulphates. This is so because sulphates are bound first occupying sites otherwise available for chlorides [48, 50].

From Tables 4 and 5, D_{app} values for chlorides were found to be in the range of $1.738 \times 10^{-10} m^2/s$ to $4.589 \times 10^{-10} m^2/s$. With low ion ingress, low D_{app} was

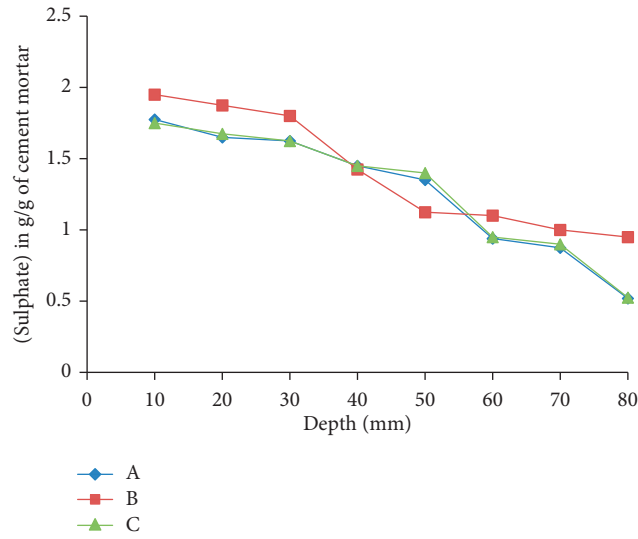


FIGURE 23: Sulphate profiles at w/c 0.7.

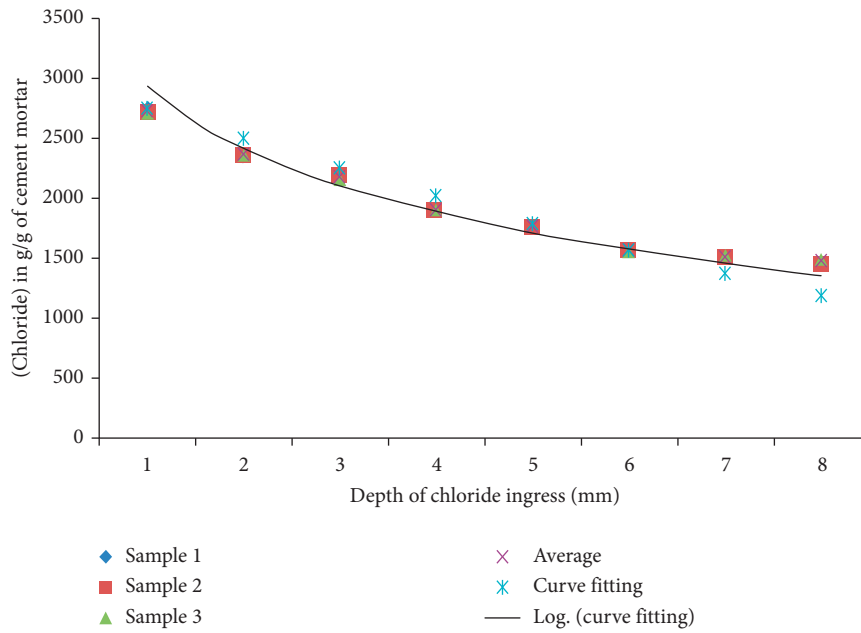


FIGURE 24: Error function fitting for (A) SW (w/c 0.7, Cl⁻), $D_{app} = 3.788 \times 10^{-10} \text{ m}^2/\text{s}$, and $R^2 = 0.9992$.

TABLE 4: D_{app} and r^2 values after exposure to SW for Cl⁻.

Cement type	w/c	D_{app} ($\times 10^{-10} \text{ m}^2/\text{s}$)	r^2	C_s
A	0.5	1.738	0.981	3.00
	0.6	2.716	0.992	1.98
	0.65	3.782	0.988	1.80
	0.7	3.788	0.992	3.00
B	0.5	1.754	0.987	1.70
	0.6	3.912	0.987	1.51
	0.65	3.912	0.981	3.00
	0.7	4.176	0.981	3.50
C	0.5	3.911	0.981	1.67
	0.6	4.176	0.985	1.75
	0.65	4.589	0.983	2.10
	0.7	4.589	0.987	2.50

TABLE 5: D_{app} and r^2 values after exposure to WLI for Cl⁻.

Cement type	w/c	D_{app} ($\times 10^{-10} \text{ m}^2/\text{s}$)	r^2	C_s
A	0.5	2.716	0.987	1.00
	0.6	3.912	0.983	1.10
	0.65	4.016	0.987	0.93
	0.7	4.683	0.987	1.20
B	0.5	2.842	0.987	1.30
	0.6	3.911	0.992	1.28
	0.65	4.268	0.987	1.45
	0.7	4.589	0.983	1.46
C	0.5	3.402	0.987	0.99
	0.6	3.912	0.983	0.99
	0.65	4.226	0.987	1.60
	0.7	4.589	0.987	1.67

TABLE 6: D_{app} and r^2 values after exposure to SW for SO_4^{2-} .

Cement type	w/c	D_{app} ($\times 10^{-11}$ m ² /s)	r^2	C_s
A	0.5	1.065	0.945	1070
	0.6	1.222	0.939	1050
	0.65	7.821	0.936	1070
	0.7	8.148	0.955	1590
B	0.5	1.061	0.955	1200
	0.6	1.569	0.939	1400
	0.65	9.810	0.942	1500
C	0.7	7.821	0.945	1600
	0.5	1.065	0.939	1200
	0.6	1.223	0.936	1300
	0.65	1.569	0.933	1300
	0.7	1.569	0.933	1200

TABLE 7: D_{app} and r^2 Values after exposure to WLI for SO_4^{2-} .

Cement type	w/c	D_{app} ($\times 10^{-11}$ m ² /s)	r^2	C_s
A	0.5	1.0645	0.939	1600
	0.6	1.3906	0.934	1500
	0.65	7.8220	0.945	2100
	0.7	5.4200	0.918	1800
B	0.5	1.0600	0.939	2000
	0.6	1.2200	0.936	2000
	0.65	1.3900	0.934	2100
	0.7	9.1800	0.942	2100
C	0.5	6.5730	0.950	1850
	0.6	10.647	0.939	1600
	0.65	10.647	0.939	1720
	0.7	12.220	0.936	2200

expected. These values were in agreement with D_{app} values for chlorides which have been found to be in the range of 10^{-9} to 10^{-10} m²/s depending on the concrete. In trying to fit the error function in all the test cement mortars, chloride profile results to obtain the D_{app} , it was observed that the fitting was generally good. This was arrived at from the r^2 values that were above 0.98.

From Tables 4 and 5, r^2 values did not show an increase as w/c ratio increased or a decrease as w/c ratio decreased. This could probably show that there were other processes other than pure diffusion involved in the ingress. This change in D_{app} could be attributed to other factors such as sulphate precipitation with the components of the pore solution, adsorption rather than w/c effect only.

In trying to fit the error function in all the test cement mortars, sulphate profile results to obtain the D_{app} , it was observed that the fitting was generally not good. This was arrived at from the r^2 values that were below 0.96. D_{app} values have been reported by many researchers to be in the range of 10^{-10} to 10^{-13} m²/s depending on the concrete [22]. From Tables 6 and 7, r^2 values did not show an increase as w/c ratio increased or a decrease as w/c ratio decreased. This could probably show that there were other processes other than pure diffusion involved in the ingress [48].

Generally as expected, it was observed that the higher the w/c, the higher the D_{app} . From Tables 4–7, there was more ion ingress in the mortars with higher w/c ratio. This in turn resulted in higher D_{app} which can be attributed to increased permeability due to high porosity.

4. Conclusions

Based on the results, analysis, and discussions, the following conclusions were made:

- (i) Diffusivity of both Cl^- and SO_4^{2-} ions increased with w/c ratio for all the test cements
- (ii) Diffusivity of Cl^- ions was higher than that of SO_4^{2-} ions
- (iii) The use of high w/c > 0.5 should be discouraged since it resulted in more ingress of aggressive ions
- (iv) Mortars subjected to SW exhibited a gain in compressive strength as opposed to those subjected to WLI
- (v) All the test cements, A, B, and C, met the stipulated minimum requirements by KS EAS 18-1:2008

Data Availability

The data used in this paper will be provided upon request.

Conflicts of Interest

The authors declare that they have no conflicts of interest.

Acknowledgments

The authors sincerely thank the Department of Materials Testing under the Ministry of Roads in Kenya for providing the laboratory facilities.

References

- [1] J. M. Marangu, J. K. Thiong'o, and J. M. Wachira, "Chloride ingress in chemically activated calcined clay-based cement," *Journal of Chemistry*, vol. 2018, Article ID 1595230, 8 pages, 2018.
- [2] P. Grassl, H. S. Wong, and N. R. Buenfeld, "Influence of aggregate size and volume fraction on shrinkage induced micro-cracking of concrete and mortar," *Cement and Concrete Research*, vol. 40, no. 1, pp. 85–93, 2010.
- [3] C. Alonso, C. Andrade, M. Castellote, and P. Castro, "Chloride threshold values to depassivate reinforcing bars embedded in a standardized OPC mortar," *Cement and Concrete Research*, vol. 30, no. 7, pp. 1047–1055, 2000.
- [4] G. K. Glass and N. R. Buenfeld, "The presentation of the chloride threshold level for corrosion of steel in concrete," *Corrosion Science*, vol. 39, no. 5, pp. 1001–1013, 1997.
- [5] R. R. Hussain and T. Ishida, "Influence of connectivity of concrete pores and associated diffusion of oxygen on corrosion of steel under high humidity," *Construction and Building Materials*, vol. 24, no. 6, pp. 1014–1019, 2010.
- [6] M. Criado, D. M. Bastidas, S. Fajardo, A. Fernández-Jiménez, and J. M. Bastidas, "Corrosion behaviour of a new low-nickel stainless steel embedded in activated fly ash mortars," *Cement and Concrete Composites*, vol. 33, no. 6, pp. 644–652, 2011.
- [7] S. A. Civjan, J. M. LaFave, J. Trybulski, D. Lovett, J. Lima, and D. W. Pfeifer, "Effectiveness of corrosion inhibiting admixture combinations in structural concrete," *Cement and Concrete Composites*, vol. 27, no. 6, pp. 688–703, 2005.
- [8] P. Chindapasirt and S. Rukzon, "Strength, porosity and corrosion resistance of ternary blend Portland cement, rice

- husk ash and fly ash mortar,” *Construction and Building Materials*, vol. 22, no. 8, pp. 1601–1606, 2008.
- [9] M. N. Haque and O. A. Kayyali, “Free and water soluble chloride in concrete,” *Cement and Concrete Research*, vol. 25, no. 3, pp. 531–542, 1995.
- [10] A. A. Sagüés, “Chapter 3—corrosion of metals in concrete,” in *Galvanized Steel Reinforcement in Concrete*, S. R. Yeomans, Ed., pp. 71–86, Elsevier Science, Amsterdam, Netherlands, 2004.
- [11] S. Mundra, M. Criado, S. A. Bernal, and J. L. Provis, “Chloride-induced corrosion of steel rebars in simulated pore solutions of alkali-activated concretes,” *Cement and Concrete Research*, vol. 100, pp. 385–397, 2017.
- [12] K. K. Aligizaki, “Mechanisms of ion transport in cement-based materials during the application of corrosion mitigating electrical techniques,” in *Proceedings of the NACE-2012-1542*, pp. 1–15, NACE International, Salt Lake City, UT, USA, March 2012.
- [13] R. R. Hussain and T. Ishida, “Enhanced electro-chemical corrosion model for reinforced concrete under severe coupled action of chloride and temperature,” *Construction and Building Materials*, vol. 25, no. 3, pp. 1305–1315, 2011.
- [14] M. Maes, K. Van Tittelboom, and N. De Belie, “The efficiency of self-healing cementitious materials by means of encapsulated polyurethane in chloride containing environments,” *Construction and Building Materials*, vol. 71, pp. 528–537, 2014.
- [15] A. M. D. Oliveira and O. Cascudo, “Effect of mineral additions incorporated in concrete on thermodynamic and kinetic parameters of chloride-induced reinforcement corrosion,” *Construction and Building Materials*, vol. 192, pp. 467–477, 2018.
- [16] K. O. Ampadu and K. Torii, “Chloride ingress and steel corrosion in cement mortars incorporating low-quality fly ashes,” *Cement and Concrete Research*, vol. 32, no. 6, pp. 893–901, 2002.
- [17] M. Mwinyihija, “Pollution control and remediation of the tanning effluent,” *The Open Environmental Pollution & Toxicology Journal*, vol. 3, no. 1, pp. 55–64, 2012.
- [18] G. Boshoff, J. Duncan, and P. D. Rose, “Tannery effluent as a carbon source for biological sulphate reduction,” *Water Research*, vol. 38, no. 11, pp. 2651–2658, 2004.
- [19] H.-W. Song, C.-H. Lee, and K. Y. Ann, “Factors influencing chloride transport in concrete structures exposed to marine environments,” *Cement and Concrete Composites*, vol. 30, no. 2, pp. 113–121, 2008.
- [20] M. J. Mwititi, T. J. Karanja, and W. J. Muthengia, “Properties of activated blended cement containing high content of calcined clay,” *Heliyon*, vol. 4, no. 8, article e00742, 2018.
- [21] P. Stutzman, A. Heckert, A. Tebbe, and S. Leigh, “Uncertainty in Bogue-calculated phase composition of hydraulic cements,” *Cement and Concrete Research*, vol. 61–62, pp. 40–48, 2014.
- [22] C. Andrade, “Calculation of chloride diffusion coefficients in concrete from ionic migration measurements,” *Cement and Concrete Research*, vol. 23, no. 3, pp. 724–742, 1993.
- [23] J. Crank, *The Mathematics of Diffusion*, Clarendon Press, Oxford, UK, 2nd edition, 1975.
- [24] T. Luping and J. Gulikers, “On the mathematics of time-dependent apparent chloride diffusion coefficient in concrete,” *Cement and Concrete Research*, vol. 37, no. 4, pp. 589–595, 2007.
- [25] T. Chappex and K. Scrivener, “Alkali fixation of C-S-H in blended cement pastes and its relation to alkali silica reaction,” *Cement and Concrete Research*, vol. 42, no. 8, pp. 1049–1054, 2012.
- [26] P. Juilland, A. Kumar, E. Gallucci, R. J. Flatt, and K. L. Scrivener, “Effect of mixing on the early hydration of alite and OPC systems,” *Cement and Concrete Research*, vol. 42, no. 9, pp. 1175–1188, 2012.
- [27] U. T. Bezerra, A. E. Martinelli, D. M. A. Melo, M. A. F. Melo, and F. M. Lima, “A correlation between Bogue’s equations and Taylor’s procedure for the evaluation of crystalline phases in special class Portland oilwell cement clinker,” *Cerâmica*, vol. 57, no. 341, pp. 122–128, 2011.
- [28] M. J. Mwititi, T. J. Karanja, and W. J. Muthengia, “Thermal resistivity of chemically activated calcined clays-based cements,” in *Calcined Clays for Sustainable Concrete*, F. Martirena, A. Favier, and K. Scrivener, Eds., pp. 327–333, Springer, Dordrecht, Netherlands, 2018.
- [29] M. H. Almabrok, R. G. McLaughlan, and K. Vessalas, “Effect of curing and mixing methods on the compressive strength of mortar containing oil,” *Journal of Civil Engineering, Science and Technology*, vol. 6, no. 1, pp. 6–11, 2015.
- [30] A. A. Amadi and A. S. Osu, “Effect of curing time on strength development in black cotton soil—quarry fines composite stabilized with cement kiln dust (CKD),” *Journal of King Saud University—Engineering Sciences*, vol. 30, no. 4, pp. 305–312, 2016.
- [31] C. Angulski da Luz and R. D. Hooton, “Influence of curing temperature on the process of hydration of supersulfated cements at early age,” *Cement and Concrete Research*, vol. 77, pp. 69–75, 2015.
- [32] Y.-Y. Kim, K.-M. Lee, J.-W. Bang, and S.-J. Kwon, “Effect of W/C ratio on durability and porosity in cement mortar with constant cement amount,” *Advances in Materials Science and Engineering*, vol. 2014, Article ID 273460, 11 pages, 2014.
- [33] S. B. Singh, P. Munjal, and N. Thammishetti, “Role of water/cement ratio on strength development of cement mortar,” *Journal of Building Engineering*, vol. 4, pp. 94–100, 2015.
- [34] R. Radhakrishna and K. Praveen Kumar, “Characteristics of cement mortar with M-sand as replacement of fine aggregates,” *Materials Today: Proceedings*, vol. 5, no. 11, pp. 25412–25419, 2018.
- [35] A. M. Neville, *Properties of Concrete*, Longman, London, UK, 4th edition, 1997.
- [36] M. M. Amin, S. B. Jamaludin, F. C. Pa, and K. K. Chuen, “Effects of magnesium sulfate attack on ordinary Portland cement (OPC) mortars,” *Portugaliae Electrochimica Acta*, vol. 26, no. 2, pp. 235–242, 2007.
- [37] M. N. Aziez and A. Bezzar, “Magnesium sulphate attacks on mortars-influence of temperature, type of sand and type of cement,” *Journal of Engineering Science & Technology Review*, vol. 10, no. 1, pp. 41–50, 2017.
- [38] E. Dan and I. Janotka, “Chemical resistance of Portland cement, blast-furnace slag Portland cement and sulphoaluminate-belite cement in acid, chloride and sulphate solution: some preliminary results,” *Ceramics-Silikaty*, vol. 47, pp. 141–148, 2003.
- [39] S. Zofia and Z. Adam, “Theoretical model and experimental tests on chloride diffusion and migration processes in concrete,” *Procedia Engineering*, vol. 57, pp. 1121–1130, 2013.
- [40] Z. Liu, F. Zhang, D. Deng, Y. Xie, G. Long, and X. Tang, “Physical sulfate attack on concrete lining—a field case analysis,” *Case Studies in Construction Materials*, vol. 6, pp. 206–212, 2017.

- [41] P. W. Brown and A. Doerr, "Chemical changes in concrete due to the ingress of aggressive species," *Cement and Concrete Research*, vol. 30, no. 3, pp. 411–418, 2000.
- [42] A. Delagrave, J. Marchand, J.-P. Ollivier, S. Julien, and K. Hazrati, "Chloride binding capacity of various hydrated cement paste systems," *Advanced Cement Based Materials*, vol. 6, no. 1, pp. 28–35, 1997.
- [43] O. Hodhod and G. A. Salama, "Analysis of sulfate resistance in concrete based on artificial neural networks and USBR4908-modeling," *Ain Shams Engineering Journal*, vol. 4, no. 4, pp. 651–660, 2013.
- [44] A. E. Abalaka and A. D. Babalaga, "Effects of sodium chloride solutions on compressive strength development of concrete containing rice husk ash," *ATBU Journal of Environmental Technology*, vol. 4, no. 1, pp. 33–40, 2011.
- [45] E. A. Kishar, D. A. Ahmed, M. R. Mohammed, and R. Noury, "Effect of calcium chloride on the hydration characteristics of ground clay bricks cement pastes," *Beni-Suef University Journal of Basic and Applied Sciences*, vol. 2, no. 1, pp. 20–30, 2013.
- [46] M. Erniati, M. W. Tjaronge, U. Zulharnah, and U. R. Irfan, "Porosity, pore size and compressive strength of self compacting concrete using sea water," *Procedia Engineering*, vol. 125, pp. 832–837, 2015.
- [47] M. J. Kim, K. B. Kim, and K. Y. Ann, "The influence of C3A content in cement on the chloride transport," *Advances in Materials Science and Engineering*, vol. 2016, Article ID 5962821, 8 pages, 2016.
- [48] N. R. Wangui, "Sulphate and chloride ingress and the effect in selected cements mortar prisms immersed in sea water and leather industry effluent," MSc thesis, Kenyatta University, Nairobi, Kenya, 2014.
- [49] J. W. Bullard, H. M. Jennings, R. A. Livingston et al., "Mechanisms of cement hydration," *Cement and Concrete Research*, vol. 41, no. 12, pp. 1208–1223, 2011.
- [50] H. Y. Ghorab, E. A. Kishar, and S. H. Abou Elfetouh, "Studies on the stability of the calcium sulfoaluminate hydrates. Part II: effect of alite, lime, and monocarboaluminate hydrate," *Cement and Concrete Research*, vol. 28, no. 1, pp. 53–61, 1998.
- [51] L. Bágel and V. Živica, "Relationship between pore structure and permeability of hardened cement mortars: on the choice of effective pore structure parameter," *Cement and Concrete Research*, vol. 27, no. 8, pp. 1225–1235, 1997.